A NEW APPROACH FOR TRANSITION METAL FREE MAGNETIC SiC: DEFECT INDUCED MAGNETISM AFTER SELF-ION IMPLANTATION

Venkata Chandra Sekhar Kummari, M.Sc.

Dissertation Prepared for the Degree of

DOCTOR OF PHILOSOPHY

UNIVERSITY OF NORTH TEXAS

May 2013

APPROVED:

Bibhudutta Rout, Major Professor
Tilo Reinert, Minor Professor
Jerome L. Duggan, Committee Member
Floyd D. McDaniel, Committee Member
Duncan L. Weathers, Committee Member
Srinivasan G. Srivilliputhur, Committee Member
David R. Schultz, Chair of the Department of Physics
Mark Wardell, Dean of the Toulouse Graduate School

Kummari, Venkata Chandra Sekhar, A new approach for transition metal free magnetic SiC: Defect induced magnetism after self-ion implantation. Doctor of Philosophy (Physics), May 2013, 137 pp., 11 tables, 56 illustrations, chapter references.

SiC has become an attractive wide bandgap semiconductor due to its unique physical and electronic properties and is widely used in high temperature, high frequency, high power and radiation resistant applications. SiC has been used as an alternative to Si in harsh environments such as in the oil industry, nuclear power systems, aeronautical, and space applications.

SiC is also known for its polytypism and among them 3*C*-SiC, 4*H*-SiC and 6*H*-SiC are the most common polytypes used for research purposes. Among these polytypes 4*H*-SiC is gaining importance due to its easy commercial availability with a large bandgap of 3.26 eV at room temperature.

Controlled creation of defects in materials is an approach to modify the electronic properties in a way that new functionality may result. SiC is a promising candidate for defect-induced magnetism on which spintronic devices could be developed. The defects considered are of room temperature stable vacancy types, eliminating the need for magnetic impurities, which easily diffuse at room temperature. Impurity free vacancy type defects can be created by implanting the host atoms of silicon or carbon. The implantation fluence determines the defect density, which is a critical parameter for defect induced magnetism. Therefore, we have studied the influence of low fluence low energy silicon and carbon implantation on the creation of defects in n-type 4*H*-SiC. The characterization of the defects in these implanted samples was performed using the techniques, RBS-channeling and Raman spectroscopy. We have also utilized these characterization techniques to analyze defects created in much deeper layers of the SiC due to implantation of high energy nitrogen ions.

The experimentally determined depths of the Si damage peaks due to low energy (60 keV) Si and C ions with low fluences (< 10^{15} cm^{-2}) are consistent with the SRIM-2011 simulations. From RBS-C Si sub-lattice measurements for different fluences (1.1×10^{14} cm^{-2} to 3.2×10^{14} cm^{-2}) of Si implantation in 4*H*-SiC, the Si vacancy density is estimated to range from 1.29×10^{22} cm^{-3} to 4.57×10^{22} cm^{-2}, corresponding to average vacancy distances of 4.26 Å to 2.79 Å at the damage peak (50±5 nm). Similarly, for C implanted fluences (1.85×10^{14} cm^{-2} to 1×10^{15} cm^{-2}), the Si vacancy density varies from 1.37×10^{22} cm^{-3} to 4.22×10^{22} cm^{-3} with the average vacancy distances from 4.17 Å to 2.87 Å at the damage peak (110±10 nm). From the Raman spectroscopy, the implantation-induced lattice disorders calculated along the c-axis (LO mode) and perpendicular to c-axis (TO mode) in 4*H*-SiC are found to be similar.

Furthermore, the results obtained from SQUID measurements in C implanted n-type 4*H*-SiC sample with fluences ranging from 1×10^{12} to 1.7×10^{16} ions/cm^2 have been discussed. The implanted samples showed diamagnetism similar to the unimplanted sample. To date, to our best of knowledge, no experimental work has been reported on investigating defect induced magnetism for self-ion implantation in n-type 4*H*-SiC. These first reports of experimental results can provide useful information in future studies for a better understanding of self-ion implantation in SiC-based DMS.

Copyright 2013

by

Venkata Chandra Sekhar Kummari

ACKNOWLEDGEMENTS

First I would like to thank Dr. Bibhudutta Rout for being my Ph.D. major advisor and for encouragements, providing me moral support, research assistantship and guidance during my Ph.D. program at UNT. I also want to express my sincere gratitude to my minor advisor Dr. Tilo Reinert for his guidance, encouragements and ideas during the research work.

Special thanks to Dr. Floyd Del McDaniel for his guidance and support throughout the dissertation research. Many thanks to Dr. Jerome L. Duggan who's helping, encouragement and personal training and guidance on handling of accelerators have provided an excellent basis for my Ph.D. research. I wish to express my best gratitude to Dr. Duncan L. Weathers for having the privilege to work and learn from his expertise. I would like to thank Dr. Gary A. Glass and Dr. Srinivasan G. Srivilliputhur for being my dissertation committee members and providing me their valuable advice.

I also want to thank Dr. Weilin Jiang for his great help with RBS-channeling measurements at Pacific Northwest National Laboratory, Richland, Washington. My thanks are also due to Dr. John V. Kennedy and Dr. Peter P. Murmu from GNS Science, Lower Hutt, New Zealand and Dr. Pablo Esquinazi and Ms. Annette Setzer from the University of Leipzig, Germany for SQUID measurements. Thanks also go to the Center for Advanced and Research Technology (CART) at UNT for Raman measurements.

I also want to acknowledge my present colleagues at the Ion Beam Modification and Analysis (IBMAL) laboratory: Mangal S. Dhoubhadel, Naresh T. Deoli, Wickramaarachchi J. Lakshantha, Stephen J. Mulware, Jack E. Manuel, Jose L. Pacheco and Bimal Pandey. Thanks also go to the past laboratory personnel past: Eric Smith, Dr. Khalid Hossain, Dr. Prakash P. Poudel and Dr. Lucas C. Phinney, I have been very fortunate to have such great colleagues. I

would also like to thank Dr. David R. Schultz, the Department Chair and other faculty members, staff and all my other friends in the Physics Department.

My sincere thanks are due to my parents and my sister for their constant support, vision and inspiration in my life. I would like to dedicate this thesis to my parents and my sister. Without them I would not have been in this position. I also need to thank my wonderful in-laws for their trust in me. Finally I want to express my heartfelt thanks for my beautiful wife, Mrs. Shannon Kummari for her patience throughout my Ph.D. career. Her love and understanding played a catalytic role in my accomplishments during the Ph.D. career.

TABLE OF CONTENTS

Page

ACKNOWLEDGEMENT ... iii

TABLES ... ix

FIGURES ... xi

1 INTRODUCTION ... 1

1.1 Motivation ... 1

1.2 Magnetism in Materials ... 2

1.2.1 Diamagnetism ... 3

1.2.2 Paramagnetism ... 3

1.2.3 Ferromagnetism ... 4

1.3 Literature Review on Ferromagnetism Behavior of SiC ... 6

1.4 Summary of Chapters in this Thesis Work ... 10

1.5 References ... 11

2 OVERVIEW OF SILICON CARBIDE ... 17

2.1 Crystal Structure and Structural Properties ... 17

2.1.1 Mechanical and Thermal Properties ... 21

2.1.2 Optical and Electronic Properties ... 22

2.2 Defects in SiC ... 23

2.3 Ion Implantation Induced Defect Engineering in SiC ... 25

2.4 Potential Applications ... 26

2.5 References ... 28

3 THEORETICAL SIMULATIONS OF INTERACTION OF IONS IN MATERIALS AND EXPERIMENTAL CHARACTERIZATION TECHNIQUES ... 32
3.1 Introduction ... 32
3.2 Ion Beam Facility at IBMAL ... 32
3.3 Ion Implantation ... 37
3.4 Simulation of Ion Irradiation Parameters using SRIM/TRIM-2011 ... 39
3.4.1 Introduction ... 39
3.4.2 Theoretical Calculations of Irradiation Parameters of C Implanted in 4*H*-SiC using SRIM/TRIM-2011 ... 39
3.4.3.. Theoretical Calculations of Irradiation Parameters of Si Implanted in 4*H*-SiC using SRIM/TRIM-2011 ... 44
3.5 Characterization Techniques ... 47
3.5.1 Rutherford Backscattering Spectroscopy ... 47
3.5.1.1 Kinematic Factor K and Scattering Cross section σ ... 47
3.5.1.2 Stopping Power and Energy Loss ... 49
3.5.1.3 RBS-C ... 50
3.5.2 Raman Spectroscopy ... 52
3.5.2.1 Classical Theory ... 55
3.5.2.2 Quantum Theory ... 56
3.5.2.3 Experimental Set Up ... 57
3.5.3 Superconducting QUantum Interference Device ... 59
3.6 References ... 62

4 CHARACTERIZATION OF DEFECTS IN LOW ENERGY (C, SI) ION IMPLANTED 4*H*-SIC 64
4.1 Introduction 64
4.2 Ion Implantation and RBS-C Experimental Procedure 66
4.2.1 Experimental Set Up for RBS-C Analysis 68
4.2.2 Minimum Yield and Angular Scan 68
4.2.3 Kinematic Factor and Differential Cross-Section 70
4.2.4 Channel Number to Energy Conversion 71
4.2.5 Energy Loss and Depth Analysis 73
4.2.5.1 Surface Approximation 75
4.2.5.2 Mean Energy Approximation 75
4.2.6 Analysis of Defect Concentration 76
4.2.7 RBS-C Analysis for C Implanted 4*H*-SiC 77
4.2.8 RBS-C Analysis for Si Implanted 4*H*-SiC 83
4.3 Raman Analysis of Ion Implantation in 4*H*-SiC 87
4.3.1 Raman Results for C Implanted 4*H*-SiC at the Energy of 60 keV 87
4.3.2 Raman Results for Si Implanted 4*H*-SiC at Low Energy 60 keV 90
4.4 Disorder Evaluation for C and Si Implanted 4*H*-SiC Samples 91
4.5 Investigation of Magnetic Properties using SQUID for C Implanted n-type 4*H*-SiC 98
4.5.1 Introduction 98
4.5.2 Experimental Results 98
4.6 References 110

5 DEFECT CHARACTERIZATION OF HIGH ENERGY IMPLANTATION OF N IN 4*H*-SIC 115

5.1 Introduction 115

5.2 Theoretical Simulations and N Ion Implantation in 4*H*-SiC 116

5.2.1 SRIM/TRIM-2011 Simulations 116

5.2.2 High Energy Nitrogen Ion Implantation in 4*H*-SiC 117

5.3 Experimental Analysis of N Implanted 4*H*-SiC Samples 117

5.3.1 RBS-C Analysis 117

5.3.2 Raman Analysis of Nitrogen Implanted 4*H*-SiC 122

5.4 References 125

6 SUMMARY OF THE DISSERTATION 127

6.1 RBS-C and Raman Measurements 128

6.1.1 C Implantation in 4*H*-SiC 128

6.1.2 Si Implantation in 4*H*-SiC 128

6.1.3 N Implantation in 4*H*-SiC 129

6.2 SQUID Measurements for C Implanted n-type 4*H*-SiC 129

6.3 Significance of my Research Work 130

APPENDIX: STOPPING AND RANGE OF IONS IN MATTER/TRANSPORT OF IONS IN MATTER (SRIM/TRIM - 2011) 133

A.1 References 137

LIST OF TABLES

Page

Table 2.1: Notations of four common SiC polytypes and corresponding inequivalent lattice sites. 18

Table 2.2: Properties of three commonly used polytypes of SiC along with most used semiconductor Si at 300 K for comparison [9, 10]. 22

Table 3.1: Calculated values for different parameters using SRIM/TRIM simulations for C ion implantation in 4*H*-SiC at low energy 60 keV....44

Table 3.2: Calculated values for different parameters using SRIM/TRIM simulations for Si ion implantation in 4*H*-SiC at low energy 60 keV....46

Table 4.1: Relative damage on Si sub-lattice extracted from RBS-C data for different fluences of 60 keV Si and C implanted in 4*H*-SiC....86

Table 4.2: dpa and average distance of vacancies at the damage peak position (50±5 nm) calculated as a function of 60 keV Si implantation fluences in 4*H*-SiC. The estimation of the error in the average distance of vacancies stems from the statistical error found in the relative disorder ratio. 96

Table 4.3: dpa and average distance of vacancies at the damage peak position (110±10 nm) calculated as a function of 60 keV C implantation fluences in 4*H*-SiC. The estimation of the error in the average distance of vacancies stems from the statistical error found in the relative disorder ratio. 96

Table 4.4: Relative damage on Si sub-lattice from RBS-C data and relative disorder from Raman measurements for implanted C fluences in n-type 4*H*-SiC at low energy 60 keV. 97

Table 4.5: Relative damage on Si sub-lattice from RBS-C data and relative disorder from Raman measurements for implanted Si fluences in n-type 4*H*-SiC at low energy 60 keV. 97

Table 4.6: Different parameters calculated for C implantation in n-type 4*H*-SiC at low energy 60 keV for SQUID measurements. 99

Table 5.1: Relative damage on Si sub-lattice from RBS-C data and relative disorder from Raman measurements for implanted N fluences in n-type 4*H*-SiC at high energy 1 MeV. 125

LIST OF FIGURES

Page

Figure 1.1: Ordering of (a) paramagnetism (b) ferromagnetism and (c) anti-ferromagnetism. 3

Figure 1.2: Hysteresis loop showing the relationship between magnetization, M and the applied magnetic field, H. 5

Figure 2.1: Tetrahedron building block of SiC crystal. (a) Four carbon atoms bonded to one silicon atom (b) Four silicon atoms bonded to one carbon atom. 17

Figure 2.2: Stacking sequence of double layers of 2*H*- SiC polytype obtained from the database of Materials Design Software, MedeA. 19

Figure 2.3: Stacking sequence of double layers of 4*H*- SiC polytype obtained from the database of Materials Design Software, MedeA. 19

Figure 2.4: Stacking sequence of double layers of 6*H*- SiC polytype obtained from the database of Materials Design Software, MedeA. 20

Figure 2.5: Stacking sequence of most common polytypes of SiC. The cubic and hexagonal crystal symmetry points are represented by h and k respectively. 21

Figure 3.1: Schematics of the main laboratory at IBMAL, showing the 3 MV tandem (9SDH-2) and the 3 MV single ended (9SH) NEC Pelletron® accelerators and associated beam lines and experimental end stations. 33

Figure 3.2: Schematics of (a) Pelletron® charging system. (b) The Pelletron® chain which consists of alternating insulating and conducting components. Adopted with permission from Dr. Greg Norton, National Electrostatics Corporation. 34

Figure 3.3: Schematics of the low energy ion implantation facility associated with the 9SDH-2 tandem accelerator. 35

Figure 3.4: Schematics of the source of negative ions by cesium sputtering (SNICS-II) associated with the 9SDH-2 tandem accelerator. Adopted with permission from Dr. Greg Norton, National Electrostatics Corporation. 36

Figure 3.5: SRIM/TRIM simulation of 60 keV carbon ions in 4*H*-SiC showing the collision cascade within the target. 40

Figure 3.6: TRIM simulation of C ion implantation in 4*H*-SiC at the energy of 60 keV. 41

Figure 3.7: TRIM plot of collision events which includes target displacements, vacancies and replacement collisions. 42

Figure 3.8: TRIM plot of energy to recoil atoms. 43

Figure 3.9 : TRIM plots for 60 keV Si implantation in 4*H*-SiC. (a) Monte-Carlo simulation of 60 keV silicon ions in 4H-SiC showing the collision cascade within the target. (b) Plot of the Si ion-distribution, (c) Collision plot which includes target displacements, vacancies and replacement collisions. (d) TRIM plot of energy to recoil atoms. 45

Figure 3.10: Scattering representation of an elastic collision between a projectile of mass M1, velocity v, and energy E_0 and a target mass M_2 which is initially at rest. After the collision, the projectile and the target mass have velocities and energies v_1, E_1 and v_2, E_2 respectively. The angles θ and Φ are positive as shown. All quantities refer to a laboratory frame of reference. 48

Figure 3.11: (a) Lattice atoms viewed along the axial direction (b) Equipotential surfaces. 50

Figure 3.12: Schematically representation of (a) Rayleigh scattering (b) Stokes scattering and (c) anti-Stokes scattering. 53

Figure 3.13: Thermo Electron Almega XR Raman Spectrometer at CART, UNT. 58

Figure 3.14: DC-SQUID with two Josephson junctions placed in the magnetic field. 60

Figure 3.15: A schematic representation of DC-SQUID with two Josephson junctions, J_1 and J_2 61

Figure 4.1: A 4" diameter n-type 4*H*-SiC wafer was diced to smaller pieces at American Dicing Inc., USA. 67

Figure 4.2: A typical RBS yield due to an angular scan across the channeling axis of 4*H*-SiC performed with 2 MeV He^+ beam. 69

Figure 4.3 : Channel number to Energy conversion plot. 72

Figure 4.4 : SIMNRA of virgin SiC 73

Figure 4.5 : Schematics of Energy Loss and Depth Conversions. 74

Figure 4.6 : RBS-C spectra of 60 keV C implanted 4*H*-SiC samples at room temperature using a 2 MeV He^+ beam. The increase in backscattering signal (between channel 500 and 570) indicates the increase in the disorder due to increase in ion fluence. 79

Figure 4.7: RBS-C spectra of C implantation in 4*H*-SiC in Si sub-lattice region. 80

Figure 4.8 : Linear Plot of dE/dX of ^{4}He in SiC used to evaluate the depth profile. The energy loss value of electronic and nuclear collision can be determined using SRIM-2011. 81

Figure 4.9 : Relative disorder of the Si sub-lattice in 60 keV C implanted 4*H*-SiC samples as a function of depth. The depth of the damage peak was found to be 110±10 nm. Si vacancy density was calculated by multiplying relative disorder with atomic density of Si (4.82×10^{22} atoms/cm^3) in 4*H*-SiC. 82

Figure 4.10 : RBS-C spectra of Si implantation in 4*H*-SiC. 84

Figure 4.11 : RBS-C spectra of Si implanted 4*H*-SiC in Si sub-lattice region. 85

Figure 4.12 : Relative disorder of the Si sub-lattice in 60 keV Si implanted 4*H*-SiC samples as a function of depth. The depth of the damage peak was found to be 50±5 nm. Si vacancy

density was calculated by multiplying relative disorder with atomic density of Si (4.82×10^{22} atoms/cm^3) in 4*H*-SiC...86

Figure 4.13 : Raman spectra of 60 keV C implanted at different fluences in 4*H*-SiC. 87

Figure 4.14: Raman spectra of low energy 60 keV C implanted 4*H*-SiC samples. The TO (775 cm^{-1}) and LO (964 cm^{-1}) mode signals are compared in order to determine the amount of disorder in the implanted samples...89

Figure 4.15: Raman spectra of 60 keV Si implanted at different fluences in 4*H*-SiC..................90

Figure 4.16: Raman spectra of low energy 60 keV Si implanted 4H-SiC samples. The TO (775 cm^{-1}) and LO (964 cm^{-1}) mode signals are compared in order to determine the amount of disorder in the implanted samples...91

Figure 4.17: Relative disorder of 60 keV C implanted at different fluences in 4*H*-SiC from RBS-C and the TO and LO modes of Raman spectra. 92

Figure 4.18: Relative disorder of 60 keV Si implanted at different fluences in 4*H*-SiC from RBS-C and TO and LO modes of Raman spectra. 93

Figure 4.19: An optical image of a specially designed SQUID sample holder. n-type 4*H*-SiC sample is secured inside the quartz tube. The sample stayed inside the tube to test the compatibility before and after implantation...100

Figure 4.20: Magnetization at (a) room temperature 300 K and (b) low temperature 5K as a function of applied magnetic field for the same n-type 4*H*-SiC sample before (virgin) and after carbon-implantation. The implanted fluence 5×10^{12} ions/cm^2 corresponds to an average distance between vacancies of 1.94 nm as estimated from TRIM simulations. In (c) and (d) the magnetization is plotted without the diamagnetic contribution m_{lin} to

identify any ferromagnetic contribution due to carbon irradiation. The data show no significant difference in the magnetization between virgin and implanted sample.........101

Figure 4.21: Magnetization as a function of magnetic field for virgin and implanted C fluence of 1×10^{12} ions/cm^2 and 1×10^{13} ions/cm^2 at 5K. These fluences correspond to the average distance between vacancies of 3.33 and 1.54 nm respectively as estimated from TRIM simulations. 102

Figure 4.22: Magnetization as a function of magnetic field for the C implanted n-type 4*H*-SiC at low energy 60 keV with fluence 8.5×10^{14} ions/cm^2 at 300 K and 5K............................103

Figure 4.23: Magnetization as a function of magnetic field for the C implanted n-type 4*H*-SiC at low energy 60 keV with fluence 5×10^{15} ions/cm^2 at 300 K and 5K...............................104

Figure 4.24: Magnetization as a function of magnetic field for the C implanted n-type 4*H*-SiC at low energy 60 keV with fluence 1.7×10^{16} ions/cm^2 at 300 K and 5K............................105

Figure 4.25: FC/ZFC magnetization curves for the virgin n-type 4*H*-SiC.................................106

Figure 4.26: FC/ZFC magnetization curves for the C implanted n-type 4*H*-SiC at low energy 60 keV with fluence 1×10^{12} ions/cm^2. 107

Figure 4.27: FC/ZFC magnetization curves for the C implanted n-type 4*H*-SiC at low energy 60 keV with fluence 1×10^{13} ions/cm2. 108

Figure 5.1: TRIM plots for N implantation in 4*H*-SiC at the higher energy of 1 MeV. (a) collision cascade between implanted N ions and SiC, (b) ion-distribution plot, (c) collision events which shows the displacements in the target and (d) energy to recoil atoms. 116

Figure 5.2: RBS-C spectra of 1 MeV N implanted 4*H*-SiC samples at room temperature analyzed using 3.5 MeV He^+ beam. 118

Figure 5.3: Energy loss (dE/dx) of He in 4*H*-SiC from energy 500 – 4000 keV. 120

Figure 5.4: Relative disorder of Si sub-lattice as a function of depth...121

Figure 5.5: Raman shift spectra of high energy (1 MeV) N implanted 4*H*-SiC..........................122

Figure 5.6: Raman spectra of 1 MeV N implanted 4H-SiC samples. The TO (775 cm^{-1}) and LO (964 cm^{-1}) mode signals are compared in order to determine the relative amount of disorder in the implanted samples..123

Figure 5.7: Relative Disorder of high energy (1 MeV) N implanted in 4*H*-SiC obtained from Raman measurements comparing the TO and LO modes. 124

CHAPTER 1

INTRODUCTION

1.1 Motivation

Silicon (Si) has been the focus of research for semiconductor applications for over 50 years and for this reason is one of the most characterized materials for electronic applications. Commercially, most semiconductors devices are produced based on Si technology. Despite having great applications in the field of microelectronics, Si devices cannot withstand extreme conditions such as high temperature, high power, and high frequency. However; silicon carbide (SiC) with its polytypism nature, wide band gap, high thermal conductivity, and unique physical and mechanical properties superior to Si, is well matched for demanding applications in harsh environments and radiation resistant applications [1 - 3]. Various devices can be fabricated using SiC that are not possible using Si. Increased research into SiC devices has come from the fabrication of high quality devices. Commercially, SiC devices are widely used for numerous applications in nuclear power, military/civilian, various optical devices, and radar/communication systems in space [4 - 7].

In addition to the aforementioned applications, SiC is also considered to be the prospective candidate for spintronic applications [8, 9]. Spintronics is a promising science and emerging field in this era of information technology leading to new devices which can not only use the charge of electrons and holes but also their spins. Spin polarization (magnetic moments) can be created by introducing transition metal impurities such as Ni, Cr, Mn, and Fe into the semiconductor host lattice. The magnetic moments induced in this transition metal doped SiC arise from partially filled and spin-polarized d or f electronic shells. Ferromagnetism was

detected not only in transition metal doped SiC but also in transition metal-free SiC. The defects, typically vacancies created in SiC found to play an important role in inducing magnetic moments. These vacancies are more stable at room temperature as compared to the defects that are created in transition-metal doped SiC.

Defects can be created in semiconductors by various techniques such as ion implantation, crystal growth, and other doping techniques. Out of all these available techniques, ion implantation is considered to be a key technology since the energy and range of the dopants can be controlled. The defects created after implantation can be characterized using many techniques; such as Rutherford backscattering spectrometry in the channeling mode (RBS-C), Raman spectroscopy, positron annihilation spectroscopy (PAS), electron spin resonance (ESR), photoluminescence (PL), and deep level transient spectroscopy (DLTS). This dissertation focuses mainly on creating defects with low energy (60 keV) C, Si, and high energy (1 MeV) N ions in 4*H*-SiC by ion implantation and studying the defect characterization by RBS-C and Raman spectroscopy. Further, the magnetic measurements were done only on the C implanted samples in n-type 4*H*-SiC using superconducting quantum interference device (SQUID) magnetometer.

1.2 Magnetism in Materials

Several materials behave differently in the presence of external magnetic field. This induced magnetism depends on atomic and molecular structure of the material and the net magnetic field associated with the atoms. Atoms can have either paired or unpaired electrons. In paired electrons, the spin is in opposite direction which causes the magnetic fields to cancel each other. On the other hand, the unpaired electrons will have a net magnetic field and reacts more to the external applied magnetic field. Magnetism in materials can be classified as (a) diamagnetism

(b) paramagnetism and (c) ferromagnetism [10]. Figure 1.1 shows the ordering of paramagnetism, ferromagnetism and anti-ferromagnetism in the material when the external magnetic field is applied.

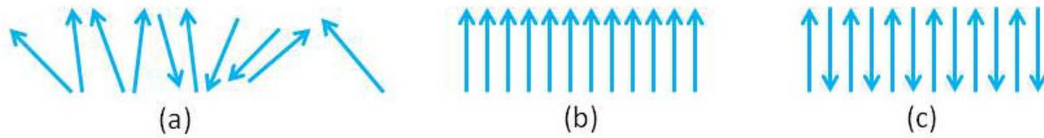

Figure 1.1: Ordering of (a) paramagnetism (b) ferromagnetism and (c) anti-ferromagnetism.

1.2.1 Diamagnetism

Diamagnetic materials become magnetized only when an external magnetic field is applied and loses magnetization as soon as the external field is removed. These materials have a weak, negative susceptibility and slightly repelled by the external applied magnetic fields. Diamagnetic properties arise due to the realignment of the electron paths caused by the external magnetic field. In diamagnetic materials, the induced dipole moment and the intensity of magnetization is a small negative value. The properties of diamagnetic materials do not change with temperature. Some of the diamagnetic materials are gold, silver, quartz, and bismuth.

1.2.2 Paramagnetism

Paramagnetic materials also become magnetized only when an external magnetic field is applied and loses magnetization as soon as the external field is removed. However, these materials have a small positive susceptibility and slightly attracted by the external applied magnetic fields. These properties exhibit due to the unpaired electrons and from the realignment of the electron paths caused by the external magnetic field. The induced dipole moment and the intensity of magnetization is a small positive value in paramagnetic materials. The magnetic properties are lost when the temperature is increased in paramagnetic materials. Aluminum, chromium, alkali and alkaline earth metals are examples of paramagnetic materials.

1.2.3 Ferromagnetism

Ferromagnetic materials have a large magnetization and retain it after the external magnetic field is removed. These materials have a large, positive susceptibility when applied to an external magnetic field. Magnetic properties in these materials evolve due to the combination of magnetic moments of the atoms and the magnetic domains. The domains can be defined as the region of many atoms with aligned dipole moments. The induced dipole moment and the intensity of magnetization in these materials have a large positive value. Iron, cobalt, nickel come under the category of ferromagnetic materials. In ferromagnetism, all the spins are aligned in one single direction resulting in parallel alignment of the spins. In anti-ferromagnetic materials, the magnetic moments of the atoms align with the neighboring spins in opposite directions which results in a complete cancellation of net magnetization results.

A typical diagram of hysteresis loop is shown in the Figure 1.2. The information about the magnetic properties of a material can be obtained by studying this hysteresis loop. The loop 123456 is called hysteresis loop and shows the relationship between the magnetization, M and the applied magnetic field, H. As the applied magnetic field in the ferromagnetic material increases, the magnetization increases and saturates at the Point 1. At this point which is called as *saturation point*, all the magnetic domains are aligned and the increase in the magnetic field does not affect the magnetization. When the magnetic field is reduced to zero, the curve reaches to Point 2 from Point 1. This point is called *retentivity* which tells about the residual magnetism and is due to the loss of alignment of some of the magnetic domains in the material. Point 3 refers to the *coercivity* of the material where the magnetization becomes zero as the applied magnetic field is reversed. The coercive force is defined as the force required removing the residual magnetism from the material.

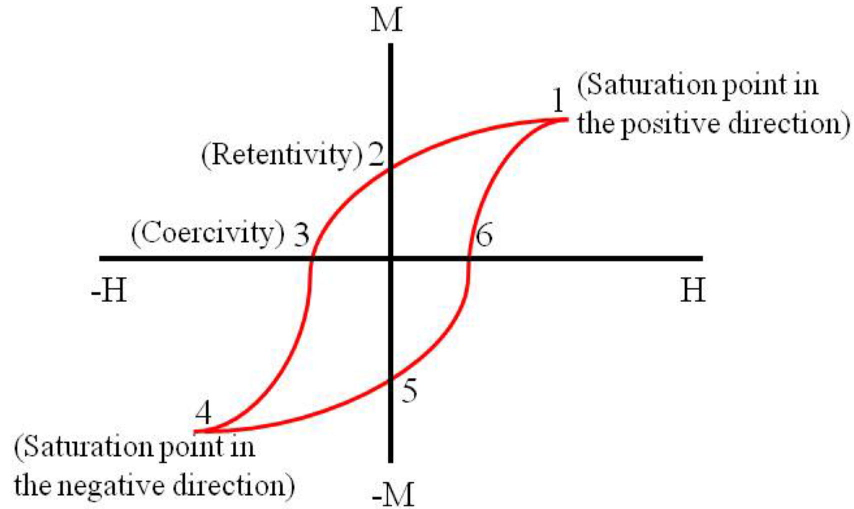

Figure 1.2: Hysteresis loop showing the relationship between magnetization, M and the applied magnetic field, H.

As the applied magnetic field is increased in the reverse direction, the curve follows the path to Point 4 which is called *saturation point* in the opposite direction. Point 5 refers to the magnetization when the applied magnetic field is reduced to zero. Point 5 has some magnetization and is not equal to zero because of the residual magnetism present in the material. As the magnetic field is increased in the positive direction, the curve ends at the Point 6.

The magnetic susceptibility is defined as the ratio of magnetization to magnetic field strength and is given as: $\chi = M/H$. The value of χ can be used to determine the magnetic nature of the material. Diamagnetic material has a negative susceptibility where as paramagnetic material has a small positive susceptibility. The susceptibility in ferromagnetic material is large and positive. Curie temperature or Curie point is defined as the temperature at which the ferromagnetic material loses its ferromagnetic properties and becomes paramagnetic material [10]. At temperatures above the Curie temperature, the magnetic domains are misaligned and the long range order between these domains disappears thus making the net magnetization zero in the ferromagnetic material. SiC is a binary compound which is made up of Si and C atoms. The

atomic number of Si is 14 and the electronic configuration is $1s^22s^22p^63s^23p^2$ whereas C has an atomic number of 6 with electronic configuration of $1s^22s^22p^2$. This binary compound has negative susceptibility and exhibit diamagnetic properties. However, ferromagnetism was observed in this non-magnetic material when doped with transition-metals and as well as with the vacancies created in SiC [11-19]. More details about this phenomenon are discussed in the following section.

1.3 Literature Review on Ferromagnetism Behavior of SiC

High Curie temperature ferromagnetism has been predicted for certain wide band gap semiconductors using the Zener model [20]. The room temperature ferromagnetism has been already reported for the systems (Zn, Co) O; (Co, Ti) O_2; $ZnSnAs_2$ [21 - 23]. There have been numerous papers published in the computational and theoretical aspects of electron spin physics in magnetically doped semiconductors [24 - 30]. Out of the available wide band gap semiconductors, SiC is considered to be a promising material for dilute magnetic semiconductors (DMS). Past experimental studies reveal that ferromagnetism can be observed in SiC diluted with 3d transition metals. SQUID measurements showed that a Curie temperature of 50 K was observed for 3 and 5 atomic percent (at.%) of Ni doped in p-type 6*H*-SiC. Fe and Mn exhibited paramagnetic at 3 at.% where as at 5 at.% a Curie temperature of 270 and 250 K was observed [11]. Kwang et al. have investigated the magnetic properties of Fe-doped SiC bulk ceramics. The observed magnetization in this Fe-doped sample was mainly attributed to the Fe_3Si crystallites and the ferromagnetic alignment of individual magnetic moments of the Fe^{3+} ions randomly substituting the Si sites of the sample. [12]. Jin et al. have investigated the magnetic signals in amorphous-SiC doped with Cr. From SQUID measurements the saturation moment at room temperature increased from 0.18 μ_B (where μ_B is the Bohr magneton and is defined as the

unit to express an electron magnetic dipole moment) to 0.27 μ_B per Cr atom by increasing the Cr content from 7 to 10 at.% [13]. Various studies have been done on Mn doped SiC and the results show high ferromagnetic ordering temperatures [14 - 18]. The formation of local magnetic moments in these transition metal doped SiC are due to the strongly localized nature of 3d and 4f states which are coupled with high degree of degeneracy which favors the spin-polarized electronic configurations. Ferromagnetism was detected not only in transition metal doped SiC but also in transition metal-free SiC. Ferromagnetism was observed with the implantation of Ne^+ ions in semi-insulating 4*H*-SiC and found to be stable upon thermal annealing at 1400 °C [19].

Along with the above mentioned experimental results, as well as other publications based on the density functional theory (DFT) and using various ab initio computational simulations, it has been shown that DMS can be created by introducing magnetic ions such as V, Cr and Mn into various polytypes of SiC [31 - 33]. Zhuo et al. have investigated the first principle calculations of SiC doped with Ni, Co, and Fe, the results show that the local spins lead to different magnetic properties for Ni and Cu, and ferromagnetism for Fe [34]. The ferromagnetism obtained in the transition metal doped SiC is mainly due to the partially-filled d or f sub shells. Recently, non-transition metal doped SiC are investigated due to their importance for high temperature spintronic materials, where defects can play an important role. Using the first-principle calculations, the roles of silicon vacancy (V_{Si}) in the magnetic properties of SiC was explored. Negatively charged silicon vacancy defects showed high-spin configurations [35]. Besides the ability of transition metals to locate on Si or C substitution sites, vacancies may create spin polarization. Recent studies, based on first principle calculations, show that for SiC monolayers the presence of silicon vacancies (V_{Si}) may induce local magnetization, however, no spin polarization occurs for carbon vacancies (V_C), Si+C divacancies, and Si-C anti-site defects

[36, 37]. The diffusion of vacancy defects, and atomic structure in carbon related materials, such as carbon nanotubes, graphene, have been investigated in a number of theoretical calculations [38 - 41]. High spin states of cation vacancies were observed particularly in 4*H*-SiC [42]. Possible formation of a magnetic phase in the bulk sample and magnetic properties of vacancies were examined in a number of studies [43 - 48].

Rutherford backscattering spectrometry in channeling mode (RBS-C) and Raman spectroscopy are two complementary techniques used to study defects in SiC. Structural defects in 4*H*- and 6*H*-SiC using these two techniques with different ion implantations have been studied by various authors. Bolse et al. have investigated the amorphization of 6*H*-SiC by Na ions of energy 100 and 155 keV. They have found that 0.1 displacements per atom (dpa) is needed for amorphization [49]. The disorder behavior and amorphization of Fe ions in 6*H*- and 3*C*-SiC were studied by Debelle et al. The results show that 0.7 dpa is needed for amorphization of the SiC material [50]. Jiang et al. have studied the damage accumulation of 6*H*-SiC irradiated with different ions and at different temperatures [51 - 55]. They also investigated the displacement energy measurements for ion-irradiated 6*H*-SiC with He^+, C^+, and Si^+ ion beams [56]. Zolnai et al. studied the ion-implantation induced damage in 6*H*-SiC by 200 keV energy Al^+ ions and 500 keV energy N^+ ions. They investigated the damage accumulation in both Si and C sub-lattice using RBS-C [57, 58].

RBS-C is mostly used for lattice location and the study of interstitials whereas positron annihilation spectroscopy (PAS) can be used for studying the various types of vacancy defects in solid materials. One of the semiconductors extensively studied using PAS is SiC. Most of the papers reviewed involve irradiated materials [59 – 68]. The concentrations and lifetime of different vacancy defects can be easily determined using PAS.

Raman spectroscopy is a nondestructive technique which is used for characterizing the semiconductor materials [69 – 71]. This technique is widely used for polytype identification [72] and as well as to study the defects in SiC [73, 74]. Rodriguez et al. have investigated the damage analysis in Ge^+ ion implantation in 6*H*-SiC. The results showed three different damage levels for the fluence ranging from 10^{12} to 10^{14} cm^{-2} [75]. Wendler et al. have investigated the damage formation in neutron irradiated 4*H*- and 6*H*-SiC. The results showed the decrease in peak intensity and shift of the phonon modes towards lower wave numbers which was caused due to the defects [76]. Several groups have studied the structure of neutron irradiated SiC [77 – 80].

The vacancies can play an important role in creating localized magnetic moments. Ramos et al. have investigated the ferromagnetism in highly oriented pyrolitic graphite (HOPG) using MeV energy H, C and N ions. The induced spin polarization was related to the mean vacancy distance and the high hydrogen concentration at the near surface region. The results indicate that the mean distance between the neighboring vacancies should be the order of about 2 nm [81]. He et al. have shown that the vacancies are responsible for inducing ferromagnetism in C ion implanted HOPG [82]. Esquinazi et al. have investigated the magnetic order in graphite implanted with protons at energy 2.25 MeV [83]. The results obtained in this work show that the largest signal due to the induced magnetic order is produced at a distance between vacancies of 1.5 nm. The mean distance of the vacancies is exclusively dependent on the vacancy concentration created in the target materials. The vacancy concentration can be controlled by the amount of fluence ($ions/cm^2$) implanted into the materials. Thus, there is a narrow window of values of different irradiation parameters, such as fluence, energy, and ion species which plays an important role in creating magnetic signals.

1.4 Summary of Chapters in this Thesis Work

An overview of the properties of SiC materials is given in Chapter 2. The chapter starts with the crystal structures of SiC and different polytypes. The properties such as mechanical, thermal, electronic and optical are also discussed in this chapter. The studies of defects are one of the important research fields in semiconductor physics. Therefore different types of defects in SiC are discussed in this chapter and the chapter is concluded with the potential applications of SiC.

In Chapter 3 the theoretical simulations of interaction of energetic ions in solid and different experimental characterization techniques employed in this study are described. Details of the ion beam facility at the Ion Beam Modification and Analysis Laboratory (IBMAL) at UNT are briefly discussed. Low energy (60 keV) Si and C ions are implanted into 4*H*-SiC using a source of negative ion by cesium sputtering – II (SNICS) at the IBMAL. Ion fluences in the ranges between 10^{12} and 10^{15} atoms/cm^2 were chosen to create different amounts of defect densities. The implantation events were simulated using a computer simulations code stopping and range of ions in matter (SRIM) / transport of ions in matter (TRIM) – 2011 based on Monte Carlo technique. These simulations are used later in the research for theoretical calculations of irradiation parameters for implanted samples in 4*H*-SiC. The chapter is concluded with a detailed discussion about the underlying theory of the experimental techniques that were used in this research study such as, RBS-C, Raman spectroscopy and SQUID.

In Chapter 4, the experimental result of this research is discussed. After the implantation, the depth profiling of created defects is investigated using RBS-C. The relative disorders are examined in all the implanted samples using RBS-C and Raman techniques. The chapter

concludes with the discussion of the magnetic behavior results obtained for 60 keV C implanted n-type 4*H*-SiC using SQUID measurements.

In Chapter 5, the results and discussions are presented about characterization of defects in a deeper layer due to implantation of N ions in n-type 4*H*-SiC at a higher energy (1 MeV).

A summary of the theoretical and experimental results of C, Si, and N ion implantation in n-type 4*H*-SiC along with SQUID measurements in C implanted n-type 4*H*-SiC is provided in Chapter 6. Based on the experiments results so far, an outline of the future work is discussed in the concluding part of this chapter.

1.5 References

1. W. J. Choyke, H. Matsunami, G. Pensl, Silicon Carbide: Recent Major Advances, Springer Series, Berlin (2004).
2. C. Buttay, D. Planson, B. Allard, D. Bergogne, P. Bevilacqua, C. Joubert, M. Lazar, C. Martin, H. Morel, D. Tournier, C. Raynaud, Mater. Sci. Eng. *B* **176** 283 (2011).
3. F. Zhao, M. M. Islam, P. Muzykov, A. Bolotnikov, T. S. Sudarshan, IEEE Electron Device Letters **30** 1182 (2009).
4. P. Godignon, X. Jorda, M. Vellvehi, X. Perpina, V. Banu, D. Lopez, J. Barbero, P. Brosselard, S. Massetti, IEEE Trans. on Ind. Elect. **58**(7) 2582 (2011).
5. M. R. Fard, T. E. Blue, D. W. Miller, AIP Conf. Proc. **699** 574 (2004).
6. S. Metzger, H. Henschel, O. Kohn, W. Lennartz, IEEE Trans. on Nucl. Sci. **49**(3) 1351 (2002).
7. H. S. Kim, J. H. Ha, S. Park, S. W. Lee, M. K. Moon, G. Sun, C. H. Lee, J. of Nucl. Sci. and Tech. **48**(10) 1342 (2011).
8. C. Chappert, A. Fert, F. N. Van Dau, Nat. Mater. **6** 813 (2007).

9. S. A. Wolf, D. D. Awschalom, R. A. Buhrman, J. M. Daughton, S. von Molnar, M. L. Roukes, A. Y. Chtchelkanova, D. M. Treger, Science **294** 1488 (2001).
10. Charles Kittel, Introduction to Solid State Physics, 8th edition, Wiley Publications, USA (2005).
11. N. Theodoropoulou et al., J. Vac. Sci. Technol. A **20** 579 (2002).
12. K. Kwang, K. Young-Wook, J. European Ceramic society **32** 1149 (2012).
13. C. Jin, X. Wu, L. Zhuge, Z.Sha, B. Hong, J.Appl. Phys. D: Appl. Phys. **41** 035005 (2008).
14. S. Ma, Y. Sun, B. Zhao, P. Tong, X. Zhu, W. Song, Physica B: Condensed Matter **394** 122 (2007).
15. W. Wang, F. Takano, H. Akinaga, H. Ofuchi, Phys. Rev. B **75** 165323 (2007).
16. W. Wang, F. Takano, H. Ofuchi, H. Akinaga, New J. Phys. **10** 055006 (2008).
17. B. Song, H. Bao, H. Li, M. Lei, J. Jian, J. Han, X. Zhang, S. Meng, W. Wang, X. Chen, Appl. Phys. Lett. **94** 102508 (2009).
18. K. Bouziane, M. Mamor, M. Elzain, P. Djemia, S. Cherif, Phys. Rev. B **78** 195305 (2009).
19. L. Lin, H. Wei, P. Slawomir, Y. Shu-De, S. Lin, P. Kay, Z. Shengqiang, Nuc. Instr. and Meth. B **275** 33 (2012).
20. T. Dietl, H. Ohno, F. Matsukara, J. Cibert, D. Ferrand, Science **287** 1019 (2000).
21. S. Choi, G. B. Cha, S. C. Hong, S. Cho, Y. Kim, J. B. Ketterson, S. Y. Jeong, G. C. Yi, Solid State Commun. **122** 165 (2002).
22. K. Ueda, H. Tahata, T. Kawai, Appl. Phys. Lett. **79** 988 (2001).

23. Y. Matsumoto, M. Murakami, T. Shono, H. Hasegawa, T. Fukurama, M. Kawasaki, P.T. Ahmet, T. Chikyow, S. Koshikara, H. Koinuma, Science **291** 854 (2001).
24. Y. Kim, Y. Chung, S. Yi, Materials Science and Engineering B **126** 194 (2006).
25. J. Ren-Xu, Z. Yu-Ming, Z. Yi-Men, Chin. Phys. B **19** 107105 (2010).
26. O. Yazyev, L .Helm, Phys. Rev. B **75** 125408 (2007).
27. L. Qing, N. Jun, Science China **53** 1 (2010).
28. M. Zhao, F. Pan, L. Mei, Appl. Phys. Lett. **96** 012508 (2010).
29. Z. Huang, Q. Chen, J. Magn. Mater. **313** 11 (2007).
30. F. Stromberg, W. Keune, X. Chen, S. Bedanta, H. Reuther, A. Mucklich, J. Phys. Condens. Matter **18** 9881 (2006).
31. A. Los and V. Los, J. Phys. Condens. Matter **22** 245801 (2010).
32. F. Stromberg et al., J. Phys. Condens. Matter **18** 9881 (2006).
33. Y. Kim et al., Key Engineering Materials Vols. **317-318** 889 (2006).
34. J. Zhou, H. Li, L. Zhang, J. Cheng, H. Zhao, W. Chu, J.Yang, Y. Luo, Z. Wu, J. Phys. Chem. C **115** 253 (2011).
35. M. Zhao, F. Pan, L. Mei, Appl. Phys. Lett. **96** 012508 (2010).
36. X. He, T. He, Z. Wang and M. Zhao, Physica E **42**(9) 2451 (2010).
37. E. Bekaroglu, M. Topsakal, S. Cahangirov, S. Ciraci, Phys. Rev. B **81** 075433 (2010).
38. E. Kaxiras, K. C. Pandey, Phys. Rev. Lett. **61** 2693 (1988).
39. A. A. El-Barbary, R. H. Telling, C. P. Ewels, M. I. Heggie, P. R. Briddon, Phys. Rev. B **68** 144107 (2003).
40. M. Sammalkorpi, A. Krasheninnikov, A. Kuronen, K. Nordlund, K. Kaski, Phys. Rev. B **70** 245416 (2004).

41. G. D. Lee, C. Z. Wang, E. Yoon, N. M. Hwang, D.Y. Kim, K. M. Ho, Phys. Rev. Lett. **95** 205501 (2005).
42. N. Mizuochi, S. Yamasaki, H. Takizawa, N. Moroshita, T. Ohshima, H. Itoh, T. Umeda, J. Isoya, Phys. Rev. B **72** 235208 (2005).
43. S. M. Evans, N. C. Giles, L. E. Halliburton, L. A. J. Kappers, Appl. Phys. **103** 043710 (2008).
44. B. H. Rose, L. E. Halliburton, J. Phys. C: Solid Stat. Phys. **7** 3981 (1974).
45. L. E. Halliburton, D. L. Cowan, W. B. J. Blake, J. E. Wertz, Phys. Rev. B **8** 1610 (1973).
46. T. A. Kennedy, N. D. Wilsey, J. J. Krebs, G. H. Stauss, Phys. Rev. Lett. **50** 1281 (1983).
47. D. Galland, A. Herve, Phys. Lett. **33A** 1 (1970).
48. L. S. Vlasenko, G. D.Watkins, Phys. Rev. B **72** 035203 (2005).
49. W. Bolse, J. Conrad, T. Rodle, T. Weber, Surface and Coatings Technology **74-75** 927 (1995).
50. A. Debelle, L. Thome, D. Dompoint, A. Boulle, F. Garrido, J. Jagielski, D. Chaussende, J. Phys. D : Appl. Phys. **43** 455408 (2010).
51. W. Jiang, H. Wang, I. Kim, Y. Zhang, W. Weber, J. Mater. Res. **25** 2341 (2010).
52. W. Jiang, W. Weber, J. Nucl. Mater. **389** 332 (2009).
53. W. Jiang. Y. Zhang, M. Engelherd, J. Appl. Phys. **101** (2007).
54. Y. Zhang, F. Gao, W. Jiang, D. McCready, Materials Science Forum **475-479** 1341 (2005).
55. W. Jiang, W. Weber, S. Thevuthasan, V. Shutthanandan, J. Nucl. Mater. **289** 96 (2001).
56. W. Jiang, W. Weber, S. Thevuthasan, D. McCready, Nucl. Instru. Methods in Research B **148** 557 (1999).

57. Z. Zolnai, N. Q. Khanh, E. Szilagyi, E. Kotai, A. Ster, M. Posselt, T. Lohner, J. Gyulai, Diamond and Related Materials **11** 1239 (2002).

58. Z. Zolnai, A. Ster, N. Q. Khanh, G. Battistig, T. Lohner, J. Gyulai, E. Kotai, M. Posselt, J. App. Phys. **101** 023502 (2007).

59. R. S. Yu, M. Maekawa, A. Kawasuso, B. Y. Wang, L. Wei, Nucl. Instru. Methods in Research B **270** 47 (2012).

60. Q. Xu, T. Yoshile, M. Okade, J. Nucl. Mater. **386** 169 (2009).

61. S. Dannefaer, D. Kerr, Diamond and Related Materials **13** 157 (2004).

62. W. E. Carlos, N. Y. Garces, E. R. Glaser, Phys. Rev. B **74** 235201 (2006).

63. A. Kawasuso, M. Yoshikawa, H. Itoh, R. Krause-Rehberg, F. Redmann, T. Higuchi, K. Betsayuku, Physica B **376-377** 350 (2006).

64. H. Wang, H. Weng, X. Zhou, Chinese J. Chem. Phys. **21** 333 (2008).

65. G. Brauer, W. Anwand, P. G. Coleman, W. Skorupa, Vacuum **78** 131 (2005).

66. G. Brauer, W. Anwand, P. G. Coleman, A. P. Knights, F. Plazaola, Y. Pacaud, W. Skorupa, J. Stormer, P. Willutzki, Phys. Rev. B **54** 3084 (1996).

67. E. Rauls, T. E. M. Staab, Z. Hajnal, Th. Frauenheim, Physica B **308-310** 645 (2001).

68. A. Polity, S. Huth, M. Lausmann, Phys. Rev. B **59** 10603 (1999).

69. W. J. Li, C. Y. Kong, H. B. Ruan, G. P. Qin, G. J. Huang, T. Y. Yang, W. W. Liang, Y. H. Zhao, X. D. Meng, P. Yu, Y. T. Ciu, L. Fang, Sol. Stat. Commn. **152**(2) 147 (2012).

70. H. Zhao, H. Fu, T. Zhao, L. Wang, T. Tan, J. Coll. Inter. Scie. **375**(1) 30 (2012).

71. S. M. Basha, K. Asokan, P. Sangeetha, V. Ramakrishnan, J. Kumar, Mat. Chem. And Phys. **132**(2-3) 494 (2012).

72. S. Nakashima and H. Harima, Phys. Stat. Sol. (a) **162** 39 (1997).

73. Y. Tang, H. Ru, W. Ping, Chin. Phys. B **17**(9) 3459 (2008).

74. S. Lin, Z. Chen, Y. Ba, M. Yang, L. Li, Mat. Lett. **81** 27 (2012).

75. A. Rodriguez, Y. Pacaud, L. Barrio, C. Serre, W. Skorupa, J. R. Morante, J. Elec. Mater. **25** 3 (1996).

76. E. Wendler, Th. Bierschenk, F. Felgentrager, J. Sommerfeld, W. Wesch, D. Alber, G. Bukalis, L. C. Prinsloo, N. van der Berg, E. Friedland, J. B. Malherbe, Nucl. Instru. Methods in Research B **286**(1) 97 (2012).

77. S. Sorieul, J. M. Constantini, L. Gosmain, L. Thome, J. J. Grob, J. Phys. Condens. Matter. **18** 5235 (2006).

78. J. J. Li, C. H. Zhang, C. L. Xu, X. J. Jia, Y. Song, J. Y. Li, Y. F. Jin, Nucl. Instru. Methods in Research B **286**(1) 124 (2012).

79. P. F. Wang, L. Huang, W. Zhu, Y. F. Ruan, Sol. Sta. Commn. **152**(10) 887 (2012).

80. A. A. Suvorova, S. Rubanov, A. V. Suvorov, Nucl. Instru. Methods in Research B **272** 1 462 (2012).

81. M. A. Ramos, J. Barzola-Quiquia, P. Esquinnazi, A. Munoz-Martin, A. Climent-Font, M. Garcia-Hernandez, Phys. Rev. B **81** 214404 (2010).

82. Z. He, X. Yang, H. Xia, X. Zhou, M. Zhao, Y. Song, T. Wang, Carbon **49** 1931 (2011).

83. P. Esquinazi, J. Barzola-Quiquia, D. Spemann, M. Rothermal, H. Ohldag, N. Garcia, A. Setzer, T. Butz, J. Magn. Magn. Mater **322** 1156 (2010).

CHAPTER 2

OVERVIEW OF SILICON CARBIDE

2.1 Crystal Structure and Structural Properties

SiC is the only stable group IV compound semiconductor. SiC is a binary compound with Si-C bonds of 12% ionic and 88% covalent. As shown in the Figure 2.1 four Si(C) atoms are strongly bonded with sp^3-tetrahedral bond with C (Si) atoms. The distance between the carbon atoms is 3.08 Å and the distance between silicon and carbon atom is 1.89 Å.

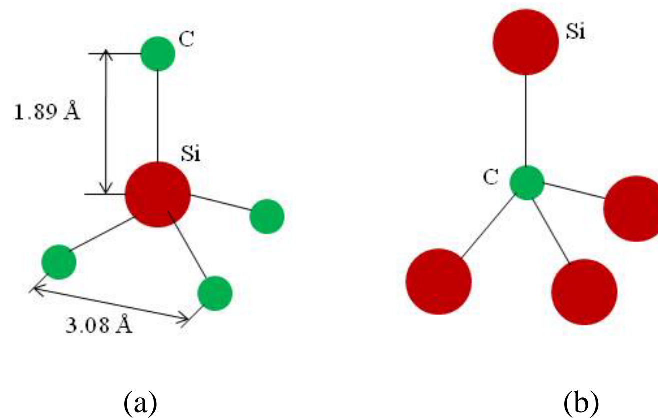

Figure 2.1: Tetrahedron building block of SiC crystal. (a) Four carbon atoms bonded to one silicon atom (b) Four silicon atoms bonded to one carbon atom.

SiC is one of the many compounds that exhibit polymorphism. It has a one dimensional polymorphism, called polytypism, which means that it can have more than one crystal structure. Until now, more than 250 polytypes of SiC have been found [1] and the only cubic polytype present is 3*C*-SiC, which is called as β-SiC. The other structures are 2*H*-SiC, 4*H*-SiC, 6*H*-SiC (hexagonal structures), and 15*R*-SiC, 21*R*-SiC, 33*R*-SiC (rhombohedral structures). All the other polytypes, except cubic polytype, are called as α-SiC. The number in the above polytypes represents the number of layers before the sequence repeats and the letter denotes the resulting

crystal structure. This kind of representation where number is followed by a letter for different polytypes is denoted by Ramsden notation and is shown in Table 2.1 [2].

Table 2.1: Notations of four common SiC polytypes and corresponding inequivalent lattice sites.

SiC polytype	ABC notation	No. of hexagonal-like inequivalent sites	No. of cubic-like inequivalent sites
2*H*	AB	1	0
3*C*	ABC	0	1
4*H*	ABCB	1	1
6*H*	ABCACB	1	2

The polytypes can be constructed by a stacking sequence of closely packed spheres; each plane of the sphere contains Si atoms lying exactly above the C atoms along the stacking axis denoted by the c-axis. Thus, the crystalline structure of SiC is characterized by different repetitions of stacking sequence of layers A, B and C. For example; if the first double layer is denoted as position A, the next layer on top of A would be B or C position according to the closed packed structure. The combination of these three different positions makes SiC have different polytypes. For the case of simple hexagonal structure 2*H*-SiC the stacking sequence is ABABAB. . . Similarly, for 3*C*-SiC, the stacking sequence is ABCABCABC. . . The same goes with 4*H*-SiC and 6*H*-SiC for which the stacking sequence is ABCBABCB. . . and ABCACBABCACB. . ., respectively. This stacking order between succeeding double layers of silicon and carbon atoms is what makes each of the polytypes of SiC different from one another. The stacking sequence of most common polytypes is shown in the Figures 2.2, 2.3, and 2.4. These polytypes were obtained from the database of Materials Design Software, MedeA [3].

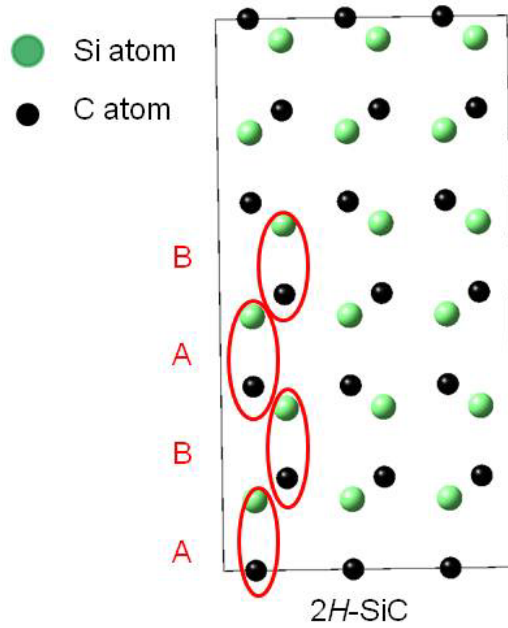

Figure 2.2: Stacking sequence of double layers of 2*H*- SiC polytype obtained from the database of Materials Design Software, MedeA.

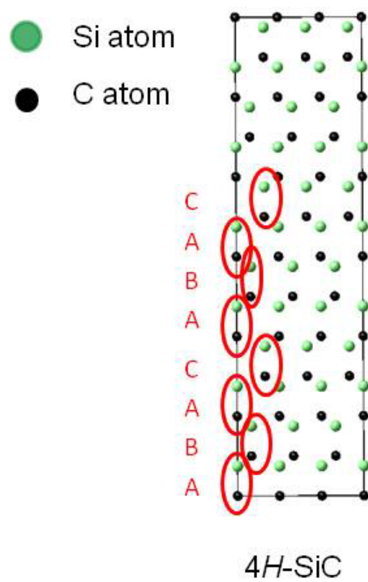

Figure 2.3: Stacking sequence of double layers of 4*H*- SiC polytype obtained from the database of Materials Design Software, MedeA.

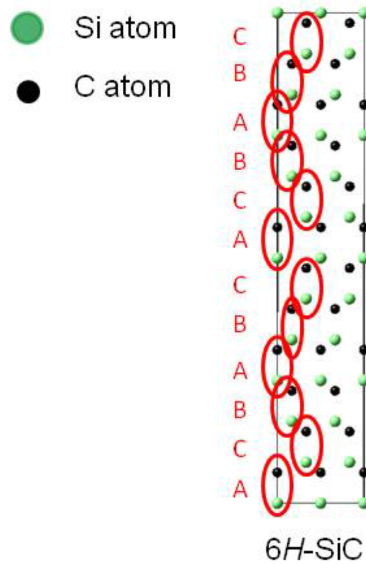

Figure 2.4: Stacking sequence of double layers of 6*H*- SiC polytype obtained from the database of Materials Design Software, MedeA.

The common donor impurities for SiC are nitrogen, phosphorus, aluminum, or boron, of which the impurity atoms may substitute on either the carbon or the silicon sub-lattice. Phosphorus and nitrogen occupy the carbon sites [4, 5] whereas aluminum substitutes only on the silicon sub-lattice [6] and boron atoms occupy either on the silicon or carbon sub-lattice. As shown in the Figure 2.5, polytypes 4*H*-SiC and 6*H*-SiC have inequivalent sites where k and h represents cubic and hexagonal symmetry lattice sites. The closeness of the impurity atom is the same on either site, but the only difference is the second-nearest neighbors. For mixed structure polytypes, the k and h sites split into inequivalent sites as quasi-cubic (k_1, k_2, k_3...), and hexagonal (h_1, h_2, h_3 …), if their third or next higher neighbors are different. For 6*H*-SiC, there are two different cubic sites k_1 and k_2 and one hexagonal site h. The Figure 2.5 shows the schematic diagram of the stacking sequence of most familiar polytypes along the c-axis in $[11\bar{2}0]$ plane.

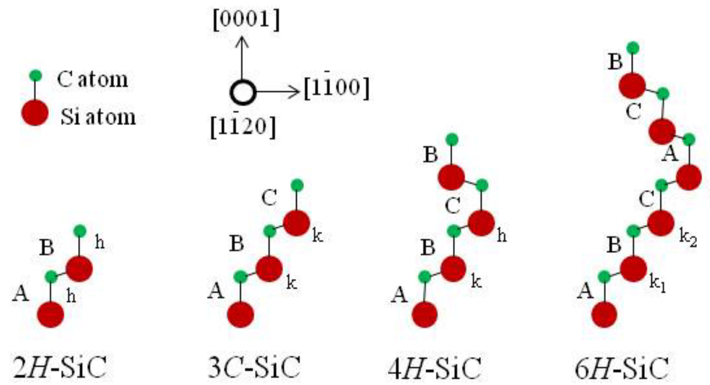

Figure 2.5: Stacking sequence of most common polytypes of SiC. The cubic and hexagonal crystal symmetry points are represented by h and k respectively.

For example, when a carbon atom in 4*H*-SiC is substituted by impurity atom, such as nitrogen, it can either occupy a k site or an h site, and will have two binding energies for this type of donor. Similarly in 6*H*-SiC it will have three binding energies and for 3*C*-SiC it will have only one binding energy.

2.1.1 Mechanical and Thermal Properties

SiC is considered to be the one of the hardest material among the ceramics. The common polytypes has Mohs hardness about the value of 9 [7]. Acoustic velocity is the other important mechanical property of SiC. 3*C*-SiC has acoustic velocity of 12,600 m/s where 4*H*-SiC and 6*H*-SiC have 13,730 and 13,100 m/s respectively [8]. The physical properties of the devices change with the increase of temperature, which degrades the performance of the material. Thus, the material with high thermal conductivity is advantageous for high power and high frequency device applications. As mentioned in the Table 2.2 below, the thermal conductivity of SiC is higher than Si and GaAs, which makes SiC the most useful wide band gap semiconductor for high-power/frequency applications. The relatively low atomic weights of Si and C and the high

elastic modulus of SiC, which causes harmonic lattice vibrations, gives rise to high thermal conductivity.

2.1.2 Optical and Electronic Properties

The structure, cubic or hexagonal, in SiC crystals depends on the nearest-neighbor atom arrangement. 2*H*-SiC has only h sites which makes the polytype 100% hexagonal and 3*C*-SiC has only k sites which makes it 0% hexagonal (100% cubic). The other common polytypes 4*H*- and 6*H*-SiC are 50% and 33% hexagonal, respectively. The band gap increases monotonically from E_g = 2.412 eV for 3*C*-SiC, which has 0% hexagonality, to E_g = 3.33 eV for 2*H*-SiC, which has 100% hexagonality. Because of this large band gap of SiC, it can be used for very high temperature environments, which limits the applications of Si-based devices.

Table 2.2: Properties of three commonly used polytypes of SiC along with most used semiconductor Si at 300 K for comparison [9, 10].

Property	3*C*-SiC	4*H*-SiC	6*H*-SiC	Si
Melting Point (K)	3100	3100	3100	1690
Lattice Parameter (a, c in A^o)	a=4.36 c=4.36	a=3.08 c=10.05	a=3.08 c=15.12	5.43
Bandgap (eV)	2.42	3.23	3.02	1.11
Dielectric constant	9.7	9.7	9.7	11.8
Breakdown electric field (10^8 Vm^{-1})	>1.5	3.0	3.2	0.6
Thermal Conductivity (W m^{-1} K^{-1})	320	370	490	150
Electron mobility (10^{-4} m^{2}V^{-1}s^{-1})	750	800	60	1200
Hole mobility (10^{-4} m^{2}V^{-1}s^{-1})	40	115	90	420
Saturation drift velocity (10^5 ms^{-1})	2.5	2	2	1

From Table 2.2, it can be seen that the breakdown electric field strength of SiC polytypes is almost 5 times higher than that of Si or GaAs. This property of SiC makes it an excellent material for power device applications, which can be operated at much higher voltages than are possible with Si. The properties of the three common polytypes of SiC discussed above are shown in the Table 2.2 for comparison along with other commonly used semiconductor Si.

2.2 Defects in SiC

Studies of defect are one of the significant research fields in semiconductor physics. The defects are formed either due to deliberate introduction of defects into the materials, or due to different growth conditions when the semiconductors are made. In general, a defect is considered as a lack of crystal perfection. Point defects, linear defects, and planar defects are the basic classes of crystal defects. Vacancies, interstitial atoms, anti-site atoms, substitution impurity atoms, and interstitial impurity atoms are considered as point defects. For example, let us consider the binary semiconductor SiC, which is composed of Si and C atoms. The vacancy, $V_{Si,\,C}$ will be a missing atom of the atomic species Si or C respectively from its lattice site in the crystal structure. The interstitial $I_{Si,\,C}$ is an excess atom acquiring a position between lattice sites; whereas the anti-site, A_{Si}, occurs when the lattice site of a Si atom is occupied by C atom and A_C occurs when the lattice site of a C atom is occupied by Si atom. Vacancies and interstitials together are called a Frenkel pair [11]. Suppose, if X is an impurity atom in the lattice, a substitutional impurity atom $X_{Si,\,C}$ can be defined as an impurity atom, which replaces one of the atom species, either Si or C in the crystal lattice. An interstitial impurity I_X can be defined as an impurity atom occupying some other region in a lattice not occupied by Si and C atoms. The arrangement of atoms in irregular positions is called linear defects and dislocations are the common linear defects found in the semiconductors. Grain boundaries and stacking faults are the

two types of planar defects. The stacking faults and planar defects are one of the characteristic defects in SiC crystals. These faults are easily generated in Si-C double atomic planes because of the differences in the formation energies of individual polytypes is small.

The studies of defects in SiC are of great scientific and technological interest, those involving with ion implantation, electron and neutron irradiation. These defects created in semiconductors play an important role in altering the optical, electronic and magnetic properties of the materials. Transition metals such as Vanadium in 6*H*-SiC are doped in SiC to make it semi-insulating material [12, 13]. Dalibor et al. have studied the V-related defect centers in V^+ implanted in 3*C*-, 4*H*-, 6*H*-SiC polytypes by DLTS measurements. These defects centers were named as V_1, V_2 and V_3 defect centers. The investigation showed that these defects created are acceptor-like and the defect centers V_1 and V_2 occupy cubic and hexagonal lattice sites in 4*H*-SiC [14]. These defects generate deep levels to trap the carriers and form the high resistive region in SiC. These deep levels are subject of interest as they are important for designing electronic devices. Structural and optical properties of SiC have been studied by different groups [15 - 17].

Even though a great deal of progress has been made in the growth of SiC crystals to reduce the imperfections in the crystal, many properties of the defects created during ion implantation are not well understood. Point defects such as vacancies, interstitials and anti-sites are produced mainly by irradiation. These native point defects exist in different charge states due to the rise to energy levels in the fundamental gap [18, 19]. In the low energy implantation range of about 100 keV, the Frenkel pairs for both C and Si atoms are close to each other. Since the interstitials and vacancies are separated by only a few atomic distances, there is a great probability for the recombination of interstitials and vacancies, which result in a strong lowering of the total energy

of the entire structure. At energies implanted with 300 keV, carbon interstitials and carbon vacancies are spatially separated, whereas silicon atoms form close Frenkel pairs due to their higher mass [20]. The Frenkel pairs of silicon atoms are well separated when the implanted energies are in the range of 2 MeV [21]. As the vacancies and interstitials are well separated, the *determining quantity* for the recombination process is to overcome the *activation barrier* for the migration of the interstitials through the lattice before reaching the capture radius of the vacancy. Isolated vacancies are thermally stable at room temperature and far above, since they need higher activation energy for vacancy diffusion [22]. Son et al. have investigated the deep luminescent centers in electron irradiated 6*H*-SiC. The results show that these defect centers are thermally stable and suggested to be complexes which involve silicon vacancy [23]. Bratus et al. have studied the carbon vacancies in ion beam and electron irradiated 6*H*-SiC [24].

The defects created in the materials by irradiation of energetic particles can be characterized using different techniques such as RBS-C, Raman spectroscopy, PAS and transmission electron microscopy (TEM). All these techniques probe different aspects of the defects. For example, RBS-C is more sensitive to the interstitial type of defects, whereas PAS is sensitive to vacancy-type defects. The degree of disorder created in the materials, due to ion implantation can be quantified using Raman spectroscopy and as well as from RBS-C methods. More details about the RBS-C and Raman techniques will be discussed in Chapter 3.

2.3 Ion Implantation Induced Defect Engineering in SiC

Ion implantation is the primary technology used in the semiconductor industry to introduce controlled impurities into semiconductors to form different types of electronic devices and for various industrial applications. The technology of ion implantation uses ion accelerators to direct beams of ions into desired materials. These implanted ions create large amounts of damage

during their slowing down phase in the solid depending on the fluence and other parameters used such as ion mass and energy. Detailed discussion about the ion implantation technology is explained in the next chapter. Detailed applications of ion implantation technology can be found at the proceedings of some of the international conferences such as Ion Beam Analysis (IBA), Ion Beam Modification of Materials (IBMM), Conference on Application of Accelerators in Research and Industry (CAARI) and Conference on ion implantation technology etc.

SiC is already drawing attention for semiconductor devices due to its capability of working under extreme conditions. These devices rely on semiconductor materials whose properties depend upon defects and their complexes. Ion implantation is a key technology and is widely used to create defects in the semiconductor materials and induce defect engineering in SiC. The damages created from the implantation are the cause of many of the levels within the forbidden energy gap and play an important role in affecting the electrical properties of implanted layers. The ion implantation damage in wide band gap semiconductor such as in SiC could be either related to donor or acceptor damage. Selective doping of the most commonly used ions such as B, P, N or Al is done using ion implantation technology. SiC is considered not only as an important material for electronic devices, but is also making rapid progress towards applications in spintronic devices. These magnetic semiconductor devices use the property of both charge transport of n- or p-type and also the quantum property of electron, its spin state. The introduction of the magnetic ions into SiC can be easily done using ion implantation technology.

2.4 Potential Applications

SiC is gaining significant interest among all the wide bandgap semiconductors available due to its exceptional physical and chemical properties [25, 26]. The superior material qualities such as wide bandgap, high thermal conductivity, high field breakdown strength, and a high

saturation velocity makes SiC more attractive than any other semiconductors under extreme conditions such as at high temperature, high power, and high frequency environments. It has a number of potential applications in the fields of microstructures; high temperature, high power and high frequency electronics; optoelectronics, and radiation hard electronics. Hence SiC can potentially be considered as a replacement for Si.

The use of SiC was first started as a cutting material and for abrasive applications [27]. Blue LEDs were the first optical application of SiC [28]. Over time, the direct band gap of GaN overtook the LED production of the indirect band gap of SiC [28]. Even though SiC is not used for production of LEDs, it is still used in active optoelectronic applications such as substrates for GaN, which has a lattice mismatch of about 3% when grown on SiC. The semi-insulating SiC has shown great potential as a substrate material for SiC and III-nitride microwave technology. Potentially, the resistance to high radiation doses makes SiC the ideal technology for nuclear power applications. Si-based electronic devices cannot operate above 250 °C and SiC can replace it in those harsh environments. SiC is used for aeronautical applications as well as in fusion and fission high temperature nuclear reactors. Applications of SiC in high temperature power electronics includes aircrafts, automotive, space exploration, and deep oil wells where the temperatures can reach above 250 °C. The wide band gap semiconductor SiC is highly attractive for metal-oxide-semiconductor (MOS) technology applications due to its unique physical, chemical, and electronic properties as compared to the conventional Si-based MOS devices [29 - 33]. The unique combination of high thermal conductivity (3 times more than Si), high saturated electron velocity (2.5 times greater than Si), and high electric field breakdown strength (5 times greater than Si) makes SiC a very promising candidate for high power microwave devices. Some of the commercially available electronic devices made of SiC include Schottky diodes,

Thyristors, MOSFETs, and UV sensors. DMS have the properties of both magnetic materials and semiconductors. These are formed when the semiconductors are doped with magnetic ions such as V, Cr, Mn, Fe, Co, and Ni. DMS are gaining interest in potential applications such as in spintronic semiconductor devices. They are also gaining importance in building spintronic devices such as in modulators, spin field effect transistor (spin-FET), spin light emitting diode (spin-LED), magneto resistive random access memory (RAM), and spin valves [34]. Some of the DMS's that are extensively studied are ZnO, HfO_2, GaAs, and carbon-based materials including SiC [35 - 39]. It can be concluded that SiC is an excellent wide band gap semiconductor that has numerous applications in harsh environments such as high temperature, high frequency, and high power areas that are not possible using Si.

2.5 References

1. A. P. Mirgorodsky, M. B. Smirnov, E. Abdelmounim, T. Merle and P. E. Quintard, Phys. Rev. B **52** 3993 (1995).
2. L. S. Ramsdell, Am. Mineralogist **32** 64 (1947).
3. MedeA software, Materials Design, Inc., USA.
4. H. H. Woodbury, G.W. Ludwig, Phys. Rev. **124** 1083 (1961).
5. G. E. G. Hardeman, J. Phys. Chem. Solids **24** 1223 (1963).
6. Y. Tajima, W. D. Kingery, Commun. Am. Ceram. Soc. **65** 27 (1982).
7. G. R. Lemaitre, Astronomical Optics and Elasticity Theory, Springer Series, Berlin (2009).
8. G. L. Harris, Properties of Silicon Carbide, INSPEC Publication, United Kingdom (1995).

9. P. G. Neudeck, “SiC Technology” in the VLSI Handbook, W.K. Chen Ed., New York: CRC & IEEE Press, pp. 6-1 – 6-32 (2000).
10. Y. Goldberg, M. Levinshtein, and S. L. Rumyantsev, “Silicon Carbide,” in Properties of advanced semiconductor materials – GaN, AlN, InN, BN, SiC, SiGe, M. Levinshtein, S.L. Rumyantsev, and M.S. Shur Eds., New York: Wiley, 93-148 (2001).
11. W. J. Choyke, H. Matsunami, G. Pensl, Silicon Carbide: Recent Major Advances, Springer Series, New York, USA (2004).
12. T. Kimoto, T. Nakajima, H. Matsunami, T. Nakata, M. Inoue, Appl. Phys. Lett. **69** 1113 (1996).
13. H. M. Hobgood, R. C. Glass, G. Augustine, R. H. Hopkins, J. Jenny, M. Skowronksi, W. C. Mitchel, M. Roth, Appl. Phys. Lett. **66** 1364 (1995).
14. T. Dalibor, G. Pensl, H. Matsunami, T. Kimoto, W. J. Choyke, A. Schoner, N. Nordell, Phys. Stat. Sol. (a) **162** 199 (1997).
15. X. Wang, Y. Zhang, S. Liu, C. Wang, Z. Zhao, Nuc. Instr. and Meth. B **289** 47 (2012).
16. Y. Dou, H. Jin, M. Cao, X. Fang, Z. Hou, D. Li, S. Agathopoulos, J. Alloys and Comp. **509**(20) 6117 (2011).
17. G. Feng, X. Fang, J. Wang, Y. Zhou, R. Lu, J. Yuan, M. Cao, Phys. B: Cond. Matter **405**(12) 2625 (2010).
18. A. Zyweitz, J. Furthmuller, and F. Bechstedt, Phys. Rev. B **59** 15166 (1999).
19. L. Torpo, S. Poykko, and R. M. Nieminen, Phys. Rev. B **57** 6243 (1998).
20. E. Rauls, T. E. M. Staab, Z. Hajnal, Th. Frauenheim, Physica B **308-310** 645 (2001).
21. H. J. von Bardeleben, J. L. Cantin, L. Henry, M. F. Barthe, Phys. Rev. B **62** 10841 (2000).

22. J. Schneider, K. Maier, Phys. B: Cond. Matt. **185**(1-4) 199 (1993).

23. N. T. Son, E. Sorman, M. Singh, W. M. Chen, C. Hallin, O. Kordina, B. Monemar, J. L. Lindstrom, E. Janzen, Diamond and Related Mater. **6**(10) 1378 (1997).

24. V. Y. Bratus, T. T. Petrenko, H. J. von Bardeleben, E. V. Kalinina, A. Hallen, Appl. Sur. Sci. **184**(1-4) 229 (2001).

25. W. Wesch, Nucl. Instr. And Meth. B **116** 305 (1996).

26. M. A. Capano, R. J. Trew, MRS Bull. **22** (3) 19 (1997).

27. S. E. Saddow, A. K. Agarwal, Advances in Silicon Carbide Processing and Applications, Artec House, Inc., USA (2004).

28. Y. S. Park, SiC Materials and Devices, Semiconductors and Semimetals, Vol. 52, Academic Press, USA (1998).

29. M. Ruff, H. Mitlehner, and R. Helbig, IEEE. Trans. Electron Devices ED **41** 1040 (1994).

30. H. Morcoc, S. Strite, G. B. Gao, M. E. Lin, B. Sverdlov, and M. Burns, J. Appl. Phys. **76** 1363 (1994).

31. J. A. Cooper, Jr., Phys. Status Solidi A **162** 305 (1997).

32. M. R. Melloch, J. A. Cooper, Jr., MRS Bull. **22** 42 (1997).

33. H. Matsunami, Mater. Sci. Forum **389-393** 15 (2002).

34. S. A. Wolf, D. D. Awschalom, R. A. Buhrman, J. M. Daughton, S. von Molnar, M. L. Roukes, A. Y. Chtchelkanova, D. M. Treger, Science **294** 1488 (2001).

35. A. N. Andriotis, R. M. Sheetz, and M. Menon, J. Phys., Condens. Matter **22** 334210 (2010).

36. W. F. Koehl, B. B. Buckley, F. J. Heremans, G. Calusine, D. D. Awschalom, Nat. **479** 84 (2011).

37. H. Ohldag, T. Tyliszczak, R. Hohne, D. Spemann, P. Esquinazi, M. Ungureanu, T. Butz, Phys. Rev. Lett. **98** 187204 (2007).

38. Y. Liu, G. Wang, S. C. Wang, J. H. Yang, L. A. Chen, X. B. Qin, B. Song, B. Y. Wang, X. L. Chen, Phys. Rev. Lett. **106** 087205 (2011).

39. J. B. Yi, C. C. Lim, G. Z. Xing, H. M. Fan, L. H. Van, S. L. Huang, K. S. K.S. Yang, X. L. Huang, X. B. Qin, B. Y. Wang, T. Wu, L. Wang, H. T. Zhang, X. Y. Gao, T. Liu, A. T. S. Wee, Y. P. Feng, J. Ding, Phys. Rev. Lett. **104** 137201 (2010).

CHAPTER 3

THEORETICAL SIMULATIONS OF INTERACTION OF IONS IN MATERIALS AND EXPERIMENTAL CHARACTERIZATION TECHNIQUES

3.1 Introduction

The outline of the theoretical simulation methods and characterization techniques used in this research are provided in this chapter. The theoretical simulations necessary for C and Si implantations in 4*H*-SiC at low energy (60 keV) and N in 4*H*-SiC at high energy (1 MeV) were done by computer simulations using SRIM/TRIM – 2011. Ion implantation was performed using source of negative ions by cesium sputtering (SNICS-II), NEC at the Ion Beam Modification and Analysis Laboratory (IBMAL), UNT. Different characterization techniques, such as RBS-C and Raman spectroscopy, were performed to analyze the implanted samples. The magnetic measurements were carried out using SQUID. RBS-C reported in this thesis was carried out at EMSL, Pacific Northwest National Laboratory (PNNL), Richland, Washington, USA. Raman measurements were performed at Center for Advanced Research Technology (CART) at UNT. Superconducting quantum interference device (SQUID) measurements were performed at two different institutes. C implanted samples with fluences ranging from 1×10^{12} ions/cm^2 to 1×10^{16} ions/cm^2 were analyzed at the Industrial Research Limited, Lower Hutt, New Zealand. The implanted sample with fluence 5×10^{12} ions/cm^2 was analyzed at the University of Leipzig, Germany.

3.2 Ion Beam Facility at IBMAL

The IBMAL at UNT in the Department of Physics is equipped with four accelerators which are 9SDH-2 3.0 MV National Electrostatic Corporation (NEC) Pelletron® tandem

accelerator, 2.5 MV Van de Graaff (HVEC Type AK) accelerator, 200 kV Cockcroft-Walton accelerator, and a newly installed 9SH 3.0 MV single-ended Pelletron® (NEC). Schematic of the main laboratory at IBMAL is shown in Figure 3.1.

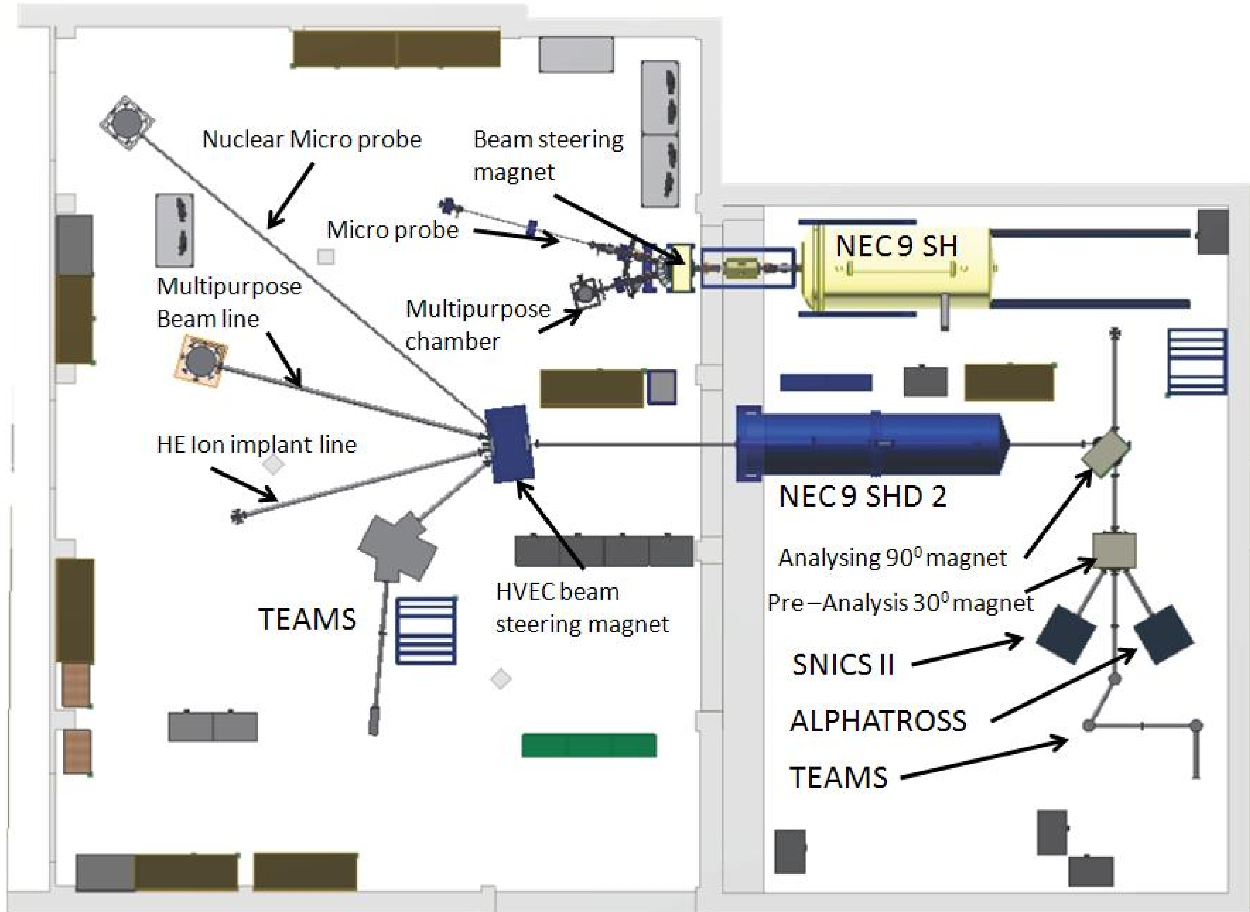

Figure 3.1: Schematics of the main laboratory at IBMAL, showing the 3 MV tandem (9SDH-2) and the 3 MV single ended (9SH) NEC Pelletron® accelerators and associated beam lines and experimental end stations.

The tandem accelerator is equipped with three ion sources: one radio frequency(RF)-He ion source (Alphatross) and two ion sources of Cs-sputter type, the SNICS II and a Cs-sputter source for trace-element accelerator based mass spectrometry. One of the beam lines of the tandem Pelletron® is used for high energy implants (in the low MeV range). The low energy implant line which is just after the 90° magnet before the accelerator is used for shallow implants

up to the range of 10-80 keV. A third implant beam line is currently being developed on the 3.0 MV Pelletron®, which can also be used for implantation.

The Model AK Van de Graaff is a single ended accelerator in which the ion source is located inside the terminal. In the Van de Graaff accelerator, the charge is transferred by a moving belt to an equipotential surface which builds up in voltage. Millions of volts can be obtained by using suitable choice of electrical components and insulating gas such as SF_6. In the Pelletron®, the belt is replaced by a charging chain of alternating insulating and conducting components, a more uniform transport of charge, and better stability can be obtained from this accelerator. The Pelletron® charging system and the charging chain are shown in the Figure 3.2.

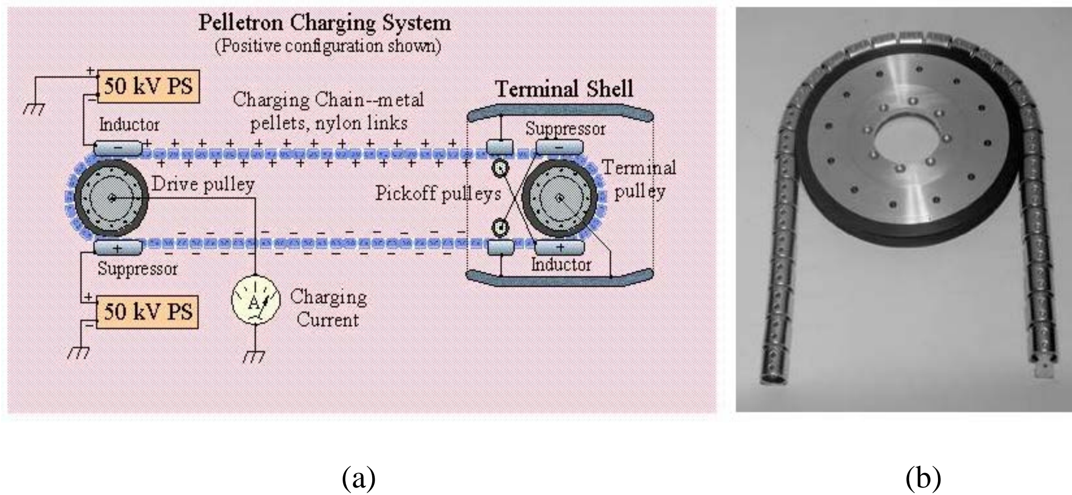

(a) (b)

Figure 3.2: Schematics of (a) Pelletron® charging system. (b) The Pelletron® chain which consists of alternating insulating and conducting components. Adopted with permission from Dr. Greg Norton, National Electrostatics Corporation.

The negative ions from the SNICS ion source are accelerated from ground to the positive charged terminal. These ions are stripped of their negative charge and accelerated through a second acceleration tube to ground, giving an energy of (n+1) eV; where n is the positive charge state after stripping and V is the terminal voltage.

For low energy ion implantation, C and Si in 4*H*-SiC was done on one of the beam lines associated with the SNICS ion source. The high energy implantation (N in 4*H*-SiC) was done using the AK Van de Graaff accelerator. The main components of the low energy ion implantation beam line consist of ion source, 30° mass analyzer magnet, scanner and target chamber and are shown in Figure 3.3.

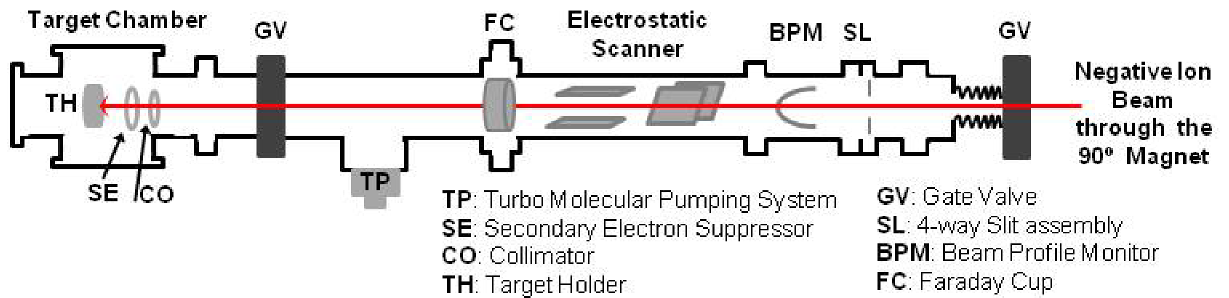

Figure 3.3: Schematics of the low energy ion implantation facility associated with the 9SDH-2 tandem accelerator.

The SNICS sputter ion source is used to generate negative ions of any element that have a substantial electron affinity. The sputter source can be used for most of the available ion species excluding noble gases which are not produced in negative charge states. The information about the list of the ions that can be implanted and their respective currents can be found from the NEC SNICS owner manual and the negative ion cookbook [1]. The negative ion cookbook is an another important book where the information about which material can be used to make the cathode for a given ion, the historical ion current, and mass spectrum of the sputtered material can be found. Currents more than 50 μA can be extracted from the SNICS ion source, depending on the type of cathode used.

The principle of operation of SNICS source uses ionized cesium (Cs) ions and the process of sputtering and charge exchange to produce negative ions. Schematic of SNICS is shown in the Figure 3.4. Cs vapors come from the Cs oven, which is heated up to 160 °C in a

closed area between the cooled cathode and the ionizer assembly. About 22 A of current is sent through the ionizer and is used to produce Cs^+ ions. In this process of heating, Cs vapors coat the cooled cathode area and some of the Cs is ionized by the hot surface. This ionized Cs is accelerated towards the cathode which is applied at about 5 kV.

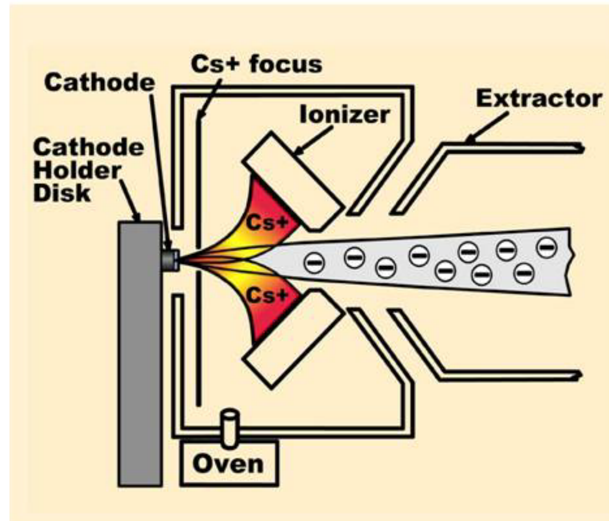

Figure 3.4: Schematics of the source of negative ions by cesium sputtering (SNICS-II) associated with the 9SDH-2 tandem accelerator. Adopted with permission from Dr. Greg Norton, National Electrostatics Corporation.

These energetic Cs ions strike and sputter particles from the surface of the cathode. Some materials will preferentially sputter negative ions and some other materials positive or neutral ions and become negatively charged as they pass through the Cs coating on the cathode surface producing negative ions. These negative ions are sputtered from the cathode and are extracted by an 11 kV voltage and later accelerated by a 0 - 80 kV potential of a pre-acceleration stage prior to injection into the acceleration. Once the ions are extracted from the ion source it passes through the 30° magnet, where the ions are steered and get separated to the desired isotope needed for implantation. The magnet current can be controlled using the power supply either in local mode or using the computer (remote mode). In order to achieve the uniform

exposure of ions over the target, a high voltage electrostatic X-Y scanner is used to scan the ions, which can be controlled using the scanner power supply. Current integration is performed directly from the target. The implant fluence D (ions/cm^2) can be calculated using the following equation:

$$D = \frac{I \times t}{A} \times \frac{1}{q \times c} \qquad \text{Equation 3-1}$$

where I is current in amperes, t is time in seconds, A is area in cm^2, q is the charge state of the ion, and c is the charge of the electron which is 1.6×10^{-19} coulombs.

Integration of the charge on the target is done using a current integrator. Before performing the implantation, the current integrator was calibrated using a standard current source. Secondary electron effects are reduced by placing a small ring in front of the target and biasing it negative by a few hundred volts. Another isolated circular ring was placed before the suppressor so that the ion beam does not strike the negatively biased grid.

3.3 Ion Implantation

Ion implantation is a major technology used for device fabrication in semiconductor industry. Selective doping of impurities into any materials can be easily done using this technology. During implantation, energy from the ions is transferred to the target by electronic and nuclear interactions through a series of collisions before finally coming to a rest within the target. At low energy the radiation damage [2] is caused mostly by the nuclear collisions, which can transfer sufficient energy to target atoms to move them off lattice sites. The range of the ion can be determined from both nuclear and electronic energy-loss mechanisms. In order to produce damage, the energy transferred from ion to the target atom should exceed the displacement energy of the target atom. Let us consider the energy transferred to a target atom is E_1 and the displacement energy of the target atom is E_d. Collisions in which E_1 is greater than E_d will

displace the atom from its lattice site creating the damage within the crystal. The displaced recoiling target atom interacts with other target atoms in the crystal and produces more displacements causing a second generation of recoiling target atoms. In the end, it comes to rest through another series of nuclear and electronic stopping collisions. The generated secondary recoiled atoms create more damages to the crystal and thus this process is called a cascade process, or a series of damage events within the crystal. This damage depends on various factors such as mass of the incident ion and its energy, the mass of the target atom, and the temperature of the target. These collision cascades can be referred to as the damage cluster within the crystal.

Lattice defects are created when energetic ions are implanted into the materials. The parameters such as atomic number and mass of the incident ion, the incident energy of the ion, the temperature at which the ions are introduced into the target materials and the implanted fluence greatly influence the defect profile and the defects created in the materials. Thus various implantation conditions are important to control the defect processes. The energetic incident ions slow down as they lose energy in a series of nuclear collision with the atoms in the target material causing damage to the lattice structure. At lower fluences, the ion may have distinct individual tracks, but as the fluence increases in the volume of the target material, the damaged regions will begin to overlap thus leading to the amorphization of the material.

3.4 Simulation of Ion Irradiation Parameters using SRIM/TRIM-2011

3.4.1 Introduction

SRIM/TRIM is the most commonly used computer simulated program which calculates stopping powers, range, and straggling distribution for any ion at any given energy in any elemental target or compound as well as other features of the transport of ions in matter. This program is based on the Monte Carlo simulation method and was developed by James F. Ziegler and Jochen P. Biersack [3]. More details about this program are discussed in Appendix section.

3.4.2 Theoretical Calculations of Irradiation Parameters of C Implanted in 4*H*-SiC using SRIM/TRIM-2011

TRIM simulations were performed for low energy 60 keV of C or Si ions in 4*H*-SiC. Figure 3.5 shows the computer simulation of 60 keV carbon ions in 4*H*-SiC. The displacement energies of 20 eV and 35 eV were used for C and Si respectively for the theoretical simulations [4]. The ion path and the displaced Si and C atoms and the surrounding collision cascades created are shown in the Figure 3.5. An ion, when injected into the target with such high energy, will leave the disorder along the track it takes. The radius of the damaged area around the path depends upon the nature of collision that particle suffers.

Primary knock-on ions produce secondary knock-on and in turn produces many knock-ons so long as sufficient energy is imparted in each collision. The energy available for each ion will be reduced with each subsequent collision until all the ions come to rest within the target. The implanted ion travels in a random path as shown in Figure 3.5 as it penetrates the target losing energy by electronic and nuclear collisions.

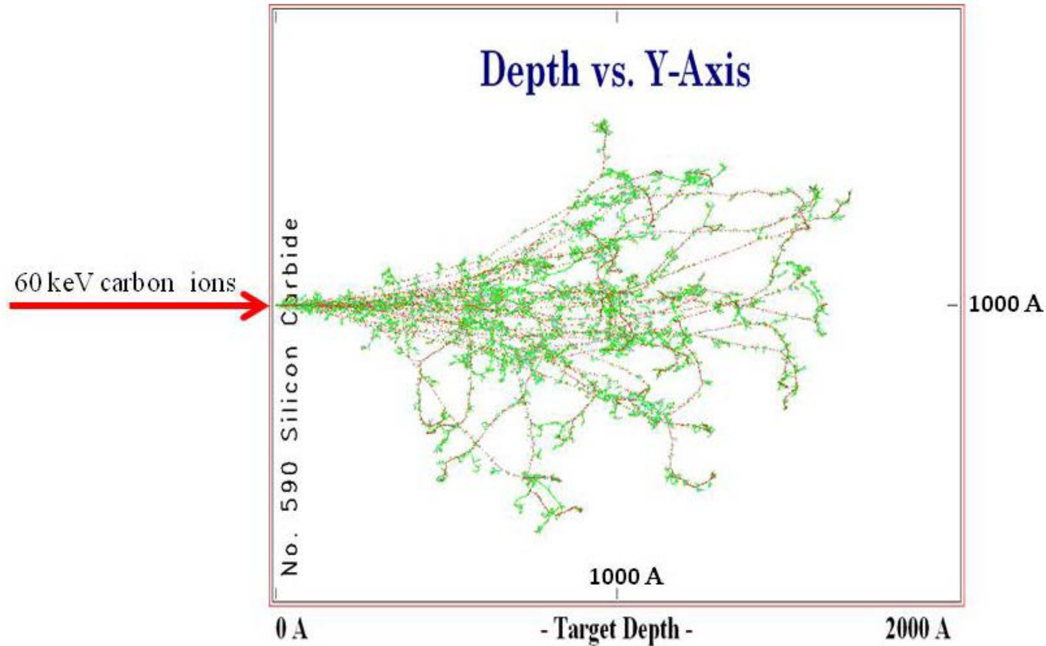

Figure 3.5: SRIM/TRIM simulation of 60 keV carbon ions in 4*H*-SiC showing the collision cascade within the target.

The range, R, can be defined as the average total path length along the depth of the sample which is composed of both vertical and lateral motions. The projected range, R_p, is defined as the average depth of the implanted ions. The distribution of the implanted ions at that depth can be approximated to a Gaussian with a standard deviation or energy straggling, ΔR_p. Figure 3.6 shows the ion distribution obtained from the statistics of 99999 ion histories. For C implantation in 4*H*-SiC at a low energy 60 keV, the projected range is found to be 116.6 nm with straggling of 32.2 nm in the depth axis. From SRIM-2011, the values for electronic and nuclear stopping power are found to be 41.29 eV/Å and 8.49 eV/Å respectively.

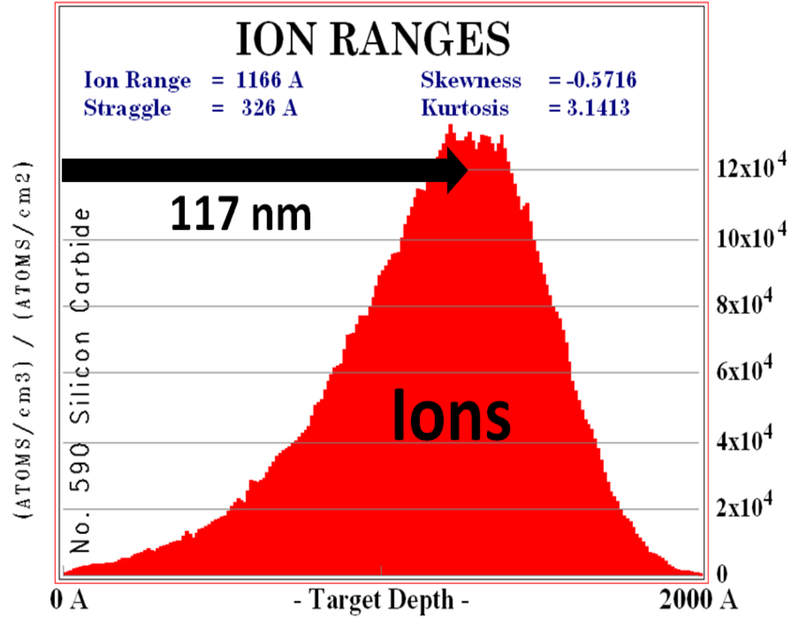

Figure 3.6: TRIM simulation of C ion implantation in 4*H*-SiC at the energy of 60 keV.

In the Figure 3.6, the X axis denotes the depth in Å and Y axis represents the units of (atoms.cm^{-3})/(atoms.cm^{-2}) which is atomic density normalized by fluence. The dopant concentration can be found from this ion-range distribution plot. This can be calculated by multiplying the implanted fluence with the maximum value at the damage peak. After the calculations, the dopant concentration for the C implanted fluences of 1.85×10^{14}, 3.5×10^{14}, 7×10^{14}, and 1×10^{15} ions/cm^2 are found to be 2.45×10^{19}, 4.55×10^{19}, 9.1×10^{19}, and 1.3×10^{20} atoms/cm^3 respectively.

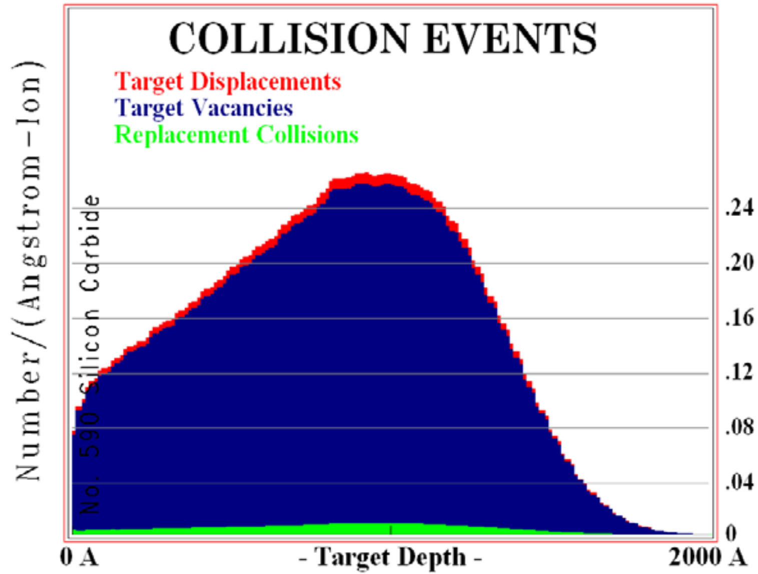

Figure 3.7: TRIM plot of collision events which includes target displacements, vacancies and replacement collisions.

The Monte Carlo TRIM simulation of collision events of C implantation in 4*H*-SiC is shown in the Figure 3.7. When ions are incident into the target, they constantly lose energy to the sea of electrons. These ions collide with the target atoms and displace the atoms creating vacancies. Displacement energy can be defined as the energy required for a target atom to leave its site and be pushed far enough away such that it will not return to its empty site. In this collision process, the recoiling target atom may have adequate energy to start a collision cascade where the other target atoms are collided and in turn may recoil into other atoms. This collision cascade is divided into displacement collisions, vacancy production, replacement collisions, and interstitial atoms. The total displacements collisions are the sum of the vacancies and replacement collisions and are shown in the Figure 3.7. When a recoil atom stops and is not a replacement atom, then it becomes interstitial. There can be a flow of vacancies and interstitials into the target material which can lead to the formation of extended defects such as dislocation loops.

At the peak of the damage plot, vacancy creation reaches maximum of about 0.27 vacancies per carbon ion. This value, when multiplied by the fluence used, gives the vacancy density. For example, for a fluence of 1×10^{15} ions/cm^2 when multiplied by 0.27 vacancies/(Å – Ion) gives the vacancy density of 2.7×10^{22} vacancies/cm^3. The displacement per atom (dpa) is defined as the fraction of atoms which have been displaced from lattice site by the incoming ions and is used to quantify the level of damage produced by the ion beam. The vacancy density of 2.7×10^{22} vacancies/cm^3 when divided by the density of 4*H*-SiC (9.64×10^{22} atoms/cm^3) gives a dpa value of 0.284. Similarly for the fluences of 1.85×10^{14}, 3.5×10^{14}, and 7×10^{14} ions/cm^2; the dpa calculated resulted in 0.052, 0.099, and 0.198 respectively.

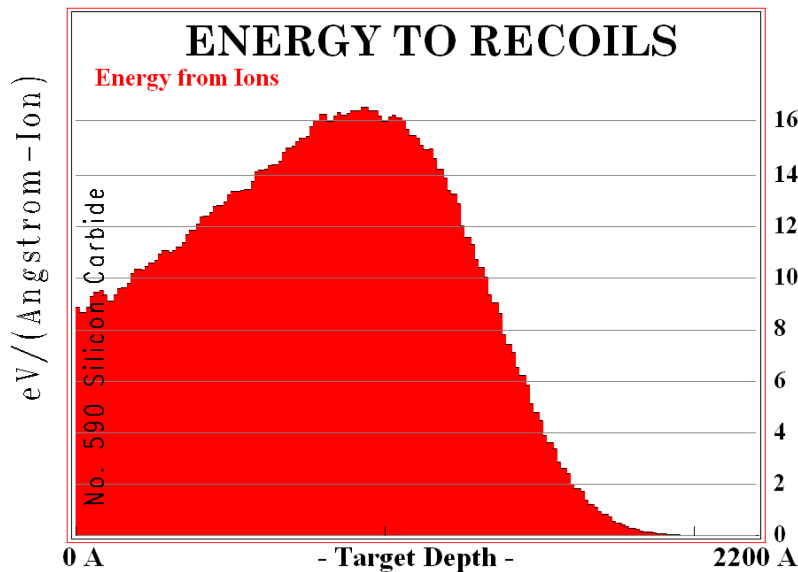

Figure 3.8: TRIM plot of energy to recoil atoms.

From the energy to recoil atoms plot which is shown in the Figure 3.8 the displacement damage or critical energy density is calculated. At the damage peak, the energy of the C ions reaches a maximum of 16 eV/(Å – Ion). This value when multiplied by the fluence used gives the critical energy density value. For example, for the fluence of 1×10^{15} ions/cm^2 when multiplied by 16 eV/(Å – Ion) gives the value of about 1.6×10^{24} eV/cm^3. Similarly for the

fluences of 1.85×10^{14}, 3.5×10^{14}, and 7×10^{14} ions/cm^2; the critical energy density calculated resulted in 2.96×10^{23} eV/cm^3, 5.6×10^{23} eV/cm^3, and 1.12×10^{24} eV/cm^3 respectively.

These critical energy density values are calculated based on the recommended threshold displacement energies of 20 eV and 35 eV for C and Si sub-lattices respectively [4]. Different values of displacement energies for both C and Si for calculating critical energy densities will lead to slightly different values for critical damage energy. Damage accumulation increases during ion implantation with increased fluence and proceeds to amorphization of the material. The different parameters calculated using these simulations for C ion implantation in 4*H*-SiC are tabulated in the Table 3.1.

Table 3.1: Calculated values for different parameters using SRIM/TRIM simulations for C ion implantation in 4*H*-SiC at low energy 60 keV.

C ion implantation in 4*H*-SiC at low energy 60 keV			
Fluence (ions/cm^2)	Vacancy concentration (vac./cm^3)	Displacement per atom (dpa)	Critical energy density (eV/cm^3)
1.85×10^{14}	5×10^{21}	0.052	2.96×10^{23}
3.5×10^{14}	9.45×10^{21}	0.099	5.6×10^{23}
7×10^{14}	1.89×10^{22}	0.198	1.12×10^{24}
1×10^{15}	2.7×10^{22}	0.28	1.6×10^{24}

3.4.3 Theoretical Calculations of Irradiation Parameters of Si Implanted in 4*H*-SiC using SRIM/TRIM-2011

TRIM-2011 simulations were performed for Si implantation into 4*H*-SiC at the energy of 60 keV. Figure 3.9(a) illustrates the distribution of ion tracks showing the cascade of collisions

between Si ions and SiC atoms. The implanted Si ions undergo collisions with some of the lattice atoms and displace them from lattice sites.

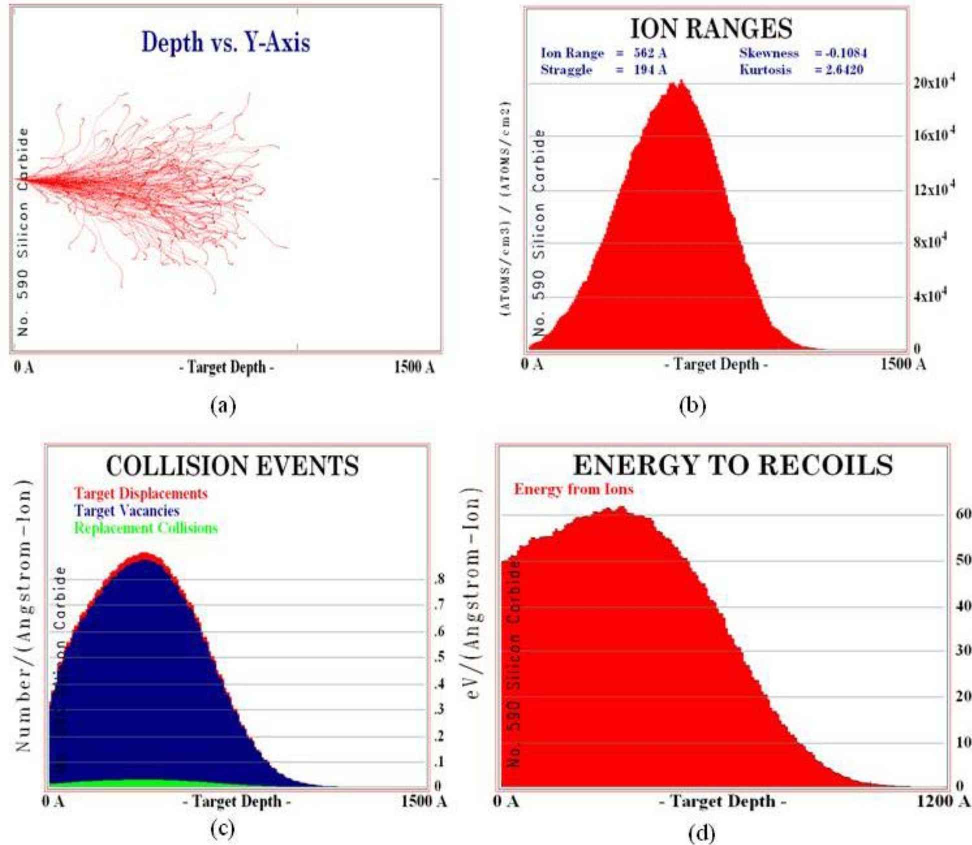

Figure 3.9 : TRIM plots for 60 keV Si implantation in 4*H*-SiC. (a) Monte-Carlo simulation of 60 keV silicon ions in 4*H*-SiC showing the collision cascade within the target. (b) Plot of the Si ion-distribution, (c) Collision plot which includes target displacements, vacancies and replacement collisions. (d) TRIM plot of energy to recoil atoms.

For Si implantation in 4*H*-SiC at the energy 60 keV, the projected range is found to be 56.2 nm with energy straggling of 19.4 nm. From SRIM -2011, the values for electronic and nuclear stopping power are found to be 45.7 eV/Å and 50.1 eV/Å respectively. The dopant concentration for the Si implanted fluences of 5.5×10^{13}, 1.1×10^{14}, 2.2×10^{14}, and 3.2×10^{14} ions/cm^2 is calculated to be 1.1×10^{19}, 2.2×10^{19}, 4.4×10^{19}, and 6.4×10^{19} atoms/cm^3, respectively.

From Figure 3.9(c), vacancy creation reaches a maximum of about 0.9 vacancies per carbon ion at the peak of the damage plot. This value when multiplied by the fluence gives the vacancy density created in the sample. For example, for a fluence of 5.5×10^{13} ions/cm^2 when multiplied by 0.9 vacancies/(Å – Ion) gives the vacancy density of 4.95×10^{21} vacancies/cm^3. As defined earlier the dpa is the fraction of atoms which have been displaced from lattice site by the incoming ions and is used to quantify the level of damage produced by the ion beam. The vacancy density of 4.95×10^{21} vacancies/cm^3 when divided by density of SiC which is 9.64×10^{22} atoms/cm^3 gives a dpa value of 0.0513. Similarly for the fluences of 1.1×10^{14}, 2.2×10^{14} and 3.2×10^{14} ions/cm^2, the dpa calculated resulted in 0.1026, 0.205 and 0.298 respectively. The different parameters calculated using these simulations for Si ion implantation in 4*H*-SiC are tabulated in the Table 3.2.

Table 3.2: Calculated values for different parameters using SRIM/TRIM simulations for Si ion implantation in 4*H*-SiC at low energy 60 keV.

Si ion implantation in 4*H*-SiC at low energy 60 keV			
Fluence (ions/cm^2)	Vacancy concentration (vac./cm^3)	Displacement per atom (dpa)	Critical energy density (eV/cm^3)
5.5×10^{13}	4.95×10^{21}	0.0513	3.3×10^{23}
1.1×10^{14}	9.9×10^{21}	0.1026	6.6×10^{23}
2.2×10^{14}	1.98×10^{22}	0.205	1.32×10^{24}
3.2×10^{14}	2.88×10^{22}	0.298	1.92×10^{24}

3.5 Characterization Techniques

3.5.1 Rutherford Backscattering Spectroscopy

RBS analysis is a non-destructive analytical technique without the need for sample preparation and concentration standards. It is extensively used for near-surface to deep layers (few micrometers) analysis of solids. RBS technique is based on elastic collisions between the incident ions (usually H or He) and the target materials, and involves measuring the backscattered ions from the target materials. This information can be used to determine elemental composition ratio and depth profiling of individual elements. The other applications of RBS include analysis of thin film thickness, uniformity, and impurity content. The crystalline quality of the materials can be determined by orienting the incident ions through the various crystal axes (RBS-channeling). The analyzed depth is about 2 µm in Si for incident 2 MeV He ions and about 20 µm for incident 2 MeV protons. The RBS-C technique is a powerful technique to determine the location and concentration of the implanted ions in the host substrate lattice [5].

3.5.1.1 Kinematic Factor K and Scattering Cross section σ

Consider a particle of mass M_1, moving with constant velocity collides elastically with a stationary particle of mass M_2. In this process, the energy will be transferred from the moving particle to the stationary particle. By applying the principles of conservation of energy and momentum, the simple elastic collision of two masses M_1 and M_2 can be solved. In backscattering analysis, M_1 is the mass of the projectile atom in the analyzing beam and M_2 is the mass of the atom of the target to be studied. The schematic representation of the backscattering analysis is shown in the Figure 3.10. Before collision, the kinetic energy of the projectile atom of mass M_1 is $E_0 = (½) \times M_1 v_0^2$ and the energy of target atom of mass M_2 is zero since it is at rest. After the collision, the energies of the projectile and target atoms are $E_1 = (½) \times$

$M_1v_1^2$ and $E_2 = (½) \times M_2v_2^2$ where v_1 and v_2 are the velocities of projectile and target atoms respectively after collision. The scattering geometries are shown in the Figure 3.10, where α is the incident angle, θ is the scattering angle, and φ is the recoil angle.

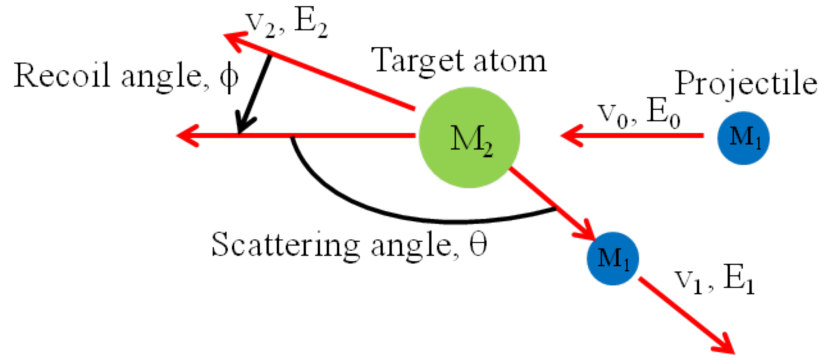

Figure 3.10: Scattering representation of an elastic collision between a projectile of mass M_1, velocity v, and energy E_0 and a target mass M_2 which is initially at rest. After the collision, the projectile and the target mass have velocities and energies v_1, E_1 and v_2, E_2 respectively. The angles θ and Φ are positive as shown. All quantities refer to a laboratory frame of reference.

Now, according to conservation of energy and momentum the following equations can be solved:

$$\frac{1}{2}M_1v_0^2 = \frac{1}{2}M_1v_1^2 + \frac{1}{2}M_2v_2^2 \quad \text{Equation 3-2}$$

$$M_1v_0 = M_1v_1 \cos\theta + M_2v_2 \cos\varphi \quad \text{Equation 3-3}$$

$$0 = M_1v_1 \sin\theta - M_2v_2 \sin\varphi \quad \text{Equation 3-4}$$

Solving the above equation gives:

$$\frac{v_1}{v_0} = \frac{[\pm(M_2^2 - M_1^2 \sin^2\theta)^{\frac{1}{2}} + M_1 \cos\theta]}{M_1 + M_2} \quad \text{Equation 3-5}$$

where the plus sign holds for $M_1 \leq M_2$. The kinematic factor K can be defined as the ratio of the projectile energy after the elastic collision, to that before the collision, and can be written as:

$$K_{M_2} = \left[\frac{(M_2^2 - M_1^2 \sin^2\theta)^{\frac{1}{2}} + M_1 \cos\theta}{M_1 + M_2} \right]^2 \quad \text{Equation 3-6}$$

All quantities here refer to the laboratory system of coordinates. As in the above equation the kinematic factor depends on the mass ratio of M_1 and M_2 and the scattering angle θ.

When the beam is incident on the target, only a small fraction of incident ions scatter backwards from the target material and are detected. The relative number of backscattered particles from a target atom into a solid angle for a given number of incident particles is related to the differential scattering cross section. In the laboratory frame of reference the differential scattering cross section can be written as:

$$\frac{d\sigma}{d\Omega} = \frac{Z_1 Z_2 e^2}{4E} \frac{4}{\sin^4\theta} \frac{\{[1-((\frac{M_1}{M_2}) \sin\theta)^2]^{\frac{1}{2}} + M_1 \cos\theta\}^2}{[1-((\frac{M_1}{M_2}) \sin\theta)^2]^{\frac{1}{2}}} \quad \text{Equation 3-7}$$

Here, dσ/dΩ is the differential scattering cross section and dΩ is the solid angle subtended by the detector. The sensitivity increases with increasing Z_1 and Z_2 and decreases with E.

3.5.1.2 Stopping Power and Energy Loss

When an energetic particle penetrates into the target material, it constantly loses energy due to electronic and nuclear collisions. This energy loss, ΔE per unit length Δx, depends on the type of the projectile, density and composition of the target, and the velocity of the projectile. This energy loss, dE/dx, of a fast moving energetic ion is determined by screened Coulomb interactions with the target atom electrons and protons in the nucleus. The energy loss rate can be expressed as the sum of nuclear and electronic collisions. In electronic collisions, the moving ion loses energy by ejecting or exciting atomic electrons. Significant angular deflection of the trajectory of the ion and large discrete energy losses are caused by nuclear collisions. This collision displaces atoms from their lattice sites and creates lattice disorder. While electronic

collisions cause much smaller energy losses and negligible deflection of the trajectory of the ion thus causing negligible lattice disorder. The energy transferred by the ion to the target nuclei is called nuclear stopping and the energy transferred by the ion to the target electrons is called electronic stopping. The energy lost by the moving particle due to elastic collisions-per-unit length traveled in the target materials is called nuclear stopping. The electron stopping is due to slowing down of the ions because of the inelastic collisions between the incident ions and the bound electrons in the target materials. The mechanism of energy loss is very important for depth profiling of individual elements in the target material. The stopping cross section, S, is defined as S = (dE/dx)/N where N is the atomic density of the target material. The energy loss, dE/dx, in any target materials can be calculated using the computer program SRIM.

3.5.1.3 RBS-C

In the channeling mode, the rows or planes of atoms in the lattice are aligned parallel to the incident beam, which reduces their interactions with the target atoms. The ions penetrate deeper in the crystal, making small angle collisions with the atomic rows. The yield of the backscattered ions is much reduced compared to random scattering (Rutherford scattering), since the channeled particles cannot get close enough to the atoms of the solid, which avoids large angle Rutherford scattering as illustrated in Figure 3.11.

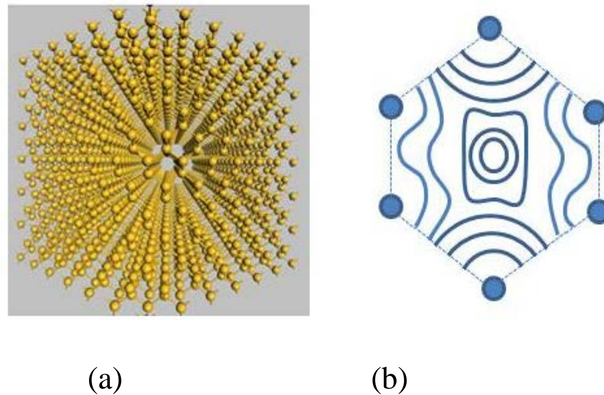

(a) (b)

Figure 3.11: (a) Lattice atoms viewed along the axial direction (b) equipotential surfaces [5].

The minimum yield of ions, i.e. reduction of scattering from atoms on regular lattice sites, makes the channeling mode an excellent tool for analyzing the crystal structure. The lattice site, lattice disorder, and defect density can be easily analyzed by the use of channeling. The major applications of channeling are to find the composition and thickness of amorphous layers, location of impurity atoms in the lattice sites, interstitials and the amount and depth distribution of lattice disorder. The critical angle, Ψ_c, can be defined as the maximum incident angle for which the incident ions can be steered by the atomic rows. For channeling the critical angle is referred to as half angle, $\Psi_{1/2}$, which is defined to relate to the angular width of the channel. The critical angle can be mathematically represented as:

$$\Psi 1/2 = \alpha e \left[\frac{Z_1 Z_2}{Ed}\right]^{\frac{1}{2}} \quad \text{Equation 3-8}$$

where Z_1 and Z_2 are atomic numbers of ion and target atoms, E is energy of the beam, d is the atomic spacing, e is the charge of an electron, and α depends on lattice vibration with values ranging from 0.8 to 1.2 [6]. Compared to axial channeling, planar channeling gives higher minimum yields and is characterized by narrower critical angles [7 - 9].

There is always a possibility that in a perfect crystal as the channeled particles penetrate deep into the material they can be scattered into non-channeled trajectories leading to de-channeling. As mentioned earlier the combination of small angle multiple scattering events and scattering by thermally displaced atoms increases with the depth of the number of dechanneled particles [10 - 12]. The amount of dechanneling depends on the crystallographic direction and can be minimized by channeling along major crystallographic axes. Defects in the crystal also cause dechanneling. Compared to the scattering by electrons in the perfect crystal, the scattering by the displaced atoms is much stronger. The channeled particles are scattered relative to the critical angle causing small deflections in the perfect crystal whereas the scattering from the

displaced atoms is beyond the critical angle which causes greater deflections. The dechanneling is characterized by different correlations between the displacements of the lattice atoms. Different kinds of defects have different dechanneling mechanisms. The trajectories of the incident particles depend on the type of defect and can be calculated using the dechanneling factor σ_D for each type of defect. The product of the defect dechanneling factor σ_D and defect density n_D gives the probability of dechanneling per unit depth $\frac{dP_D}{dz}$ and can be mathematically written as:

$$\frac{dP_D}{dz} = \sigma_D n_D(z) \quad \text{Equation 3-9}$$

The dechanneling rate is greatly influenced by crystal imperfections. The behavior of the ion energy with respect to the channeling yield can be used to identify the defect types in the lattice. The rate of dechanneling is proportional to $E^{-1/2}$, $E^{1/2}$ and E^0 for point defects, dislocations and stacking faults respectively [13 - 15].

In Chapter 4, detailed discussions are provided for how to extract the experimental values for the kinematic factor, differential scattering cross-section, channel number to energy conversion, energy loss, and depth analysis.

3.5.2 Raman Spectroscopy

Raman spectroscopy is a well-established optical characterization technique used for investigation of crystallinity and homogeneity of materials along with study of electronic properties. It is a sensitive, contactless, fast, and non-destructive method used to identify materials, crystalline quality, and stress among the nanometer-sized materials. The applications are vast and are widely used in the semiconductor field as well as in the pharmaceutical, forensic science, and in archaeological fields.

The Raman effect is a light scattering phenomenon, which was first reported by an Indian scientist, Sir Chandrasekhara Venkata Raman, in 1928 [16]. When a light (photon) is incident on a material, it can be reflected, transmitted, absorbed, or scattered. This scattered light can be either elastic or inelastic. In the case of elastic scattered photons, the wavelength of the scattered photons is same as the wavelength of the incident photons; i.e. the scattered photons have the same frequency (energy) as the incident photons. This elastic scattering of photons is known as Rayleigh scattering. However Raman found that a very small fraction of light photons, one in 10^7, are inelastically scattered, where the wavelength of the scattered photon changes (either increases or decreases) with respect to the incident photon wavelength. This inelastic scattering is termed as Raman scattering.

Virtual state
v_o
Vibrational states
v_o
n
m
$v_o - v_m$
n
m
$v_o + v_m$

(a) Rayleigh Scattering (b) Stokes Scattering (c) Anti-Stokes Scattering

(a) (b) (c)

Figure 3.12: Schematically representation of (a) Rayleigh scattering (b) Stokes scattering and (c) anti-Stokes scattering.

The change in vibrational, rotational, or electronic energy of a molecule can be linked to Raman scattering. Raman scattering can be divided as Stokes or anti-Stokes scattering and can be explained by the energy diagram as shown in the Figure 3.12. In Figure 3.12 m and n

corresponds to the ground and higher vibrational energy levels, respectively. At room temperature most of the molecules are present in the lowest energy vibrational level.

When light is incident on these molecules, the ground vibrational state (m) excites to the virtual state and comes back to the higher vibrational state (n) with the absorption of energy by the molecule. That means that the emitted photon has less energy and a longer wavelength than the initial photon. This scattering is termed as Stokes scattering, where the scattered frequency is less than the incident frequency and is given as $\nu_0 - \nu_m$ where ν_m is the vibrational frequency of the molecule. However, some of the molecules might exist in the higher vibrational level due to thermal energy. Scattering from these states to the ground vibrational level (m) involves transfer of energy to the scattering photon. Meaning the emitted photon has more energy and shorter wavelength than the initial photon. This scattering is known as anti-Stokes scattering where the scattered frequency is more than the incident frequency and is given by $\nu_0 + \nu_m$ [17]. In the Raman spectrum, the X-axis is denoted by wave numbers or Raman shift. Wave number is the reciprocal of wavelength which has the units of cm^{-1}. The Raman shift (cm^{-1}) is calculated using the equation:

$$\Delta v(cm^{-1}) = \frac{1}{\lambda_{incident}} - \frac{1}{\lambda_{scattered}}$$ Equation 3-10

where $\lambda_{incident}$ and $\lambda_{scattered}$ are the wavelengths (in cm) of incident laser beam and scattered beam. Thus, the Raman shift is the difference between the excitation wavelength and the Raman scattered wavelength. The Y-axis is measured in intensities of Rayleigh or Raman scattered light, which is proportional to the number of molecules illuminated. Since at thermal equilibrium the molecules in the ground vibrational energy level exceeds the molecules in higher vibrational energy level, the intensity of Stokes scattering will always be higher than anti-Stokes scattering.

But in general, the Raman spectrum consists of only Stokes scattering unless it is mentioned as anti-Stokes scattering.

The Raman effect can be explained by the classical theory and using the quantum theory the selection rules and intensities of the peaks can be predicted.

3.5.2.1 Classical Theory

A dipole moment is induced in a molecule when an electric field is applied to it. This happens due to the displacement of electrons and nuclei in the molecule and the molecule is said to be polarized. The polarizability of the molecule can be found using the formula:

$$\mu = \alpha E \qquad \text{Equation 3-11}$$

where μ is the magnitude of the induced dipole moment, E is the strength of the electric field, and α is the polarizability of the molecule. Thus, a polarized molecule when subjected to radiation of frequency ν, each molecule experiences an electric field according to the equation:

$$E = E_0 \sin 2\pi\nu t \qquad \text{Equation 3-12}$$

Now:

$$\mu = \alpha E = \alpha E_0 \sin 2\pi\nu t \qquad \text{Equation 3-13}$$

Rayleigh's scattering can be explained from the above equation where the scattered photon energy (frequency) is same as incident photon energy (frequency).

Now consider the case where the molecules have vibration and rotational motions. The polarizability of the molecules changes periodically when it undergoes vibratory motion. The change in polarizability due to this vibration of frequency ν_a can be written as:

$$\alpha = \alpha_0 + \beta \sin 2\pi\nu_a t \qquad \text{Equation 3-14}$$

where α_0 is the equilibrium polarizability and β is the rate of changes of polarizability with the vibration:

$$\mu = \alpha E = (\alpha_0 + \sin 2\pi \upsilon t) E_0 \sin 2\pi \upsilon t \qquad \text{Equation 3-15}$$

$$\mu = \alpha_0 E_0 \sin 2\pi\upsilon t + \frac{1}{2}\beta E_0 \left[\cos 2\pi\,(\nu - \upsilon_a)t - \cos 2\pi\,(\upsilon + \nu_a)t\right] \qquad \text{Equation 3-16}$$

In this equation, the first term corresponds to the Rayleigh's scattering where there is no change of frequency from incident to scattering photon. The second term corresponds to the Raman scattering where the frequency change is (ν-ν_a) and (ν+ν_a). The scattering frequency (ν-ν_a) is termed as Stokes frequency, where the frequency of the scattered photon decreases or wavelength increases and the scattering frequency (ν+ν_a) is known as anti-Stokes frequency, where the frequency of the scattered photon increases or wavelength decreases.

Now consider the effect of rotation of the molecule on polarizability. In a diatomic molecule, as it rotates, the orientation of the molecule changes accordingly to the electric field of rotation. The polarization of the molecule changes with time if the molecule is not optically isotropic and can be expressed as:

$$\alpha = \alpha_0 + \beta' \sin 2\pi\,(2\nu_r t) \qquad \text{Equation 3-17}$$

where ν_r is the frequency of the rotation and the term $2\nu_r$ is used instead of ν_r because the rotation of the molecule through π angle will make the polarization of the diatomic molecule the same as initially:

$$\mu = \alpha_0 E_0 \sin 2\pi\upsilon t + \frac{1}{2}\beta' E_0 \left[\cos 2\pi\,(\nu - 2\nu_r)t - \cos 2\pi\,(\upsilon + 2\nu_r)t\right] \qquad \text{Equation 3-18}$$

The first term in this equation corresponds to the, Rayleigh's scattering and the latter two terms corresponds to Raman scattering.

3.5.2.2 Quantum Theory

According to the quantum theory, the Raman effect can be characterized as the collisions between the incident light and the molecules of the material. Consider a molecule of mass m in the state of energy E_0 and moving with velocity v that collides with a light photon hν. After

collision, the molecule undergoes a change in energy state as well as in its velocity. Assume that the new energy state is E_1 and the velocity v' after collision. From the conservation of energy principle it can be written as:

$$E_0 + \frac{1}{2} m v^2 + h\nu = E_1 + \frac{1}{2} m v'^2 + h\nu' \qquad \text{Equation 3-19}$$

Considering the change in velocity of the molecule negligible the equation becomes:

$$E_0 + h\nu = E_1 + h\nu' \qquad \text{Equation 3-20}$$

$$\nu' = \nu + \frac{E_0 - E1}{h} \qquad \text{Equation 3-21}$$

$$\nu' = \nu + \frac{\Delta\nu}{h} \qquad \text{Equation 3-22}$$

If $E_0 = E_1$, the frequency difference Δν is zero implying that ν'= ν. This corresponds to Rayleigh scattering where the frequency of the scattered photon is same as the incident photon. In the case of $E_0 > E_1$, ν'>ν, which means the frequency of the scattered photon is more than the incident photon. This corresponds to anti-Stokes scattering. When $E_0 < E_1$, the frequency becomes ν'<ν, i.e. the scattered photon has less frequency than the incident photon frequency, which is Stokes scattering.

3.5.2.3 Experimental Set Up

All the Raman measurements were performed at The Center for Advanced and Research Technology (CART) at UNT. The CART research center has a number of very sophisticated characterization and processing instruments. The Raman system used here in the present research work was a Thermo Electron Almega XR Raman spectrometer. The system includes Omnic for Almega-7 analytical software, which includes fluorescence correction with all excitation frequencies. Atlus software is used for spectroscopic mapping and chemical profiling.

The main components required for the Raman system are (a) excitation source, (b) optical design, (c) monochromators, and (d) detectors. The system used was equipped with two laser

sources. One of them is a near infrared laser, which has a wavelength of 780 nm with 100-3100 cm^{-1} Raman shift and the other was a visible green laser of wavelength 532 nm with 100-4000 cm^{-1} Raman shift. The maximum laser power that can be used is 25 mW. The system is also equipped with automated Rayleigh rejection filter switching. For the measurements, the green laser was used as an excitation source with 25 % laser power (6 mW).

Figure 3.13: Thermo Electron Almega XR Raman Spectrometer at CART, UNT.

Optical design is the important characteristic feature of the Raman system. The system is equipped with high and low resolution gratings for each wavelength and different sizes of aperture slits. The aperture used was 25 μm slit and the beam spot size of the laser was 1.1 μm. The system is also equipped with different working distance objectives (10×, 20×, 50×, 100×). 50× objective was used for the Raman measurements.

The charged-coupled device (CCD) is reliable and commercially available for spectroscopic applications. The CCD is fabricated using metal-oxide semiconductor technology. The charge is stored in the capacitor gate. Readout occurs after sequential charge transfer and the transfer of photoelectrons is controlled by clocking of voltages on the electrodes. Conversion of

charge into a measurable voltage is subsequently digitized and transferred to the control computer. The system is equipped with high sensitivity thermo electrically cooled silicon CCD array detector. Picture of the Raman spectrometer is shown in Figure 3.13.

The Raman experimental set-up that was used for the present research and the results obtained for C, Si implanted samples in 4*H*-SiC are discussed in Chapter 4. The Raman scattering results of N implanted 4*H*-SiC samples are discussed in Chapter 5.

3.5.3 Superconducting Quantum Interference Device

SQUID is a very sensitive magnetometer which is used to measure extremely small magnetic fields. It can also measure magnetic field gradient, voltage and magnetic susceptibility. SQUID uses the properties of Josephson effect and flux quantization in a superconducting loop. Josephson effect [18] involves the coherent tunneling of Cooper pairs of electrons in Josephson junction with no applied voltage. Josephson junctions are formed by two superconductors separated by thin insulating layers. The Cooper pairs tunneling through the barrier have a super current and is given by $I = I_0 \sin \delta$ where I_0 is the critical current and δ is the difference of phase of effective wave functions across the barrier. For currents greater than the critical value, a voltage is developed across the junction. The magnetic flux enclosed by a superconducting loop is quantized in units of the flux quantum, $\Phi_0 = \hbar/(2e)$ where $\hbar$ is the Planck's constant and e is the electron charge and the value of Φ_0 is 2.07×10^{-15} Weber.

In a SQUID superconducting loop, the loop contains either one RF-SQUID or two DC-SQUID Josephson junctions. These junctions are also termed as weak links. RF-SQUID has single Josephson junction in the path of the superconducting loop. The superconducting loop is inductively coupled to the inductor of an LC-resonant circuit. This circuit is excited with a

current with frequency ranging between MHz and GHz. When a magnetic flux is applied to this loop, the voltage oscillates with a period Φ_0.

In DC-SQUID the junctions are in parallel and operate using the interference of the currents from each junction and can detect minute magnetic fields in the material and are shown in Figure 3.14. SQUID measures the changes in magnetic field related with one flux quantum. When a constant bias current is maintained in the SQUID, the measured voltage oscillates with the changes in phase at the two junctions, which depend upon the change in the magnetic flux.

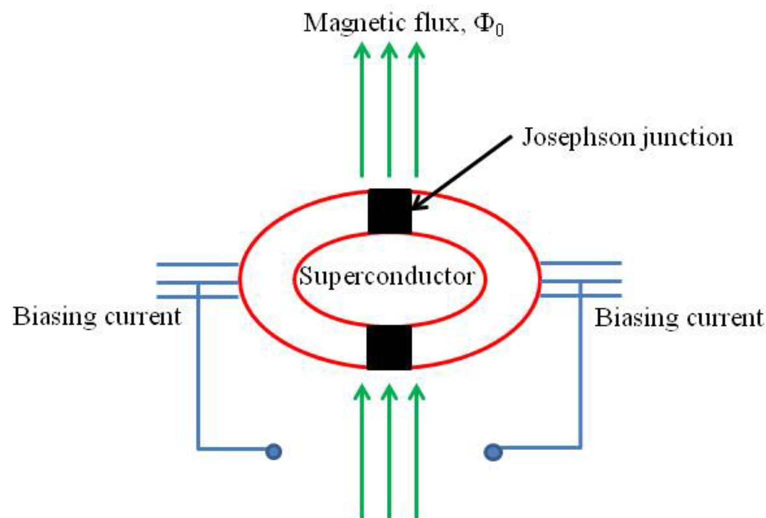

Figure 3.14: DC-SQUID with two Josephson junctions placed in the magnetic field.

Figure 3.15 shows the schematic representation of DC-SQUID. Assume a constant current known as bias current is passing through the SQUID. This bias current will split equally, half on each side when the SQUID is symmetrical and the Josephson junctions are identical. The flow of the super current continues as long as the total current flowing through it does not exceed the critical current of the Josephson junctions. A voltage is developed across the SQUID due to this super current. This critical current can be measured by increasing the bias current from zero until a voltage appears in the loop. Both the Josephson junctions develop the voltage at the same time when the applied magnetic field is zero in the symmetrical superconducting loop. Hence the

critical current of the SQUID is twice the critical current of one of the Josephson junctions in the loop.

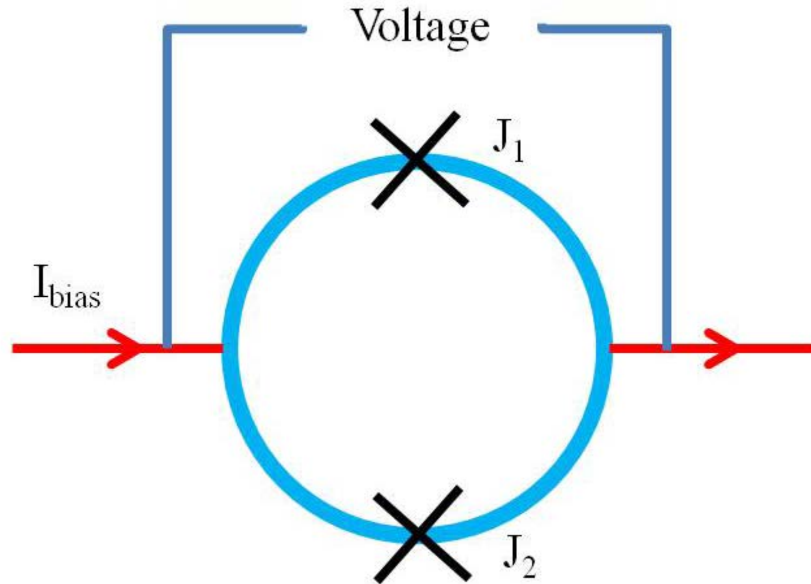

Figure 3.15: A schematic representation of DC-SQUID with two Josephson junctions, J_1 and J_2.

When a magnetic field is applied to the loop, the superconducting opposes the magnetic field by generating a screening current, I_s which flows around the loop. A magnetic field is created due to this screening current. This created magnetic field is opposite to the applied magnetic field thus cancelling out the net flux in the loop. The screening current increases in the loop as the applied magnetic field increases. When the applied magnetic flux is an integral multiple of the flux quantum, the screening current is zero whereas the critical current is maximized in the superconducting loop. The screening current is large and the critical current becomes minimum when the applied magnetic flux is an integral multiple of the flux quantum plus one half. Thus the SQUID voltage is periodic in the applied magnetic flux.

So when the magnetic flux through the loop is an integral multiple of the flux such as 0, Φ_0, $2\Phi_0$, $3\Phi_0$ and so on both the Josephson junctions have the same phase difference which results in constructive interference. Similarly opposite phase difference which results in

destructive interference is introduced between these junctions when the magnetic flux through the loop is $\Phi_0/2$, $3\Phi_0/2$, $5\Phi_0/2$ and so on. By measuring the voltage drop across the junction as the function of total current through the device, the critical current can be evaluated. Small magnetic moments can be measured as the critical current is sensitive to the magnetic flux through the superconducting loop.

3.6 References

1. R. Middleton, A Negative Ion Cookbook, University of Pennsylvania, Philadelphia (1989).
2. J. Lindhard, M. Scharff, and H. Schiott, “Range concepts and heavy ion ranges,” Kgl. Danske Vid. Selskab. Mat.-Fys. Medd. 33 (1963).
3. J. F. Ziegler, J. P. Biersack, U. Littmark, The Stopping and Range of Ions in Solids, Pergamon, Press, New York (1985).
4. R. Devanathan, W. J. Weber, and F. Gao, J. Appl. Phys. **90** 2303 (2001).
5. L. C. Feldman, J. W. Mayer, Fundamental of Surface and Thin Film Analysis, USA (1986).
6. W. Chu, J.W. Mayer, M.A. Nicolet, Backscattering spectrometry, Academic Press, New York (1978).
7. B. R. Appleton, and G. Foti, “Ion Beam Handbook for Material Analysis”, Academic Press, New York (1977).
8. D. S. Gemmell, Rev. Mod. Phys. **46** 121 (1974).
9. D. V. Morgan, “Channeling”, Wiley, New York (1973).
10. G. Foti, F. Grasso, R. Quattrochi, and E. Rimini, Phys. Rev. B **3** 2169 (1971).

11. E. Bonderup, H. Esbensen, J. U. Andersen, and H. E. Schiott, Radiat. Effects **12** 261 (1972).

12. N. Matsunami, and L. M. Howe, Radiat. Effects **51** 111 (1980).

13. S. T. Picraux, E. Rimini, G. Foti, S. U. Campisano, Phys. Rev. B **18**(5) 2078 (1978).

14. L. C. Feldman, J. W. Mayer, S. T. Picraux, Materials Analysis by Ion Channeling, Academic Press, New York (1982).

15. G. Gotz, B. Gruska, Nuc. Instr. and Meth. B **194**(1-3) 199 (1982).

16. C. V. Raman, K. S. Krishnan, Nature **121** 501 (1928).

17. R. W. Wood, Nature **122** 349 (1928).

18. B. D. Josephson, Phys. Lett. **1** 251 (1962).

CHAPTER 4

CHARACTERIZATION OF DEFECTS IN LOW ENERGY (C, Si) ION IMPLANTED 4*H*-SiC

Controlled creation of defects in materials is an approach to modify the electronic properties in a way that results in new functionality. Silicon carbide is a promising candidate for defect-induced magnetism on which spintronic devices could be developed. The defects considered are of room temperature stable vacancy types, eliminating the need for magnetic impurities, which easily diffuse at room temperature. Impurity free vacancy type defects can be created by implanting the host with atoms of silicon or carbon. The implantation fluence determines the defect density, which is a critical parameter for defect induced magnetism. Therefore, we have studied the influence of low fluence silicon and carbon implantation on the creation of defects in SiC. The defects have been profiled using RBS-C and Raman spectroscopy measurements. In this chapter the experimental results and analysis of various characterization techniques are presented.

4.1 Introduction

SiC has already become an attractive wide bandgap semiconductor due to its unique physical and electronic properties and is widely used in high temperature, high frequency, high power and radiation resistant applications [1 - 3]. SiC has been used as an alternative to Si in harsh environments such as in the oil industry, nuclear power systems, aeronautical, and space applications [4 - 7]. Some of the commercially available electronic devices made of SiC include Schottky diodes, Thyristors, MOSFETs, and UV sensors. SiC is also known for its polytypism and so far over 250 different polytypes have been found with bandgaps ranging from 2.42 eV to 3.26 eV. Among them 3*C*-SiC, 4*H*-SiC and 6*H*-SiC are the most common polytypes used for

research purposes. Among these polytypes 4*H*-SiC is gaining importance due to its easy availability as a commercial wafer with high thermal conductivity, high thermal mobility and a large bandgap of 3.26 eV at room temperature [8].

For carbon films, it is found that proton irradiation leads to magnetic order [9]. A recent study indicated the possibility of defect induced magnetic moments also for SiC, which is highly interesting for technological applications. Based on first-principle calculations for SiC monolayer, it was shown that the presence of silicon vacancies (V_{Si}) may induce local magnetic moments whereas for carbon vacancies (V_C) no spin polarization occurs [10, 11]. The possibility of defect induced magnetism in SiC opens the door for research towards possible transition-metal-free SiC semiconductors. In this respect, ion implantation is an excellent technique to create defects in a controlled fashion. When Si or C ions are implanted into the SiC host material, no impurities are introduced, but vacancies can be created. The local magnetic moments, which can be induced due to the defects, depend on the average distance between vacancies [12, 13], which is dependent on the density of the created defects. The defect concentration in turn is dependent on the fluence. *Hence, the crucial point is the average distance between vacancies or the defect concentration, which is dependent upon the fluence.* The main aim of this research is to determine the predicted narrow window in the implantation fluence, which will result in local ferromagnetism in 4*H*-SiC.

Although ion implantation of different ions in SiC has been extensively studied [14 - 21], including 550 keV energy C^+ [22] and Si^+ ions [23] at different substrate temperatures, not much is known about low energies and low fluences of C and Si implanted into 4*H*-SiC. Recently Li et al. have reported defect induced ferromagnetism in 4*H*-SiC using 140 keV Ne ions [21] with fluences of 5×10^{14} cm^{-2} and 1×10^{16} cm^{-2}. RBS-C is a suitable technique to study defects since the

defects induced by implantation enhance the dechanneling compared to the virgin crystal. Raman spectroscopy is a contactless, non-destructive, and sensitive technique. It is a common tool to study defects in SiC polytypes [24 - 28]. RBS-C and Raman can be used as complementary techniques to monitor disorder buildup in the ion implanted samples in the following way. RBS-C measurement can be used to determine the damage in the transverse direction of the probing ion beam as a function of depth. Whereas the LO and TO phonon mode signals in Raman spectroscopy provide information on the integral damage in the longitudinal and transverse directions respectively in the sample. In the present study, we have investigated the influence of Si and C ion implantation on the production of defects and defect density in 4*H*-SiC. Low energy (60 keV) C or Si ions were implanted into 4*H*-SiC. Ion fluences between 10^{13} cm^{-2} and 10^{15} cm^{-2} were chosen to create different vacancy type defect densities, ranging from low to high densities. In order to investigate the defect induced magnetism, SQUID measurements were performed with samples implanted with 60 keV carbon ions at various fluencies.

4.2 Ion Implantation and RBS-C Experimental Procedure

Single crystal nitrogen-doped n-type, double side polished, research grade 4*H*-SiC wafer, with surface normal to [0 0 0 1], was obtained from CREE, Inc., USA (CREE product description: W4NRF0X-0200 with chemical and mechanical polished Silicon face). More details about the product description can be found at the wafer grower's website Cree.com. The wafer had a net doping density (N_D-N_A) of 9×10^{14} – $1\times10^{19}/cm^3$ (±25 % tolerance) in the Si face with a resistivity of 0.013-2.00 ohm-cm. The wafer was diced (by American Dicing Inc., USA) into several small samples of different sizes of 5 mm × 5 mm, 10 mm × 5 mm and 10 mm × 10 mm as shown in Figure 1. Different pieces of sizes 10 mm × 5 mm were used for both C and Si

implantations. The samples were implanted with 60 keV Si or C ions using the sputter ion source, SNICS – II [29] at the IBMAL at the UNT.

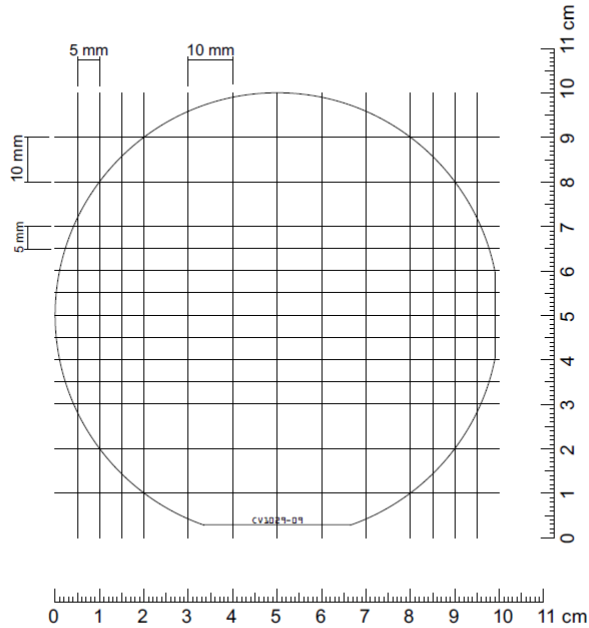

Figure 4.1: A 4” diameter n-type 4*H*-SiC wafer was diced to smaller pieces at American Dicing Inc., USA.

As discussed earlier in Chapter 3, from the simulations, the fluences of 1.85×10^{14}, 3.5×10^{14}, 7×10^{14}, and 1×10^{15} ions/cm^2 for C implantation were chosen. The fluences for Si implantation were chosen as 5.5×10^{13}, 1.1×10^{14}, 2.2×10^{14}, and 3.2×10^{14} ions/cm^2. These fluences corresponds to 0.0052, 0.098, 0.196, 0.28, and 0.051, 0.103, 0.205, 0.298 dpa for C and Si implantation, respectively.

The target was placed vertically behind a ring-shaped electrode which was negatively biased with 300 V in order to correctly integrate the current by suppressing the emission of secondary electrons from the sample during the ion implantation. One side of the sample was implanted uniformly over its area by electrostatically raster scanning the incident ion beam. The implantation was carried out at an angle of 7° off the surface normal to avoid channeling

conditions for the implanted ions. A low ion current areal density of ~0.2 μA/cm^2 was used to avoid any significant sample heating due to implantation.

4.2.1 Experimental Set Up for RBS-C Analysis

RBS-C measurements were performed using a 2 MeV He^+ ion beam at the Environmental Molecular Sciences Laboratory (EMSL) within the Pacific Northwest National Laboratory (PNNL). The facility consists of a NEC 9SDH-2 Pelletron® 3-MV electrostatic tandem accelerator. The detector was placed at a backscattering angle of 150°. The current on the target was kept below 40 nA. The beam was collimated to a spot size of about 1×1 mm^2. The samples were mounted on a six-axis goniometer in the vacuum chamber maintained at a pressure of 10^{-7} Torr. All the spectra were collected for charge integration of 10 μC and the current on the target was maintained about 25 nA. The target was positively biased to 300 V for suppression of secondary electrons.

4.2.2 Minimum Yield and Angular Scan

Initially the search for the channeling axis was done on the virgin part of the implanted sample. The sample was rotated from -1° to +1° at a scan step of 0.207°. Once the position for the minimum RBS yield was found, the sample is tilted from -1° to +1° at a scan step of 0.05°. After finding the positions (rotation and tilt) for minimum RBS yield, the aligned spectra for the virgin sample was taken at this point. Later, a random spectrum was taken on the implanted region with a rotation of the sample from -7° to +7°. The minimum yield χ_{min} and the full width half maximum (FWHM) of an angular scan, $2\psi_{1/2}$, in ion channeling experiments define how well the ion is channeled into the crystal. The minimum yield can be described as the ratio of the yield along the channel direction to the random direction. The yield as a function of the sample tilt angle with respect to the main axial or planar direction is defined as angular scan.

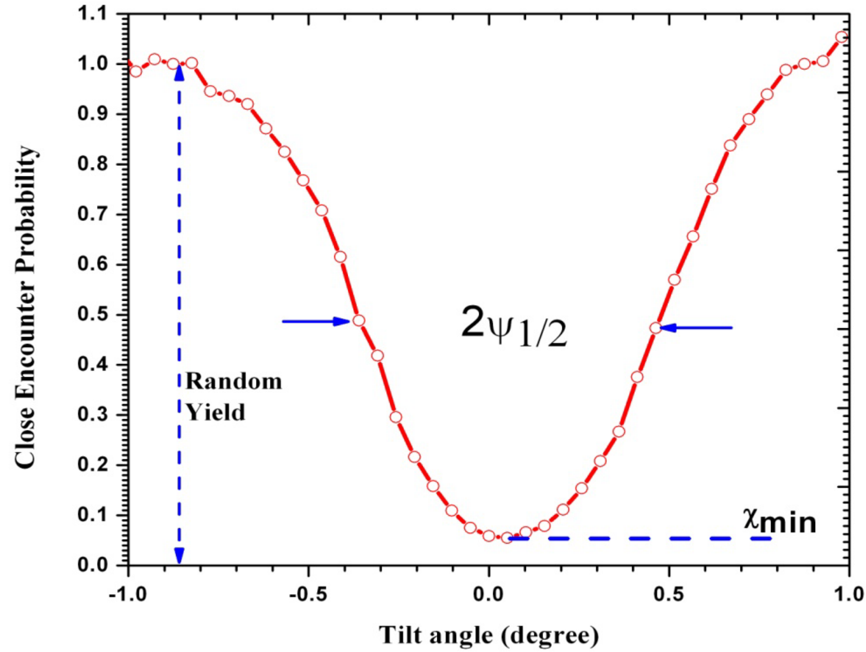

Figure 4.2: A typical RBS yield due to an angular scan across the channeling axis of 4*H*-SiC performed with 2 MeV He^+ beam.

The FWHM of angular scan is related to the critical angle for channeling and can be used to locate the lattice site determinations. The characteristic angle, Ψ_1, for axial channeling according to Lindhard's model [30] is:

$$\Psi_1 = [2Z_1Z_2e^2/Ed]^{1/2} \qquad \text{Equation 4-1}$$

Where Z_1 and Z_2 are the atomic numbers of ion incident and the target atom, e is the unit charge, E is the energy of the ion, and d is the lattice distance between the atoms.

An increase in the minimum yield χ_{min} and lower critical angle $\psi_{1/2}$ gives rise to an increase in ion dechanneling. The dechanneling rate is greatly influenced by crystal imperfections. The behavior of the ion energy with respect to channeling yield can be used to identify the defect types in the lattice. Figure 4.2 shows the angular scan of virgin 4*H*-SiC with a He^+ beam as the projectile. The channeling angular scan was measured at 2 MeV beam energy along (0 0 0 1) axis. The critical angle is found to be 0.4° from the angular scan and the results

extrapolated from the experimental data shows the critical angle for 1 MeV He ions incident on Si and Ge along the <100> directions to be 0.63 and 0.8, respectively [31].

4.2.3 Kinematic Factor and Differential Cross-Section

In RBS, the energy of the backscattered particles depends on the mass of the projectile, mass of the target atoms, scattering angle, incident energy of the ions and the depth of the collision in the material. The kinematic factor K can be derived using conservation of energy and momentum which is shown in Chapter 3. The equation for kinematic factor K is given by:

$$K_{M_2} = \left[\frac{(M_2^2 - M_1^2 \sin^2\theta)^{\frac{1}{2}} + M_1 \cos\theta}{M_1 + M_2} \right]^2 \qquad \text{Equation 4-2}$$

All quantities here refer to the laboratory system of coordinates as in the above equation the kinematic factor depends on the mass ratio of M_1 and M_2 and the scattering angle θ. Consider, for example, a 2 MeV He beam incident on SiC and scattered at 150°. Here M_1, which is the mass of He, is 4 and M_2, which is mass of either Si or C, which is 28 or 12, and the scattering angle θ is 150°. By substituting all these values in the above equation, the kinematic factors for Si and C can be calculated which gives the value of 0.58 for Si and 0.27 for C. These kinematic factors can be used to find the backscattered energies of the Si and C edges, which can be used for channel number to energy conversions. It gives the energies of ions scattered by surface atoms, $E_1 = K \times E_0$ where E_0 is the incident energy and K is the kinematic factor which depends on M_1, M_2 and θ.

When the beam is incident on the target, only a small fraction of incident ions scatter backwards from the target material and are detected. The relative number of backscattered particles from a target atom into a solid angle for a given number of incident particles is related to the differential scattering cross section. In the laboratory frame of reference the differential scattering cross section can be written as:

$$\frac{d\sigma}{d\Omega} = \frac{Z_1 Z_2 e^2}{4E} \frac{4}{sin^4\theta} \frac{\{[1-((\frac{M_1}{M_2}) \sin\theta)^2]^{\frac{1}{2}} + M_1 \cos\theta\}^2}{[1-((\frac{M_1}{M_2}) \sin\theta)^2]^{\frac{1}{2}}} \quad \text{Equation 4-3}$$

Where dσ/dΩ is the differential scattering cross section and dΩ is the solid angle subtended by the detector. Once the experimental conditions are known it is easy to calculate the differential scattering cross section using above equation.

4.2.4 Channel Number to Energy Conversion

In the RBS-C experiment, the backscattered ions from the target surface are collected by a surface barrier detector. The multichannel analyzer receives the very small voltage pulse generated by the detector and converts that signal into a digital signal. The analog-to-digital converter sorts the pulses by their amplitude and these pulses are sorted out into a specific number of bins. These bins represent the channels in the spectrum and are typically a power of 2. The common channel values used are 512, 1024, 2048, and/or 4096 depending on the resolution of the system and the energy range being studied. The energy spectrum is calibrated using standard sources and the backscattered yields in specific channels are correlated to backscattered energy and depth. At least two leading edges are needed for calibration and to linear fit the spectrum and convert the channel numbers to corresponding energies.

The kinematic factor, K, is defined as the ratio of the projectile energies after and before collision i.e. $E_1 = K \times E_0$ where E_1 is the energy after collision and E_0 is the incident energy. The energy of He^+ beam used was 2 MeV, which is E_0, and from the kinematic equation the kinematic factor K calculated for Si and C, were 0.58 and 0.27 respectively. With these known values the backscattered energy of Si and C can be calculated. The values were 1170 keV and 547 keV for Si and C respectively. The corresponding channel numbers and energy for Si and C were used to plot and is as shown in Figure 4.3.

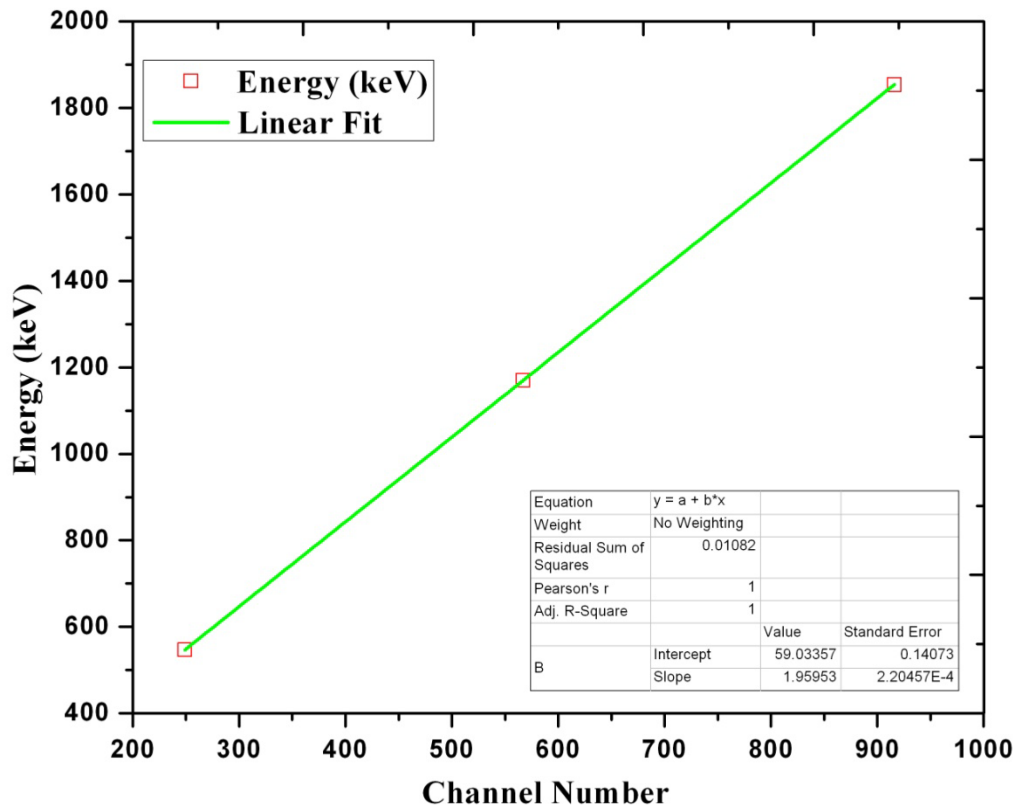

Figure 4.3 : Channel number to Energy conversion plot.

The linear correlation obtained from the plot gives us the value of E_c = mc+a, where E_c is the energy represented by the particular channel C, m is the slope of the line; i.e. Energy interval correspond to one channel (keV) and "a" is the intercept. The values obtained from the plot are m=1.959 keV/channel and a=59.17 keV respectively. So the detected energy is obtained from 1.96 keV times the channel number plus 59.17 keV. These values were used as the input in the SIMNRA plot to simulate the SiC with the other experimental conditions and the plot is as shown in Figure 4.4. From the SIMNRA plot, the values were found to be m=1.97 keV/channel with calibration offset of a=59. The values of "m" and "a" obtained by these two methods are compared and seem to be in good agreement with each other. The values obtained from the

linear correlation plot were used to convert the corresponding channel numbers to respective energies.

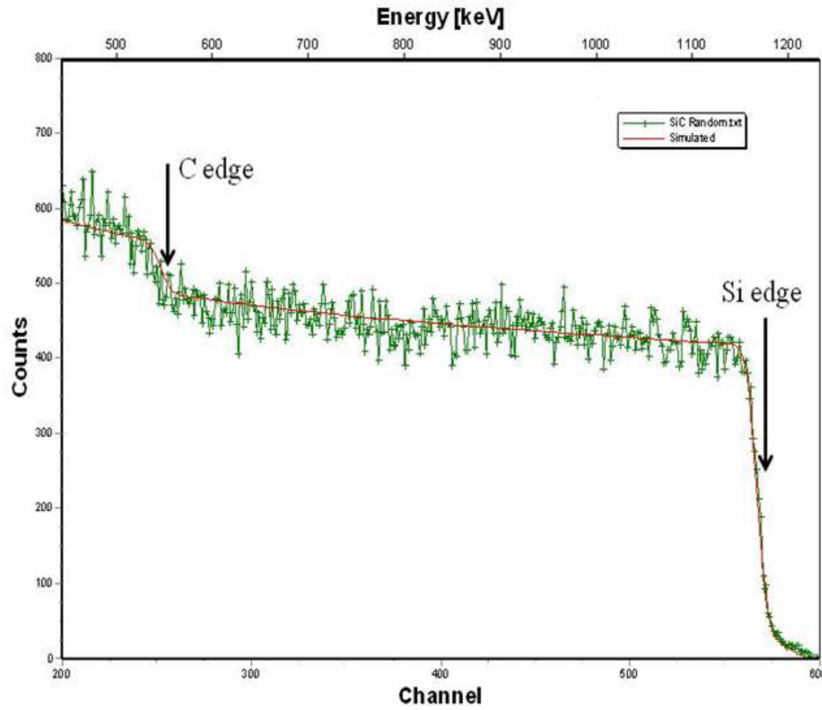

Figure 4.4 : SIMNRA of virgin SiC.

4.2.5 Energy Loss and Depth Analysis

Energy is lost continuously when a projectile penetrates a target and displaces the atoms in its path. Throughout its trajectory, this energy is lost to the electrons of the target atoms by ionization and by excitation; i.e. electronic collisions and also through nuclear collisions. The projectile trajectory changes to outward direction after the projectile encounters a hard collision with a target atom. Energy is also lost during its outward path until the particle emerges from the target. This energy loss phenomenon can be used to determine the depth to which the projectile has entered by measuring how much energy loss it has suffered in the inward and outward paths. This energy loss per unit path length depends upon the energy of the particle and also on the projectile and the target. The units of energy loss are normally expressed as eV/Å, keV/Å, or

MeV/μm. The total energy loss rate can be expressed as the sum of nuclear and electronic collisions. Nuclear collisions dominate at lower energies and electronic collisions dominate at higher energies. The stopping cross section, ε, can be defined as the energy loss dE/dx divided by the density of the target N; i.e. $\varepsilon = (1/N)\times(dE/dx)$.

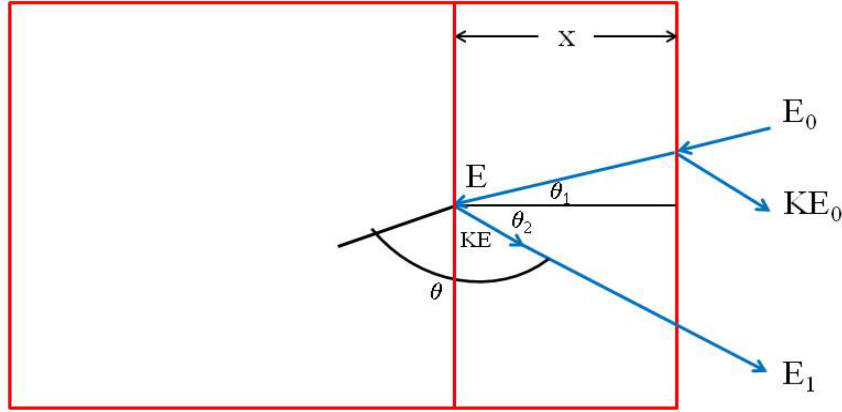

Figure 4.5 : Schematics of Energy Loss and Depth Conversions.

As shown in Figure 4.5 consider the energy of the incident particle is E_0 and the energy immediately before scattering is E at a depth x and the energy of the particle coming out of the surface is E_1. θ_1 and θ_2 are the angles between the sample normal and the direction of the incident beam and of the scattered particle and θ is given as $\theta = 180° - \theta_1 - \theta_2$.

The length x/cos θ_1 traveled by the beam inside the target can be related to the energy by:

$$\frac{x}{\cos\theta_1} = -\int_{E_0}^{E} dE \left(\frac{dE}{dx}\right)^{-1} \quad \text{Equation 4-4}$$

where the negative sign arises because E is smaller than E_0 and dE/dx is taken as a positive quantity. Similarly, for the outward path length x/cos θ_2, the energy is related by the equation below:

$$\frac{x}{\cos\theta_2} = -\int_{KE}^{E_1} dE \left(\frac{dE}{dx}\right)^{-1} \quad \text{Equation 4-5}$$

The above integrals can be simplified by assuming a constant value for dE/dx along the inward and the outward paths. With this assumption the integrals can be reduced to:

$$E = E_0 - \frac{x}{\cos\theta_1}\frac{dE}{dx_{in}} \qquad \text{Equation 4-6}$$

$$E_1 = KE - \frac{x}{\cos\theta_2}\frac{dE}{dx_{out}} \qquad \text{Equation 4-7}$$

The above two equations can be simplified by eliminating E:

$$KE_0 - E_1 = \left[\frac{K}{\cos\theta_1}\frac{dE}{dx_{in}} + \frac{1}{\cos\theta_2}\frac{dE}{dx_{out}}\right]x \qquad \text{Equation 4-8}$$

Here the KE_0 corresponds to the energy backscattered from the surface of the target. The above equation can be written as $\Delta E = [S]x$ where S is called the energy loss factor and in terms of stopping cross section the equation can be modified to $\Delta E = [\varepsilon]\times(Nx)$. Under this assumption there is a linear dependence of depth scale to energy.

4.2.5.1 Surface Approximation

Surface energy approximation can be made for thin films where the thickness, x, is small and the relative change in energy along the incident path is also small. With this approximation ΔE becomes:

$$\Delta E = \left[\frac{K}{\cos\theta_1}\frac{dE}{dx_{E_0}} + \frac{1}{\cos\theta_1}\frac{dE}{dx_{KE_0}}\right]x \qquad \text{Equation 4-9}$$

And S, the energy loss factor becomes:

$$[S] = \left[\frac{K}{\cos\theta_1}\frac{dE}{dx_{E_0}} + \frac{1}{\cos\theta_1}\frac{dE}{dx_{KE_0}}\right] \qquad \text{Equation 4-10}$$

Or ε_0 can be written as:

$$[\varepsilon_0] = [\frac{K}{\cos\theta_1}\varepsilon(E_0) + \frac{1}{\cos\theta_1}\varepsilon(KE_0) \qquad \text{Equation 4-11}$$

where the stopping cross sections $\varepsilon\times E_0$ and $\varepsilon\times(KE_0)$ can be evaluated at energies E_0 and KE_0 respectively.

4.2.5.2 Mean Energy Approximation

The surface energy approximation degrades when the path length of the beam inside the target becomes large. In this case, the mean energy approximation can be made by selecting a constant value of dE/dx or ε at an energy intermediate to that which the particle has at the end points of each track. Thus mean energy along the inward path, E_{in} becomes ½×($E+E_0$) and along the outward path, E_{out} becomes ½×(E_1+KE). The value of E can be obtained using energy loss ratio method or iterative method or analytical method. The energy loss ratio method is more accurate for analysis of surface thin films, where the surface energy approximation holds. Iterative methods can be used for accurate depth scale conversion from the energy scale [32]. An analytical approximation is calculated to determine the impurity concentration depth profiles from the measured Rutherford backscattering spectrum [33].

4.2.6 Analysis of Defect Concentration

The defect concentration can be quantitatively determined from RBS-C spectra using the two beam model. In this model the channeling spectrum from RBS-C analysis is the sum of de-channeled part of the spectrum, $\chi_R(x)$ and direct scattered part or channeled part of the spectrum (1- $\chi_R(x)$), where $\chi_R(x)$ is the dechanneled fraction of the beam. The direct scattering is from the channeled beam ions backscattered from the displaced atoms in the target. The dechanneled beam ions backscattered from the remaining thermally vibrating lattice atoms causes the de-channeled part of the spectrum. The dechanneling of the incident ions can be due to electronic scattering, the small angle nuclear scattering with the atoms of the perfect crystal, and the small angle scattering with the displaced atoms. The yield $\chi_D(x)$ with disorder can be written as:

$$\chi_D(x) = \chi_R(x) + [1 - \chi_R(x)]f\,\frac{N_D(x)}{N} \qquad \text{Equation 4-12}$$

Where $N_D(x)$ and N are the defect and atomic densities of the target material, f is the defect scattering factor, $\chi_R(x)$ is the random fraction of the total ion beam, and 1- $\chi_R(x)$ is the channeled part of the ion beam. The value of the scattering factor f depends on the contribution of different types of defects to direct scattering. For dislocation loops, f is approximately zero and for point defects, the value of f is one.

The dechanneled fraction $\chi_R(x)$ of the beam can be approximated using the formula:

$$\chi_R(x) = \chi_V(x) + [1 - \chi_V(x)]P(x, \tilde{\theta}_C) \qquad \text{Equation 4-13}$$

Where $P(x, \tilde{\theta}_C)$ is the probability that a channeled particle becomes dechanneled due to scattering of defects at angle, $\tilde{\theta}_C$. In thin film analysis, the beam path length is very short and the probability can be considered to be almost zero. With these approximations $\chi_R(x) = \chi_V(x)$.

Substituting this value in above equation and with the value of f =1, the equation simplifies to:

$$\frac{N_D(x)}{N} = \frac{\chi_D(x) - \chi_V(x)}{1 - \chi_V(x)} \qquad \text{Equation 4-14}$$

Final approximation can be made at the near surface region of the damaged crystal to the concentration $N_D(0)$ of the displaced atoms. The disorder concentration $N_D(0)$ then can be written as:

$$\frac{N_D(0)}{N} = \frac{\chi_D(0) - \chi_V(0)}{1 - \chi_V(0)} \qquad \text{Equation 4-15}$$

Where $\chi(0)$ is the ration of aligned to random yields in the energy window ΔE where the disorder is evaluated [34].

4.2.7 RBS-C Analysis for C Implanted 4*H*-SiC

Figure 4.6 shows the RBS-C spectra of C implantation in 4*H*-SiC at low energy of 60 keV for four different fluences: 1.85×10^{14} ions/cm^2, 3.5×10^{14} ions/cm^2, 7×10^{14} ions/cm^2, and 1×10^{15} ions/cm^2. These fluences can also be related in terms of dpa. The dpa is defined as the

fraction of atoms that have been displaced from lattice site by projectiles or recoils. The dpa has been calculated at the damaged peak with SiC density of 9.64×10^{22} atoms/cm^3. The corresponding dpa values after conversion are 0.0518, 0.0984, 0.196 and 0.280 for the fluences of 1.85×10^{14} ions/cm^2, 3.5×10^{14} ions/cm^2, 7×10^{14} ions/cm^2, and 1×10^{15} ions/cm^2, respectively. The aligned spectrum of virgin 4*H*-SiC and the random spectrum was also included in the Figure 4.6 for comparison. The leading edges of Si and C are found to be at channel numbers 567 and 249 respectively. The kinematic factors of Si and C were found to be 0.585 and 0.2735 and were discussed earlier in the section on kinematic factor in this chapter. In the Figure 4.6, the X-axis has the units of channel number and the top part of the X-axis is expressed in energy with units of keV. The channel to energy conversion is obtained using the method discussed in the section of Channel number to Energy conversion.

The reduction in the yield of backscattered particles is graphically visible by comparison of the aligned spectrum to random spectrum. The minimum yield χ_{min} which is defined as the ratio of the aligned to random yield is found to 0.037 which shows that the crystal obtained is of good quality. Thus almost 96% of the beam is channeled. The minimum yield increases as the fluence increases. The surface peak emerges in the aligned spectrum which represents the interaction of the ion beam with the first monolayer of the target. The surface peak is a measure of surface order whereas the minimum yield shows the quality of the crystal. Ion scattering and channeling both can be used to determine the amount of lattice disorder and lattice location of impurities such as interstitial or substitutional.

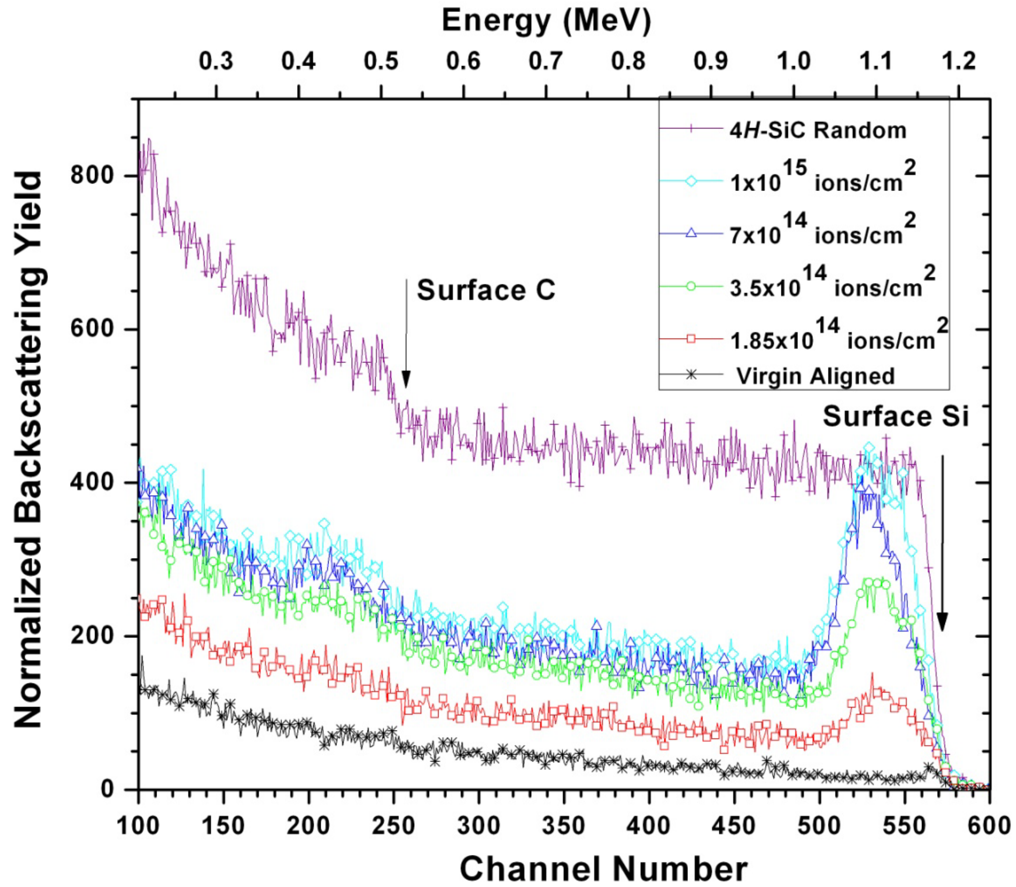

Figure 4.6 : RBS-C spectra of 60 keV C implanted 4*H*-SiC samples at room temperature using a 2 MeV He^{+} beam. The increase in backscattering signal (between channel 500 and 570) indicates the increase in the disorder due to increase in ion fluence.

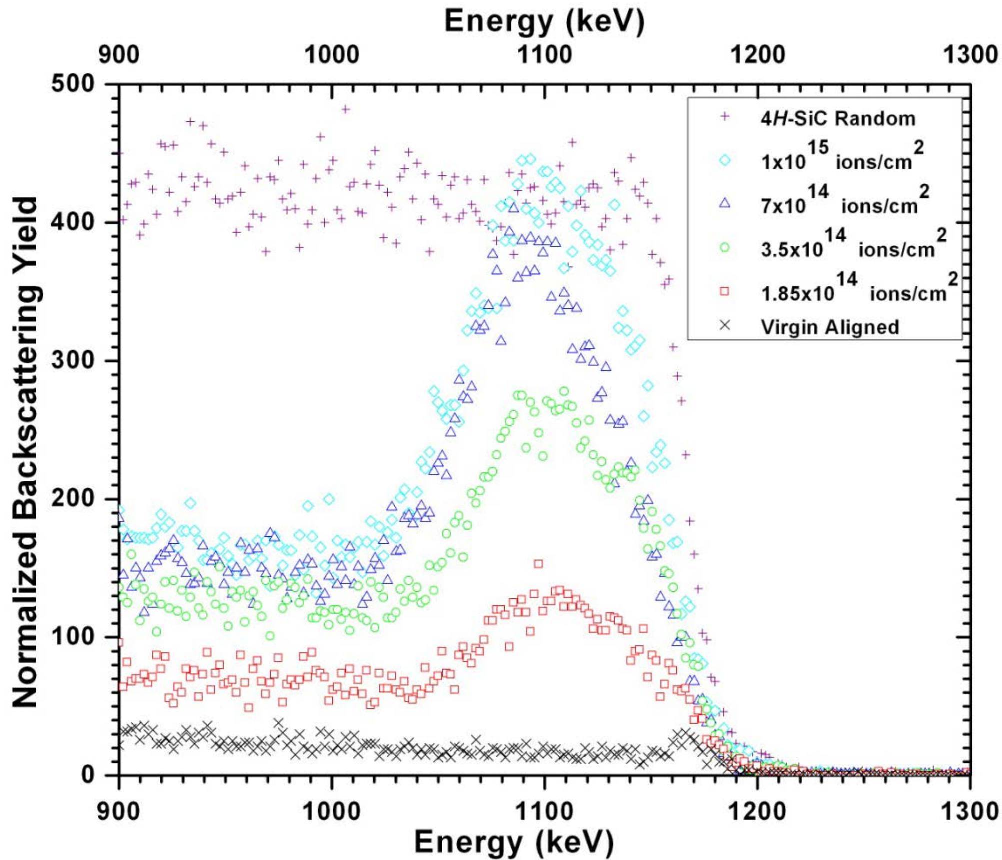

Figure 4.7: RBS-C spectra of C implantation in 4*H*-SiC in Si sub-lattice region.

The carbon yield is overlapped by the broad silicon background as shown in Figure 4.7. Because of this, the backscattering yield from carbon sub-lattice of SiC is difficult to detect. Since the backscattered yield is more evident for the Si sub-lattice than the C sub-lattice the disorder has been evaluated at Si sub-lattice. The figure above shows the RBS-C spectrum of all the implanted fluences in Si sub-lattice region.

The damage peak emerges starting from the lowest fluence of 1.85×10^{14} ions/cm^2 C implantation which corresponds to 0.0518 dpa. The backscattering yield of the damage layer appears to reach the random level for the implanted sample of highest fluence of 1×10^{15} ions/cm^2. The depth is evaluated for the implanted samples using the stopping power of He^+ ion in SiC. When He^+ ion passes through SiC target it loses energy through interactions with

electrons that are raised to excited states or ejected from atoms. The He ion can also transfer energy to the nuclei of the solid through small angle scattering events. This energy loss, which is called nuclear collisions, is much smaller than the electronic collisions.

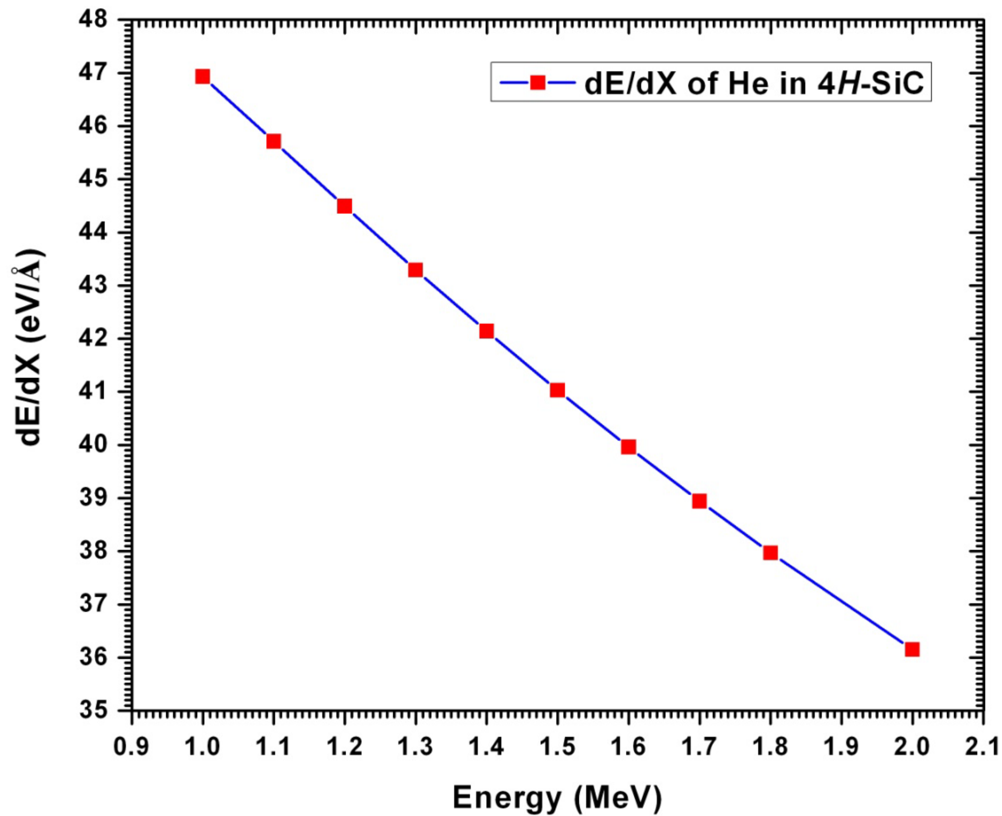

Figure 4.8 : Linear Plot of dE/dX of ^{4}He in SiC used to evaluate the depth profile. The energy loss value of electronic and nuclear collision can be determined using SRIM-2011.

The electronic energy loss of 2 MeV He^+ ions in SiC as calculated from SRIM-2011 has a value of about 361.5 eV/nm. Figure 4.8 shows the dE/dx of He^+ ion from energy 1 MeV to 2 MeV. The depth is divided into slabs with each slab of thickness of 5 nm. The energy loss, dE/dx, and the incoming and outgoing energies were calculated at each individual slab. The energy backscattered from the surface peak was calculated from KE_0 where K is the kinematic factor of Si (0.58) and E_0 is the incident energy of He^+ (2 MeV). The backscattered energy of Si is calculated to be 1170 keV.

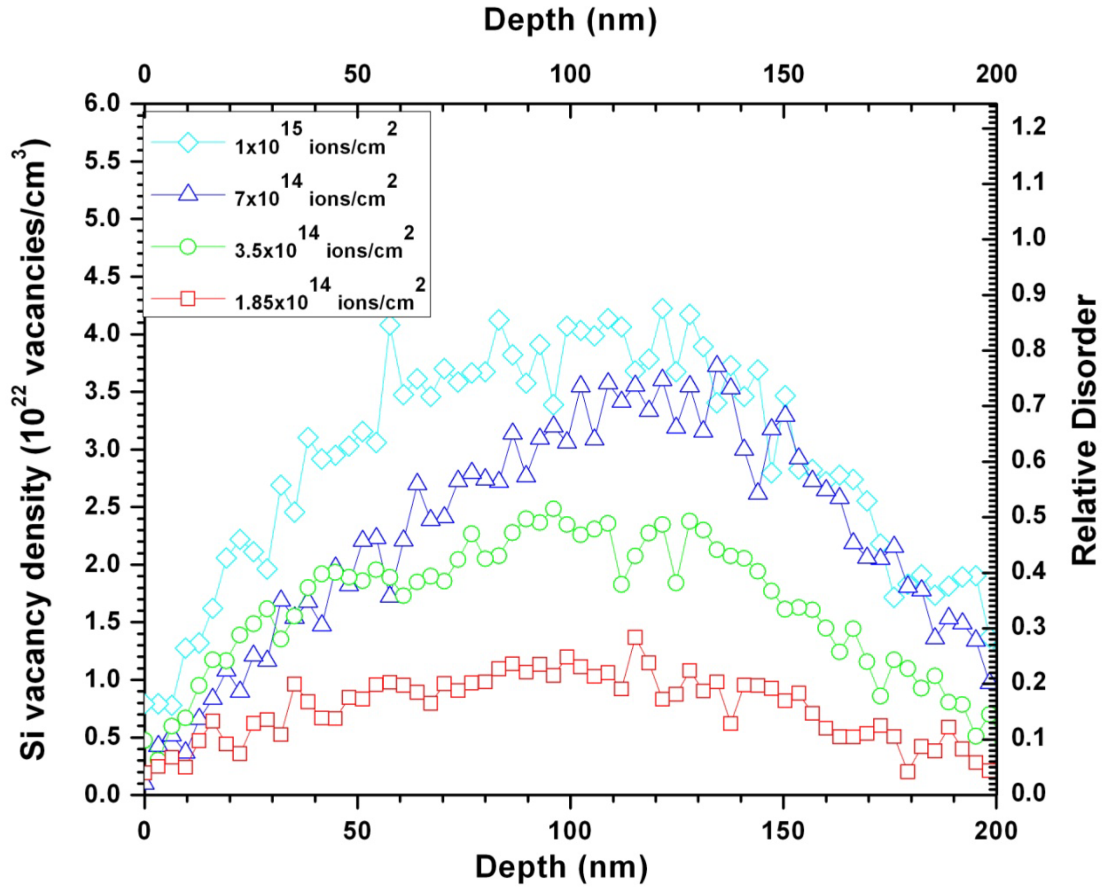

Figure 4.9 : Relative disorder of the Si sub-lattice in 60 keV C implanted 4*H*-SiC samples as a function of depth. The depth of the damage peak was found to be 110±10 nm. Si vacancy density was calculated by multiplying relative disorder with atomic density of Si (4.82×10^{22} atoms/cm^3) in 4*H*-SiC.

The disorder profile was extracted after all the implanted samples spectra were subtracted from the aligned spectrum by considering a linear dechanneling approximation for all the spectra [35, 36]. The resultant depth profile plot is shown in Figure 4.9. The damage peak for all the implanted fluences is 110±10 nm, which is in agreement with the SRIM simulated depth of 116±16 nm, is shown in Figure 4.9. The simulations and more details about this were discussed in the previous chapter. The damage peak remained constant for all the implanted fluences showing that there is no diffusion in the implanted sample. For the sample implanted with the

lowest fluence of 1.85×10^{14} ions/cm^2, which corresponds to a dpa value of 0.052 at the damage peak, shows low-level disorder of about 28%. For the next highest implanted fluence of 3.5×10^{14} ions/cm^2, which corresponds to a dpa value of 0.098 at the damage peak, 50% of the relative disorder is found. The disorder increases to 75% for the implanted fluence of 7×10^{14} ions/cm^2, which corresponds to a dpa value of 0.196 at the damage peak. For the highest implanted fluence of 1×10^{15} ions/cm^2, which corresponds to a dpa value of 0.280 at the damage peak, 92% of relative disorder is found. The disorder values are calculated using the yield ratios for implanted samples aligned and in random position, where 100% disorder corresponds to total amorphization in the sample.

4.2.8 RBS-C Analysis for Si Implanted 4*H*-SiC

In the next step of the present research work, Si was implanted in 4*H*-SiC at energy of 60 keV. The implanted fluences were 5.5×10^{13} ions/cm^2, 1.1×10^{14} ions/cm^2, 2.2×10^{14} ions/cm^2, and 3.2×10^{14} ions/cm^2. The dpa values calculated for these implanted fluences are 0.052, 0.103, 0.205 and 0.298, respectively. All the dpa values are calculated at the damage peak with the SiC density of 3.21 g/cm^3 or 9.64×10^{22} atoms/cm^3. The displacement energies of 20 and 35 eV were used in TRIM simulations for C and Si respectively. The current on the target was maintained at 200 nA to avoid sample heating. All the implantations were done at room temperature. RBS-C aligned spectra for all the implanted fluences are shown in the figure below. For comparison the virgin aligned and random spectra were also shown in Figure 4.10.

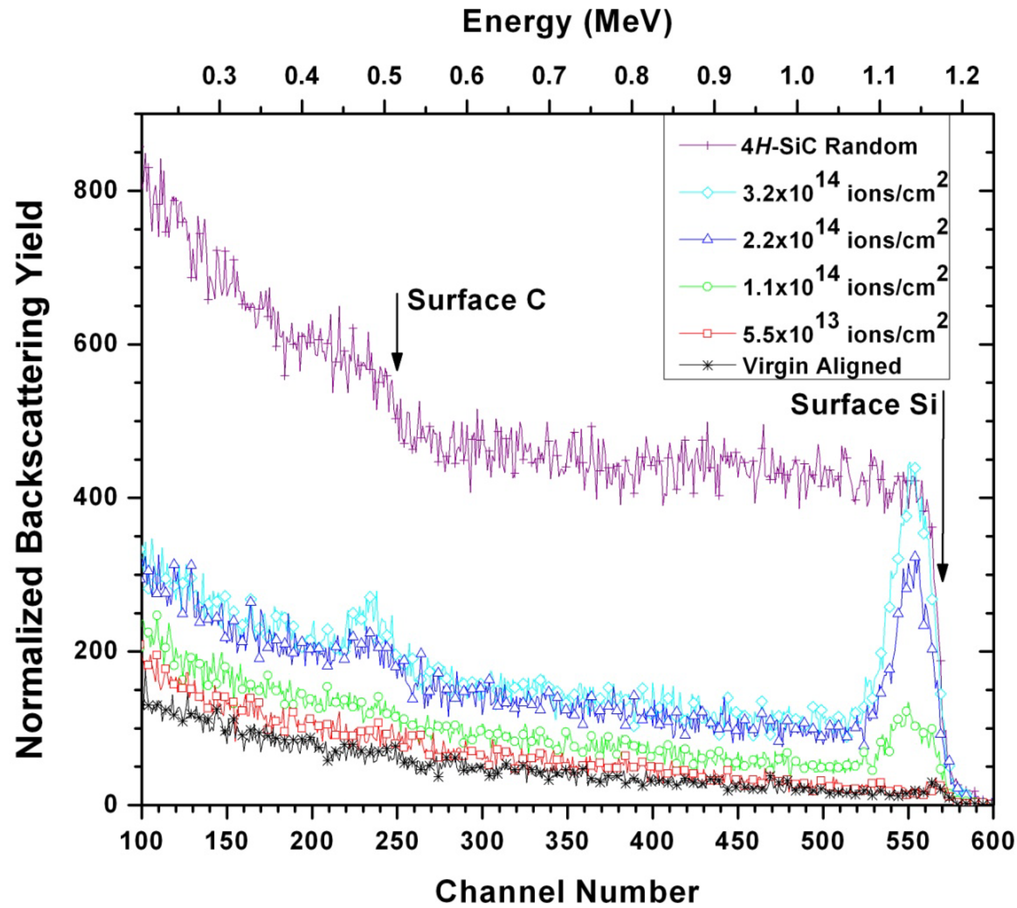

Figure 4.10 : RBS-C spectra of Si implantation in 4*H*-SiC.

Similar methods of channel to energy conversion were used as discussed earlier for the RBS-C spectra of C implantation in 4*H*-SiC. As the disorder is more pronounced in Si sub-lattice region, the disorder profile has been evaluated in only the Si sub-lattice. Figure 4.11 shows the RBS-C spectra of Si implanted 4*H*-SiC in the Si sub-lattice region. The energy of the backscattered He^+ ions is related to the depth of the target material. Hence the depth profiles of the dechanneling yield from Si atoms can be obtained from the RBS-C spectra. Figure 4.12 shows the depth profile as a function of Si disorder.

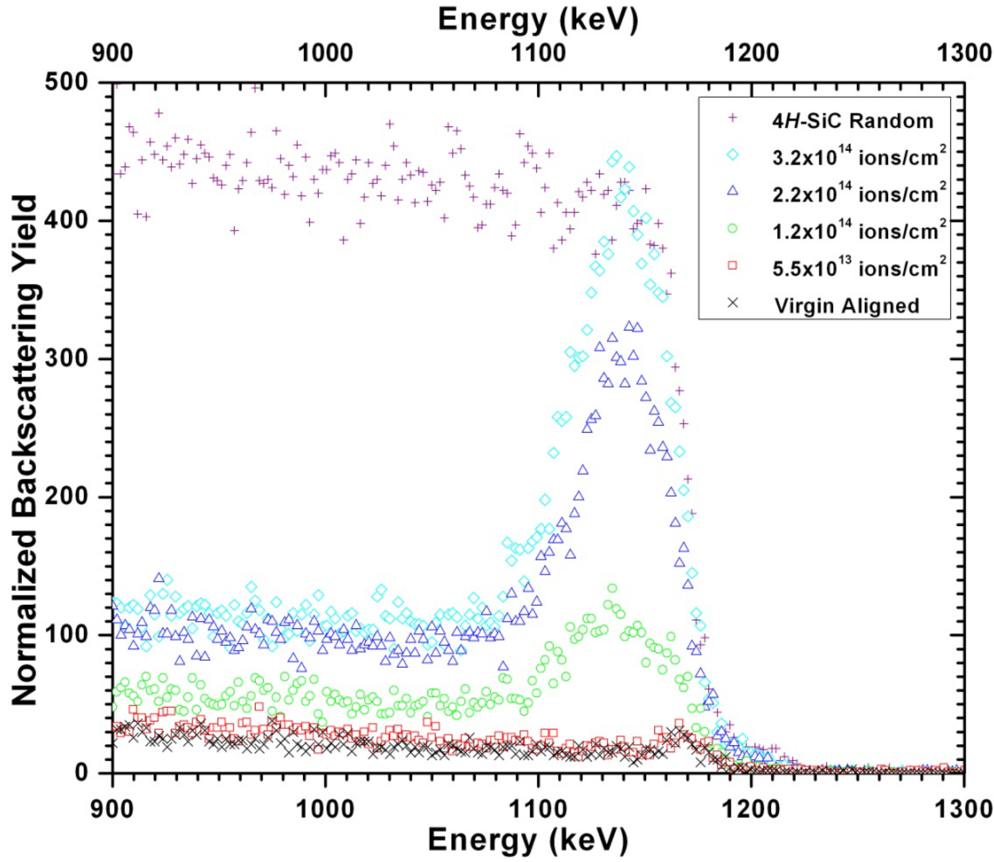

Figure 4.11 : RBS-C spectra of Si implanted 4*H*-SiC in Si sub-lattice region.

It can be seen from Figure 4.12 that the damage peak for all the implanted fluences is at about 50±5 nm, which agrees with the TRIM simulations, which was at 56±9 nm. The damage peak remained constant for all the implanted fluences. For the sample implanted with the lowest fluence of 5.5×10^{13} ions/cm^2, which corresponds to a dpa value of 0.05, the disorder was not evaluated. For the next highest implanted fluence of 1.1×10^{14} ions/cm^2, which corresponds to a dpa value of 0.103 at the damage peak, 26% of the relative disorder is found. The disorder increases to 70% for the implanted fluence of 2.2×10^{14} ions/cm^2, which corresponds to a dpa value of 0.205 at the damage peak. For the highest implanted fluence of 3.2×10^{14} ions/cm^2, which corresponds to a dpa value of 0.298 at the damage peak, 94% of the relative disorder is

found. The relative damage on the Si sub-lattice on Si- and C-implanted 4*H*-SiC with respect to different fluences are shown in Table 1.

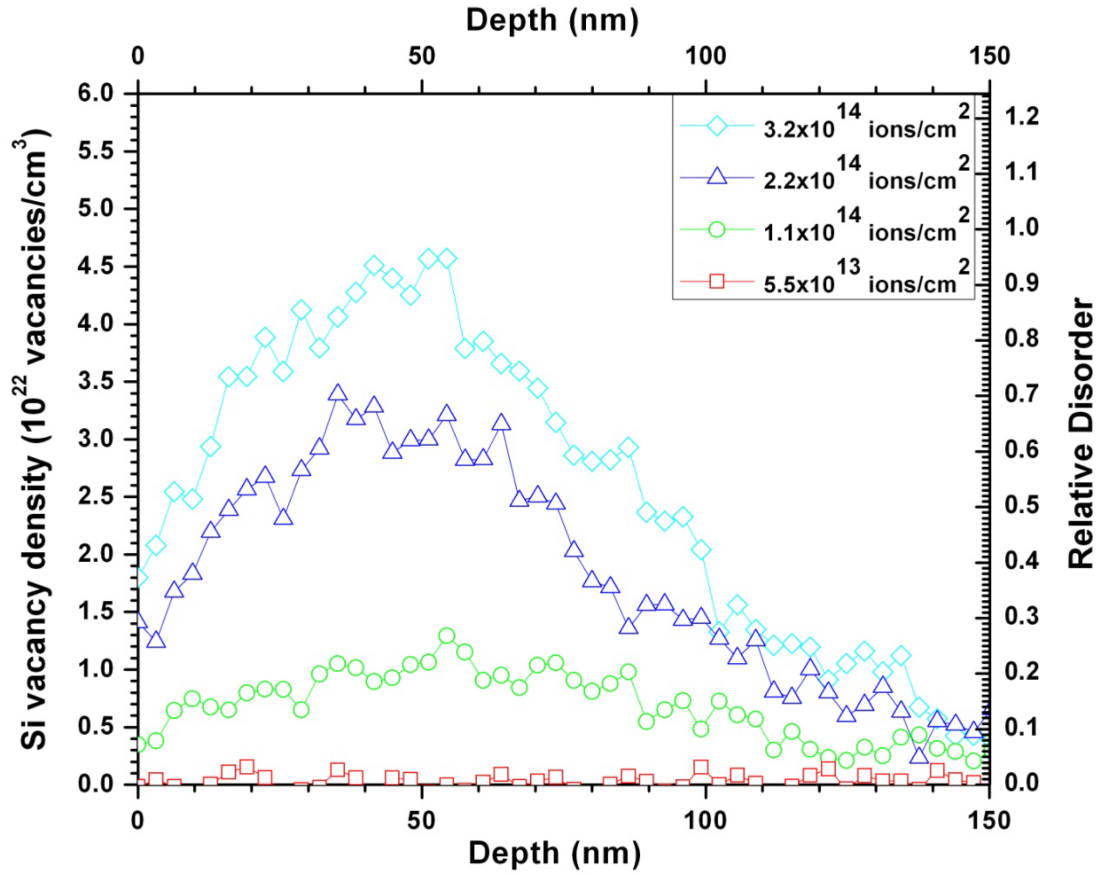

Figure 4.12 : Relative disorder of the Si sub-lattice in 60 keV Si implanted 4*H*-SiC samples as a function of depth. The depth of the damage peak was found to be 50±5 nm. Si vacancy density was calculated by multiplying relative disorder with atomic density of Si (4.82×10^{22} atoms/cm^3) in 4*H*-SiC.

Table 4.1: Relative damage on Si sub-lattice extracted from RBS-C data for different fluences of 60 keV Si and C implanted in 4*H*-SiC.

Fluence of 60 keV Si implantation in4*H*-SiC (cm^{-2})	Relative damage on Si sub-lattice from RBS-C data (%)	Fluence of 60 keV C implantation in 4*H*-SiC (cm^{-2})	Relative damage on Si sub-lattice from RBS-C data (%)
5.5×10^{13}	-	1.85×10^{14}	28
1.1×10^{14}	26	3.5×10^{14}	50

2.2×10^{14}	70	7×10^{14}	75
3.2×10^{14}	94	1×10^{15}	92

4.3 Raman Analysis of Ion Implantation in 4*H*-SiC

Raman spectroscopy is one of the contactless and non-destructive techniques, which is widely used for the study of semiconductors. It is used to identify the material and yield information about carrier concentration, impurity content, crystal structure, and mechanical strain. It is commonly used as a characterization tool for identification of SiC polytypes, to determine lattice disorder and strain, impurities, free carrier density, and mobility [37 - 39]. Raman spectroscopy is mostly used as complementary with RBS-C to probe the implantation-induced disorder. The following sections shows the Raman results obtained in C and Si implanted 4*H*-SiC material.

4.3.1 Raman Results for C Implanted 4*H*-SiC at the Energy of 60 keV

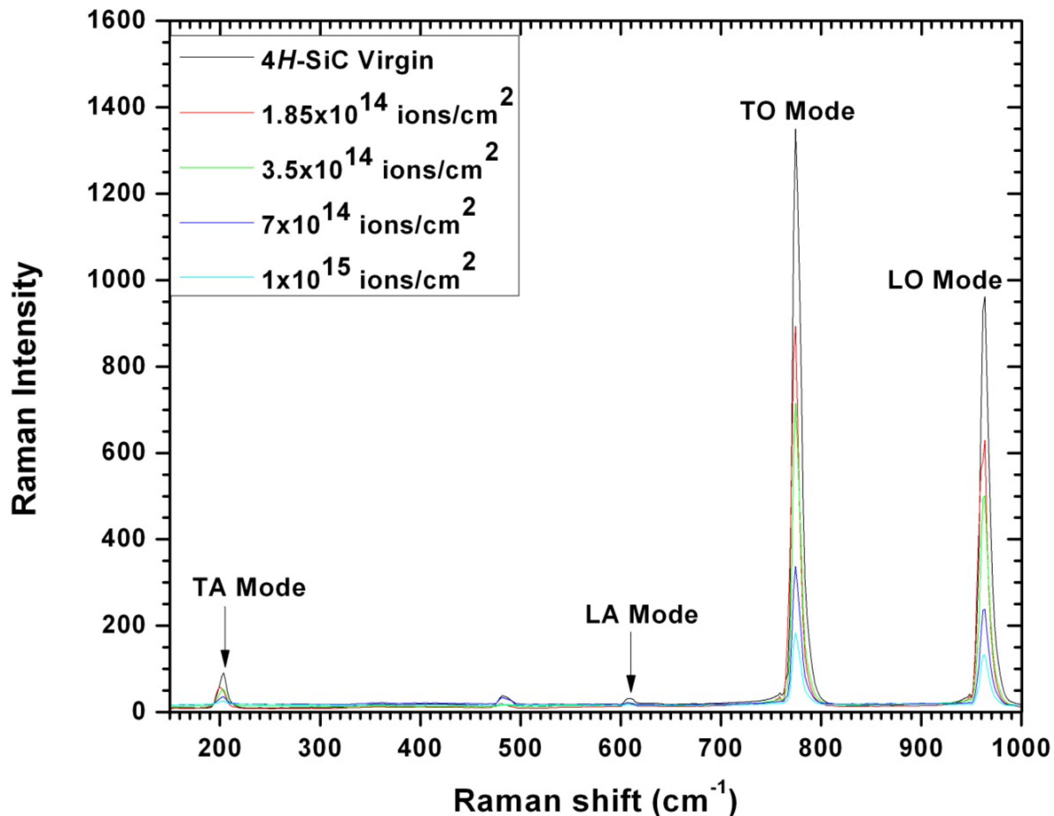

Figure 4.13 : Raman spectra of 60 keV C implanted at different fluences in 4*H*-SiC.

Four different fluences of C were implanted in 4*H*-SiC at the energy of 60 keV. The fluences ranged from 1.85×10^{14} ions/cm^2 to 1×10^{15} ions/cm^2. The implantation-induced-disorder was studied using Raman spectroscopy. The Raman system was calibrated using silicon as the standard, where the main Si phonon peak was seen at 521 cm^{-1}. After calibration of the system, the spectrum for all the implanted fluences along with the virgin was taken and is as shown in the Figure 4.13. The green laser which has a wavelength of 532 nm is used as an excitation source with the power of 6 mW on the sample. The spot size of the laser beam on the sample was around 1.1 μm. A 50× objective was used for focusing, which has a numerical aperture of 0.5. All the measurements were taken at room temperature. The spectrum was collected in the broad spectral region between 150 cm^{-1} to 1000 cm^{-1}.

The number of phonon branches in any crystal is given by 3N, where N is the number of atoms per unit cell. Out of these 3N modes, 3N-3 are optical and 3 are acoustic modes. 4*H*-SiC has 8 atoms per unit cell, which gives rise to total of 24 phonon modes. Out of these 24 phonon modes, 3 are acoustic and 21 are optical modes. Only some of these modes are active in Raman scattering. These modes are degenerate in certain directions of the Brillouin zone and are classified into transverse and longitudinal modes. 4*H*-SiC which is one of the hexagonal polytypes has a well-defined c-axis. The longitudinal modes, which are parallel to c-axis, are also called the axial modes, whereas the transversal modes, which are perpendicular to c-axis, are called as planar modes.

The major peaks for the first order band in 4*H*-SiC consists of E_1, E_2 and A_1 phonon modes and can be identified as planar or transverse acoustic mode (E_2) at 204 cm^{-1}, axial or

longitudinal acoustic mode (A_1) at 610 cm^{-1}, planar optic mode (E_2) at 775 cm^{-1} and axial optic mode (A_1) at 964 cm^{-1} [40]. The range from 100-600 cm^{-1} is attributed to Si-Si vibrations 700-1000 cm^{-1} to Si-C vibrations [41].

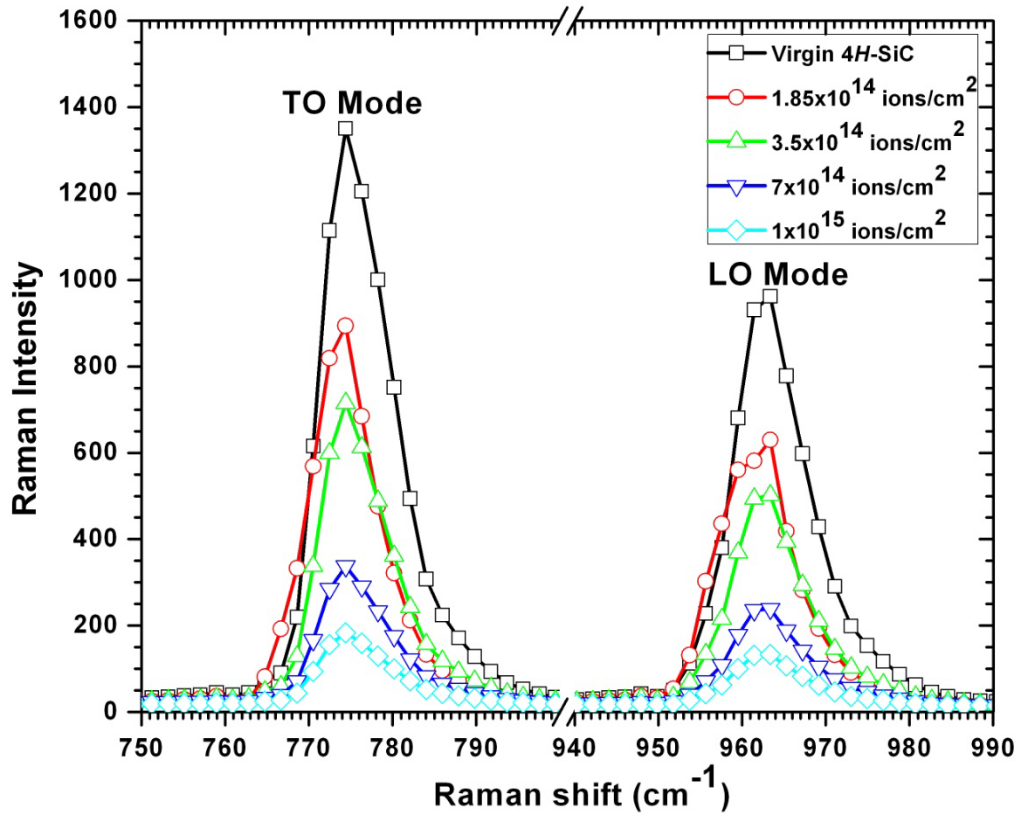

Figure 4.14: Raman spectra of low energy 60 keV C implanted 4*H*-SiC samples. The TO (775 cm^{-1}) and LO (964 cm^{-1}) mode signals are compared in order to determine the amount of disorder in the implanted samples.

Figure 4.14 shows the TO and LO modes for C implantation in 4*H*-SiC at different fluences. The virgin spectrum is also included for comparison. As one can see from the Figure 4.14, the Raman spectra show a strong dependence on the intensity of the main Raman phonon modes. This is related to the implantation-induced-damage, which determines the decrease in intensity [42]. The intensity gradually decreases as the fluence increases. The reduction in intensity is caused by the decrease in Raman polarizability because of the breaking of bonds and

changes in atomic forces and displacements. No Raman shift has been found for both the modes implying that no strain has been detected.

4.3.2 Raman Results for Si Implanted 4*H*-SiC at Low Energy 60 keV

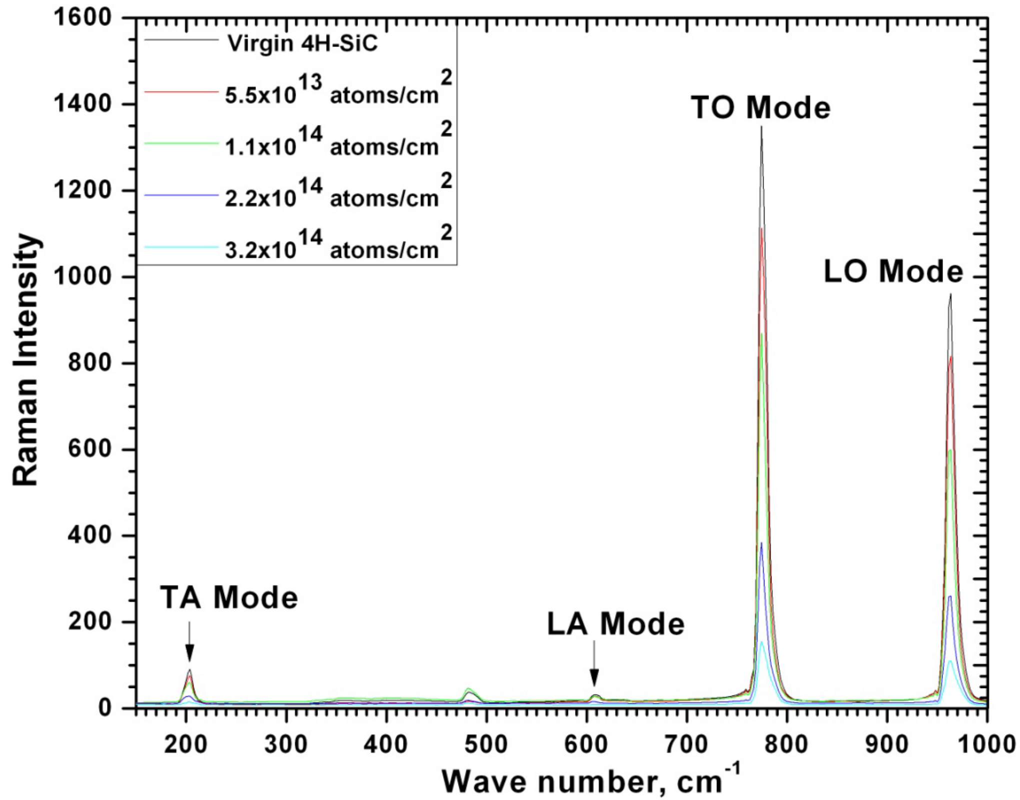

Figure 4.15: Raman spectra of 60 keV Si implanted at different fluences in 4*H*-SiC.

Figure 4.15 shows the Raman spectra of Si implantation in 4*H*-SiC at the energy of 60 keV at different fluences along with virgin 4*H*-SiC. The fluences implanted are 5.5×10^{13} ions/cm^2, 1.1×10^{14} ions/cm^2, 2.2×10^{14} ionscm^2, and 3.2×10^{14} ions/cm^2. The spectra were collected with the same experimental conditions as mentioned in the above section.

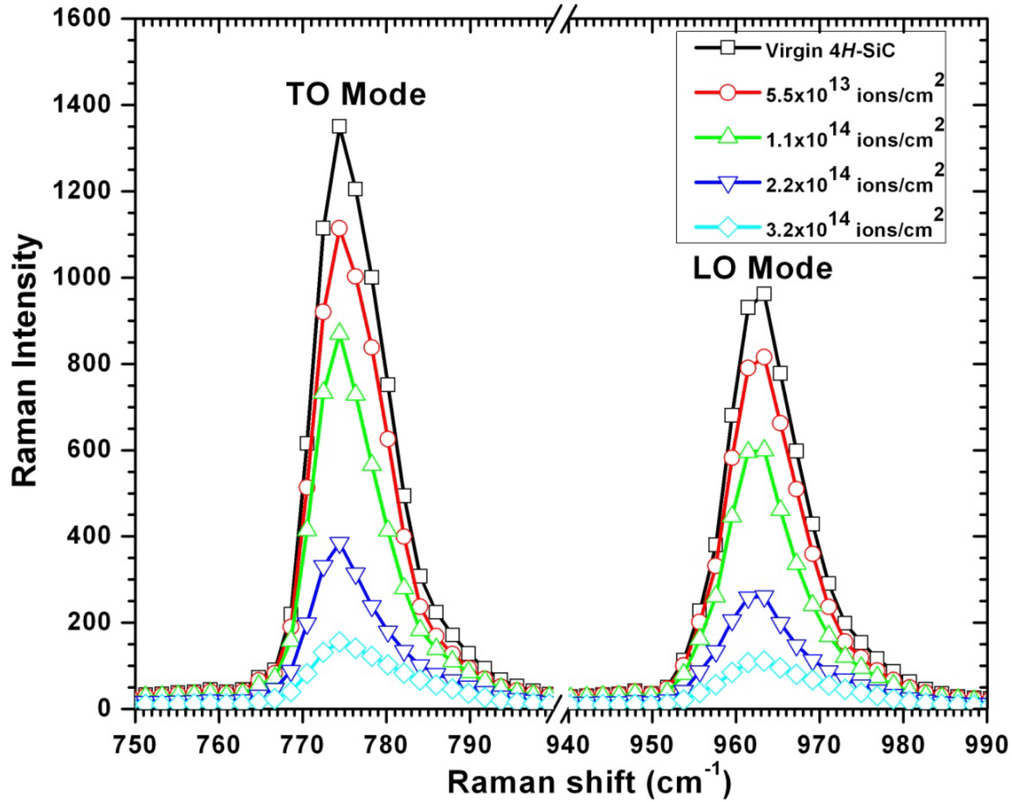

Figure 4.16: Raman spectra of low energy 60 keV Si implanted 4*H*-SiC samples. The TO (775 cm^{-1}) and LO (964 cm^{-1}) mode signals are compared in order to determine the amount of disorder in the implanted samples.

Since the Si-C vibrational mode is the region of interest, the disorder has been studied in that range and is shown in the Figure 4.16. The only change observed in these spectra is the decrease of intensity of the Raman modes as the fluences increases. This decrease in intensity is related to implantation-induced-damage in 4*H*-SiC, which indicates the appearance of defects after implantations.

4.4 Disorder Evaluation for C and Si Implanted 4*H*-SiC Samples

An energetic ion, when implanted into the material, produces disorder. The crystallinity of the material eventually changes into the amorphous state with the increase of disorder. The amount of disorder for Si and C implanted samples in 4*H*-SiC was quantified by the normalized

relative intensity of the Raman line, $I_n = (I_0 - I)/I_0$, where I_0 and I are the intensities of the virgin and implanted samples at different fluences, respectively [43]. $I_n = 0$ corresponds to the crystallinity of the sample, whereas $I_n = 1$ corresponds to the total amorphization.

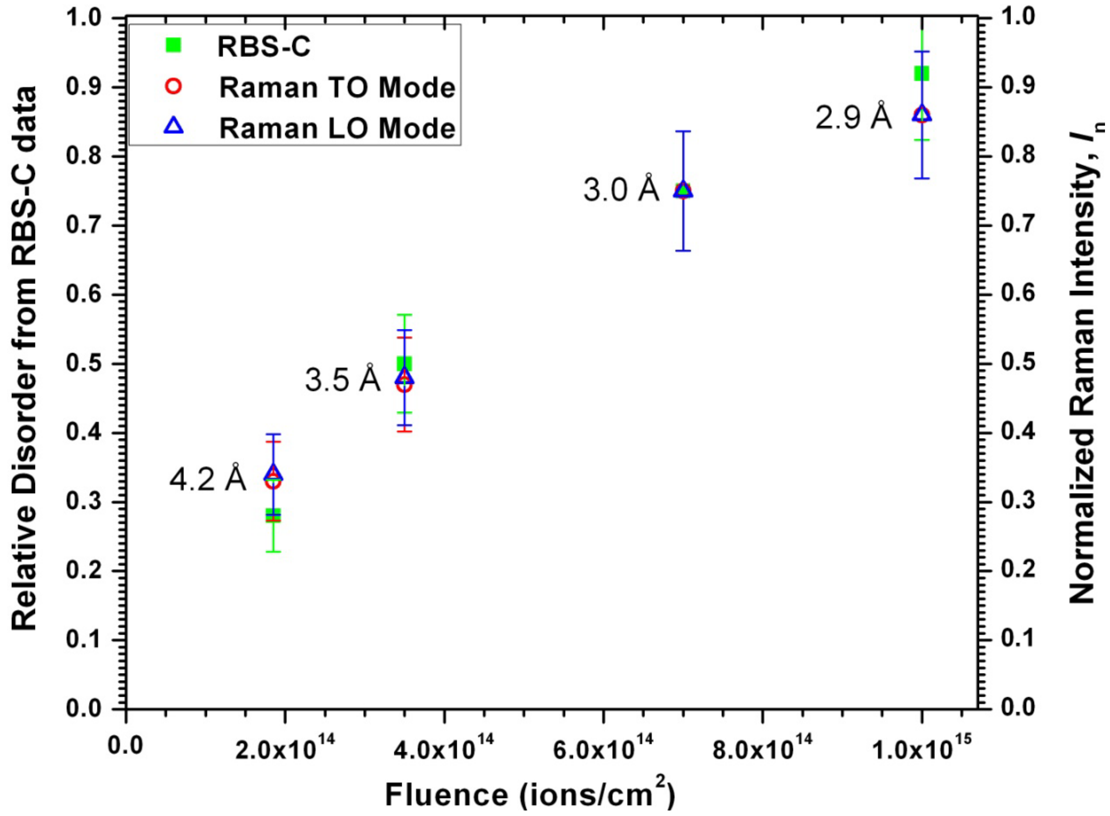

Figure 4.17: Relative disorder of 60 keV C implanted at different fluences in 4*H*-SiC from RBS-C and the TO and LO modes of Raman spectra.

Figure 4.17 shows the disorder evaluated from both RBS-C and Raman results as a function of implanted fluences for C implantation in 4*H*-SiC. For the sample implanted with lowest fluence of 1.85×10^{14} ions/cm^2, which corresponds to dpa of 0.0518 at the damage peak, the disorder from Raman is calculated to be 33%, whereas 28% of disorder has been determined using the RBS-C spectral results. The level of disorder as calculated from Raman results shows an increase to 47% and 75% for the implanted fluences of 3.5×10^{14} ions/cm^2 (0.098 dpa) and 7×10^{14} ions/cm^2 (0.196 dpa), respectively. For the same fluences, the disorder level is found to

be 50% and 75% from RBS-C results. 92% disorder has been determined for the highest implanted fluence of 1×10^{15} ions/cm^2 (0.28 dpa at the damage peak) from RBS-C, while Raman results showed the disorder of about 86%.

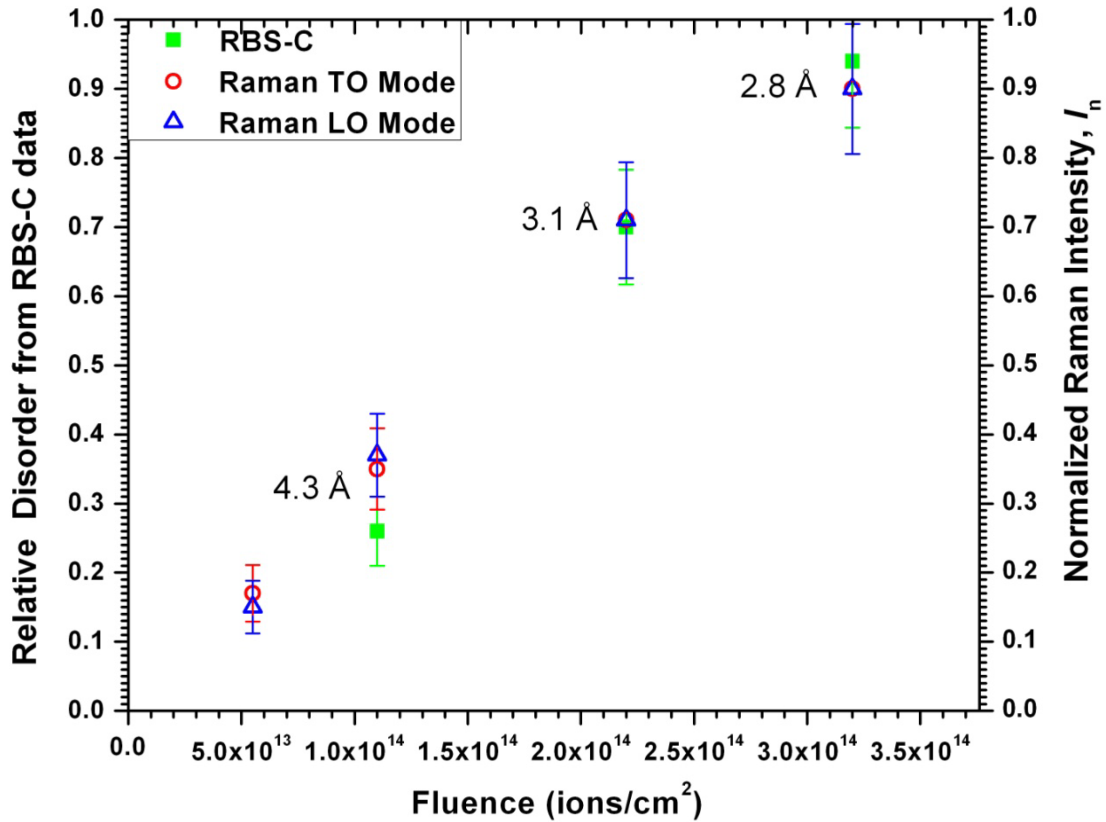

Figure 4.18: Relative disorder of 60 keV Si implanted at different fluences in 4*H*-SiC from RBS-C and TO and LO modes of Raman spectra.

Figure 4.18 shows the disorder profile as a function of the implanted fluences for all the implanted fluences for Si implantation in 4*H*-SiC at the energy of 60 keV. The disorder has been evaluated in the similar way as mentioned above. For the lowest Si implanted fluence of 5.5×10^{13} ions/cm^2, which corresponds to 0.0513 dpa at the damage peak, 17% of disorder has been calculated from the Raman intensity. No disorder was found from RBS-C results, but the results only showed the evidence of disorder introduction by only a slight increase in the de-channeling yield over that of the un-implanted sample. For the next higher implanted fluences of

1.1×10^{14} ions/cm^2 and 2.2×10^{14} ions/cm^2, the disorder level increased to 37% and 71%, respectively. From RBS-C results, the disorder level for 1.1×10^{14} ions/cm^2 was found to be 26%, which was less than the Raman results. For the fluence of 2.2×10^{14} ions/cm^2, the RBS-C disorder results were found to be 71%, which is very close to Raman results. For the highest implanted fluence, the disorder from Raman and RBS-C results were calculated to be 94%. The uncertainty in calculating the relative disorder percentages is less than 10%. The disorder results calculated from both the techniques show good agreement with each other. These two complimentary techniques have confirmed the disorder created in both Si and C implanted 4*H*-SiC for different fluences.

From SRIM simulations, the deposition energy density is calculated in the range of 3.41×10^{23} eV/cm^3 to 1.98×10^{24} eV/cm^3 for Si implantation and of 2.96×10^{23} eV/cm^3 to 1.6×10^{24} eV/cm^3 for C implantation. These values are obtained using the threshold displacement energies of 20 eV and 35 eV for C and Si sub-lattices, respectively. Different values of displacement energies for both C and Si lead to different values for critical damage energy for amorphization. Previous reports state that different values of displacement energies [44, 45] have been used for the evolution of the damage with SRIM. From SRIM, the energy densities for the highest fluences of C and Si implanted samples were 1.6×10^{24} eV/cm^3 and 1.98×10^{24} eV/cm^3, respectively. The relative Si disorders corresponding to these energy density values were 92% and 94% for C and Si, respectively. This is in good agreement with previous results where the critical energy density for complete amorphization of SiC is between 2.0×10^{24} eV/cm^3 and 2.4×10^{24} eV/cm^3 [46].

Si implantations with fluences of 1.1×10^{14} cm^{-2}, 2.2×10^{14} cm^{-2}, and 3.2×10^{14} cm^{-2} induce Si sub-lattice damages of 26%, 70%, and 94%, respectively. From RBS-C Si sub-lattice

measurements for these fluences, Si vacancy densities at the damage peak are calculated to be of 1.29×10^{22} cm^{-3}, 3.21×10^{22} cm^{-3}, and 4.57×10^{22} cm^{-3} which corresponds to 4.26 Å, 3.14 Å, and 2.79 Å average distances of Si vacancies, respectively. The Si vacancy density is calculated by multiplying the relative disorder ratio with the atomic density of Si (4.82×10^{22} cm^{-3}) in 4*H*-SiC. The average distance between vacancies is calculated from the formula, $d_{\text{vac}} = \sqrt[3]{\frac{1}{n}}$ where n is the Si vacancy density and d_{vac} is the average distance between vacancies [47]. Similarly, for C implanted with fluences of 1.85×10^{14} cm^{-2}, 3.5×10^{14} cm^{-2}, 7×10^{14} cm^{-2}, and 1×10^{15} cm^{-2}, Si vacancy densities of 1.37×10^{22} cm^{-3}, 2.3×10^{22} cm^{-3}, 3.6×10^{22} cm^{-3}, and 4.22×10^{22} cm^{-3} were calculated from RBS-C Si sub-lattice measurements. These Si vacancy densities correspond to 4.17 Å, 3.51 Å, 3.02 Å, and 2.87 Å average distances of Si vacancies, respectively. At high defect concentrations, there may be the presence of anti-site defects and defect clusters. Both dynamic and kinetic processes at room temperature contribute to the formation of those defects. In our experiments involving low ion fluences, we assume that the effects caused by the presence of those defects are negligible, while calculating the average distance of the Si vacancies.

Table 4.2 and 4.3 show the fluences and dpas at the damage peak and the corresponding average distances of Si vacancies calculated from TRIM simulations and from the implanted Si and C fluences in 4*H*-SiC. Note that SRIM does not include kinetic processes that can result in simultaneous defect recovery. Table 4.4 and 4.5 show the fluences and relative damage on Si sub-lattice from RBS-C data and relative disorder from Raman measurements for C and Si implantations respectively.

Table 4.2: dpa and average distance of vacancies at the damage peak position (50±5 nm) calculated as a function of 60 keV Si implantation fluences in 4*H*-SiC. The estimation of the error in the average distance of vacancies stems from the statistical error found in the relative disorder ratio.

Fluence of 60 keV Si implantation in n-type 4*H*-SiC (cm^{-2})	Displacement per atom (dpa) at the damage peak	Avg. dist. of total vac. (Å) from TRIM	Avg. dist. of Si vac. (Å) from RBS-C data at the damage peak
5.5×10^{13}	0.052	5.9	-
1.1×10^{14}	0.103	4.7	4.26±0.07
2.2×10^{14}	0.205	3.7	3.14±0.08
3.2×10^{14}	0.298	3.3	2.79±0.09

Table 4.3: dpa and average distance of vacancies at the damage peak position (110±10 nm) calculated as a function of 60 keV C implantation fluences in 4*H*-SiC. The estimation of the error in the average distance of vacancies stems from the statistical error found in the relative disorder ratio.

Fluence of 60 keV C implantation in n-type 4*H*-SiC (cm^{-2})	Displacement per atom (dpa) at the damage peak	Avg. dist. of total vac. (Å) from TRIM	Avg. dist. of Si vac. (Å) from RBS-C data at the damage peak
1.85×10^{14}	0.052	5.8	4.17±0.07
3.5×10^{14}	0.098	4.7	3.51±0.08
7×10^{14}	0.196	3.7	3.02±0.06
1×10^{15}	0.28	3.3	2.87±0.09

Table 4.4: Relative damage on Si sub-lattice from RBS-C data and relative disorder from Raman measurements for implanted C fluences in n-type 4*H*-SiC at low energy 60 keV.

Implanted C fluences in n-type 4*H*-SiC at low energy 60 keV (ions/cm^2)	Relative damage on Si sub-lattice from RBS-C data (%)	Relative disorder from Raman measurements (%)
1.85×10^{14}	28	33
3.5×10^{14}	50	47
7×10^{14}	75	75
1×10^{15}	92	86

Table 4.5: Relative damage on Si sub-lattice from RBS-C data and relative disorder from Raman measurements for implanted Si fluences in n-type 4*H*-SiC at low energy 60 keV.

Implanted Si fluences in n-type 4*H*-SiC at low energy 60 keV (ions/cm^2)	Relative damage on Si sub-lattice from RBS-C data (%)	Relative disorder from Raman measurements (%)
5.5×10^{13}	-	17
1.1×10^{14}	26	37
2.2×10^{14}	70	71
3.2×10^{14}	94	94

4.5 Investigation of Magnetic Properties using SQUID for C Implanted n-type 4*H*-SiC

4.5.1 Introduction

This section is a discussion of experimental results of the magnetization measurements on C implanted n-type 4*H*-SiC. The magnetic properties of the virgin and implanted samples were investigated using superconducting quantum interference device (SQUID). For these measurements the samples were sent to two independent institutes where the SQUID measurements were done by staff scientists. SQUID measurements for all the implanted fluences other than 5×10^{12} ions/cm^2 were performed at the Industrial Research limited at Lower Hutt, New Zealand. For the implanted sample of fluence 5×10^{12} ions/cm^2 the SQUID measurements were performed at the University of Leipzig, Germany.

4.5.2 Experimental Results

Different fluences of C were implanted in n-type 4*H*-SiC at low energy 60 keV. The fluences implanted were 1×10^{12}, 5×10^{12}, 1×10^{13} 5×10^{14}, 8.5×10^{14}, 5×10^{15} and 1.7×10^{16} ions/cm^2 respectively. The dpa values calculated for these implanted fluences are 2.8×10^{-4}, 1.4×10^{-4}, 2.8×10^{-3}, 0.14, 0.24, 1.4 and 4.76 respectively. The current on the target was maintained at 20 nA. From TRIM – 2011 it was estimated that the vacancy creation reaches maximum to about 0.27 vacancies per carbon ion at the damage peak. This value can be used to calculate the vacancy concentration and the values are found to be 0.27×10^{20}, 1.35×10^{20}, 0.27×10^{21}, 1.35×10^{22}, 2.23×10^{22}, 1.35×10^{23} and 4.6×10^{23} respectively. These vacancy concentrations correspond to the average distance between vacancies of 3.3, 1.94, 1.54, 0.42, 0.35, 0.19 and 0.13 nm respectively. The average distance between vacancies is calculated from the formula, $d_{\text{vac}} = \sqrt[3]{\frac{1}{n}}$ where n is the vacancy concentration and d_{vac} is the average distance between vacancies. The calculated values are tabulated in Table 4.6.

Table 4.6: Different parameters calculated for C implantation in n-type 4*H*-SiC at low energy 60 keV for SQUID measurements.

C implantation in n-type 4*H*-SiC at low energy 60 keV			
Fluence (ions/cm^2)	Displacements per atom (dpa)	Vacancy concentration (vac./cm^3)	Average distance between vacancies (nm)
1×10^{12}	2.8×10^{-4}	0.27×10^{20}	3.3
5×10^{12}	1.4×10^{-4}	1.35×10^{20}	1.94
1×10^{13}	2.8×10^{-3}	0.27×10^{21}	1.54
5×10^{14}	0.14	1.35×10^{22}	0.42
8.5×10^{14}	0.24	2.23×10^{22}	0.35
5×10^{15}	1.4	1.35×10^{23}	0.19
1.7×10^{16}	4.76	4.6×10^{23}	0.13

Before implantation, one of the virgin samples was mounted on a specially designed SQUID sample holder and was magnetically pre-characterized with the SQUID at the University of Leipzig, Germany. The sample stayed on the holder for pre-characterization and post-irradiation SQUID measurements and inside a protective quartz tube with implantation window for shipping and implantation. This procedure was chosen to prevent any accidental contamination of the SiC sample by magnetic impurities. Pre-characterization by SQUID was deemed necessary to doubtlessly attribute any changes in magnetic properties to the effects of implantation. After the pre-characterization measurements at the University of Leipzig the sample holder was sent to IBMAL, UNT for implantation. After the implantation was performed

with the fluence of 5×10^{12} ions/cm^2, the implanted sample with the sample holder was sent back to the University of Leipzig for SQUID measurements.

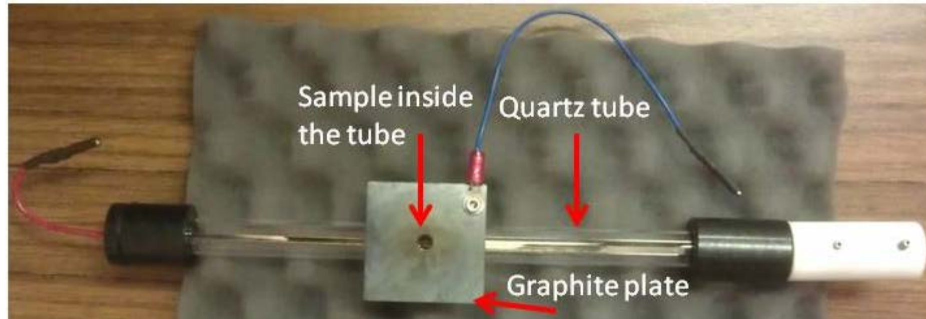

Figure 4.19: An optical image of a specially designed SQUID sample holder. n-type 4*H*-SiC sample is secured inside the quartz tube. The sample stayed inside the tube to test the compatibility before and after implantation.

The specially designed SQUID holder is shown in the Figure 4.19. The sample is secured inside the quartz tube with a circular aperture opening of diameter 5 mm. A graphite plate in front of the quartz tube with circular aperture of diameter 5 mm is used to assure the implantation into the SiC sample only.

The hysteresis curves obtained from SQUID measurements for virgin n-type 4*H*-SiC and implanted with C fluence of 5×10^{12} ions/cm^2 are shown in Figure 4.20. The magnetic field was applied in the range -10000 to 10000 Oe at both room temperature 300 K and at low temperature 5 K. The field dependency of the magnetization without subtracting the diamagnetic contribution is shown in Figures 4.20(a) and 4.20(b). A linear dependency, i.e. diamagnetic behavior, is expected for virgin n-type *4H*-SiC. In order to identify any deviations from linearity, which could be the hypothesized ferromagnetic properties after implantation, the diamagnetic contribution was subtracted.

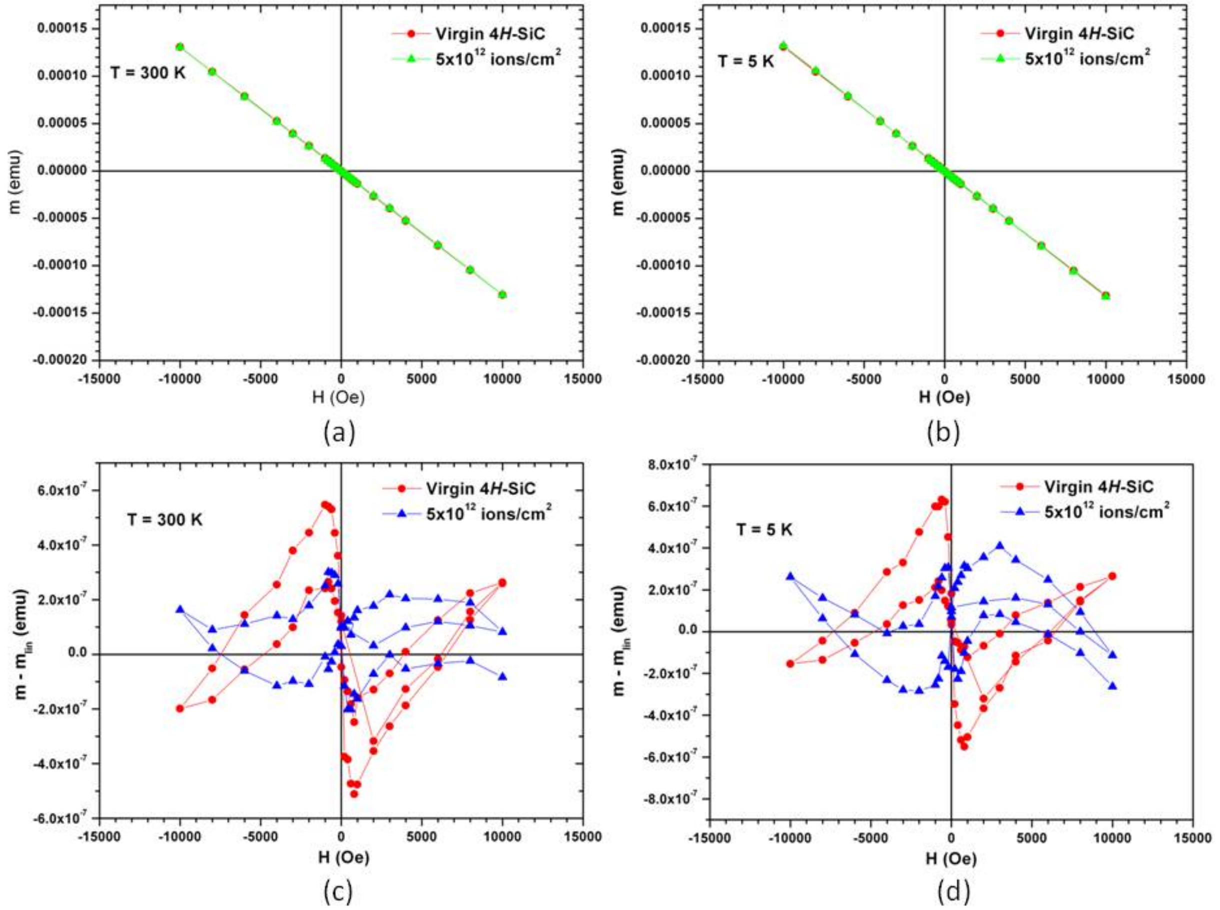

Figure 4.20: Magnetization at (a) room temperature 300 K and (b) low temperature 5K as a function of applied magnetic field for the same n-type 4*H*-SiC sample before (virgin) and after carbon-implantation. The implanted fluence 5×10^{12} ions/cm^2 corresponds to an average distance between vacancies of 1.94 nm as estimated from TRIM simulations. In (c) and (d) the magnetization is plotted without the diamagnetic contribution m_{lin} to identify any ferromagnetic contribution due to carbon irradiation. The data show no significant difference in the magnetization between virgin and implanted sample.

The curves in the Figures 4.20(c) and 4.20(d) show no significant difference of magnetization between the virgin and implanted sample. This results show that no magnetization has been achieved for the implanted sample with C fluence of 5×10^{12} ions/cm^2.

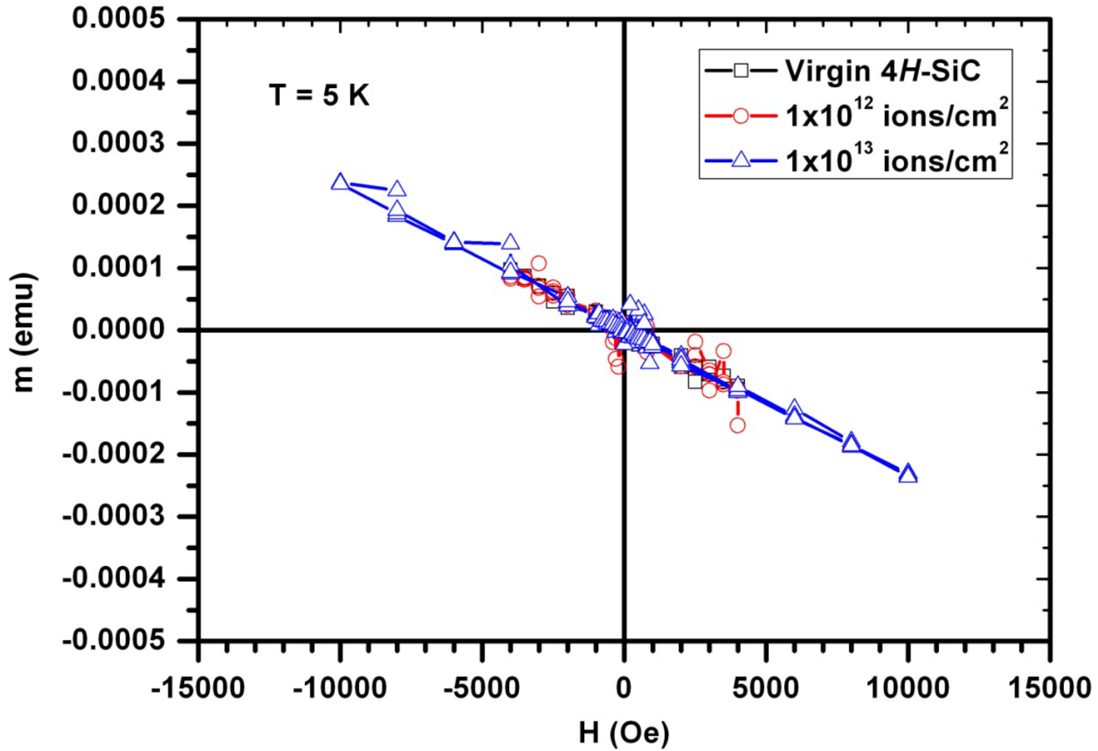

Figure 4.21: Magnetization as a function of magnetic field for virgin and implanted C fluence of 1×10^{12} ions/cm^2 and 1×10^{13} ions/cm^2 at 5K. These fluences correspond to the average distance between vacancies of 3.33 and 1.54 nm respectively as estimated from TRIM simulations.

All the implanted samples with fluences ranging from 1×10^{12} ions/cm^2 to 1.7×10^{16} ions/cm^2 except the sample with fluence 5×10^{12} ions/cm^2 were sent to the National Isotope Center at GNS Science, New Zealand. Figure 4.21 shows the magnetization measured as a function of magnetic field for C implanted fluences of 1×10^{12} ions/cm^2 and 1×10^{13} ions/cm^2. The implanted fluences along with the virgin samples show purely diamagnetic property. No ferromagnetism was induced even at these implanted fluences. Similar results were obtained for C implanted fluences of 8.5×10^{14}, 5×10^{15} and 1.7×10^{16} ions/cm^2 at room temperature which are shown in Figures 4.22 – 4. 24.

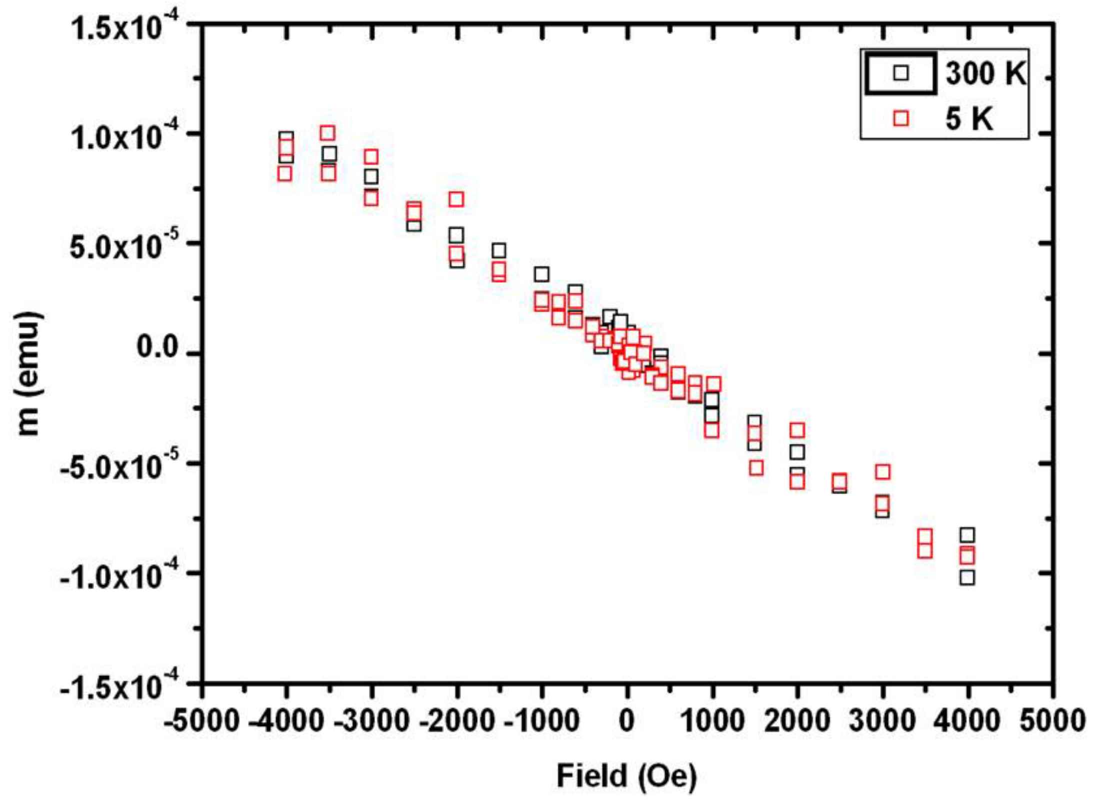

Figure 4.22: Magnetization as a function of magnetic field for the C implanted n-type 4*H*-SiC at low energy 60 keV with fluence 8.5×10^{14} ions/cm^2 at 300 K and 5K.

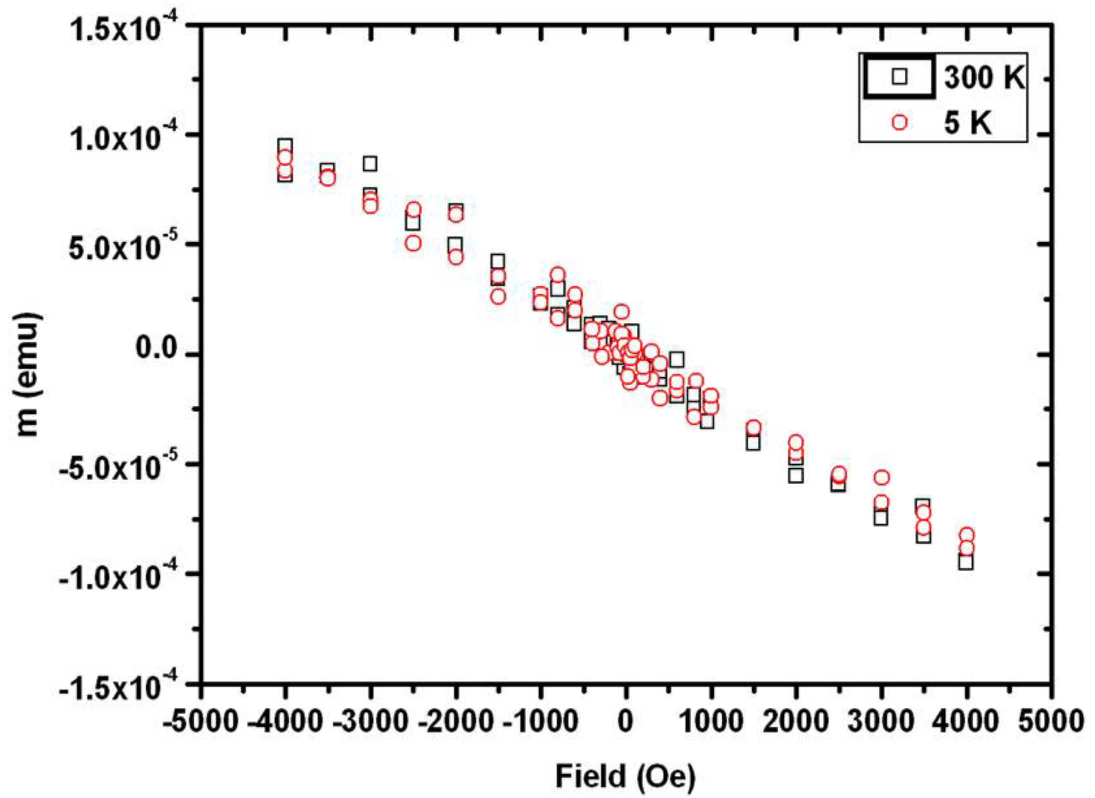

Figure 4.23: Magnetization as a function of magnetic field for the C implanted n-type 4*H*-SiC at low energy 60 keV with fluence 5×10^{15} ions/cm^2 at 300 K and 5K.

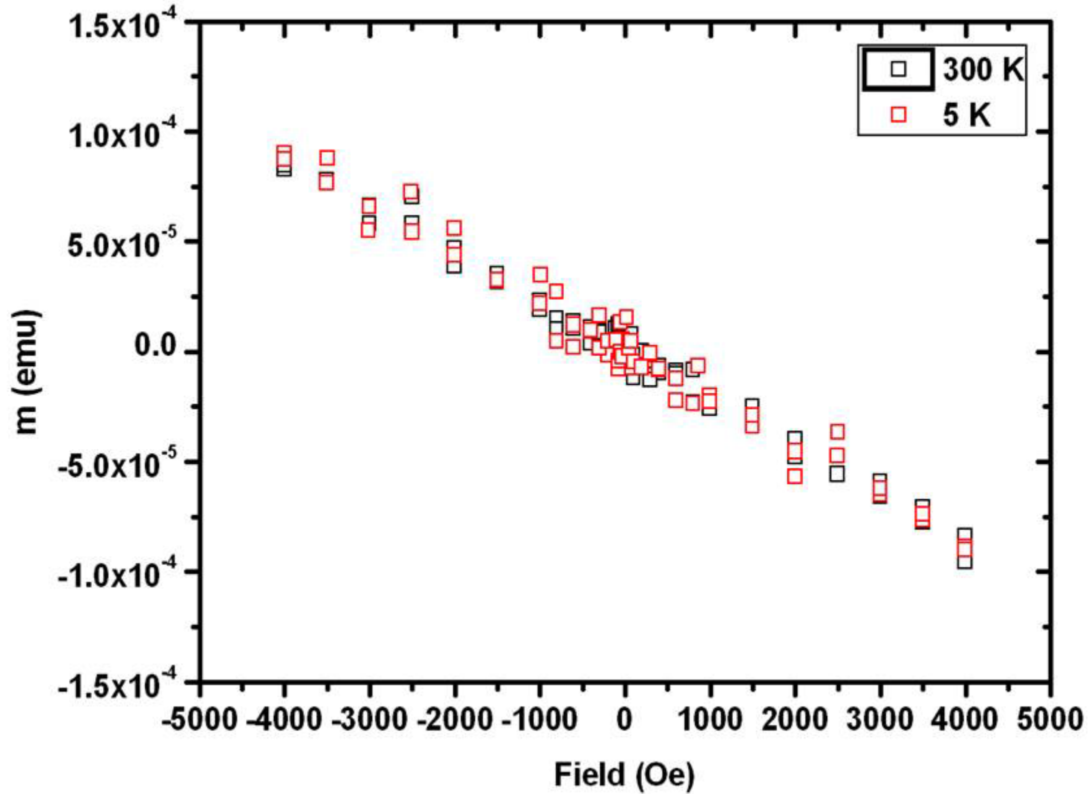

Figure 4.24: Magnetization as a function of magnetic field for the C implanted n-type 4*H*-SiC at low energy 60 keV with fluence 1.7×10^{16} ions/cm^2 at 300 K and 5K.

Additionally, the temperature dependence magnetization was measured in both field cooled (FC) and zero-field cooled (ZFC) conditions. In this condition the samples were subjected to oscillating with decreasing fields and were cooled from 400 K down to 0 K in a zero field. To obtain ZFC as a function of temperature, the samples were warmed up in the magnetic field measured either at 100 or 500 Oe. Later, the samples were cooled down in the same magnetic field and warmed up again to obtain the FC magnetization. The ferromagnetism can be determined from the difference between FC and ZFC magnetizations.

FC and ZFC magnetization curves for the virgin n-type 4*H*-SiC and for the C implanted at low energy 60 keV with fluences 1×10^{12} and 1×10^{13} ions/cm^2 respectively are shown in the Figures 4.25 – 4.27. No difference has been found between FC and ZFC magnetization curves in

C-implanted samples for the fluences 1×10^{12} and 1×10^{13} ions/cm^2 as compared to the unimplanted sample. The overlapping result of FC and ZFC magnetization curves suggests no existence of magnetic domains. For higher C implanted fluences, the FC and ZFC measurements were not performed since no ferromagnetic signal were observed during the initial magnetization measurements. All the samples with different C implanted fluences show no pronounced ferromagnetism. Lack of ferromagnetism can be attributed due to the absence of enough free carriers in n-type 4*H*-SiC.

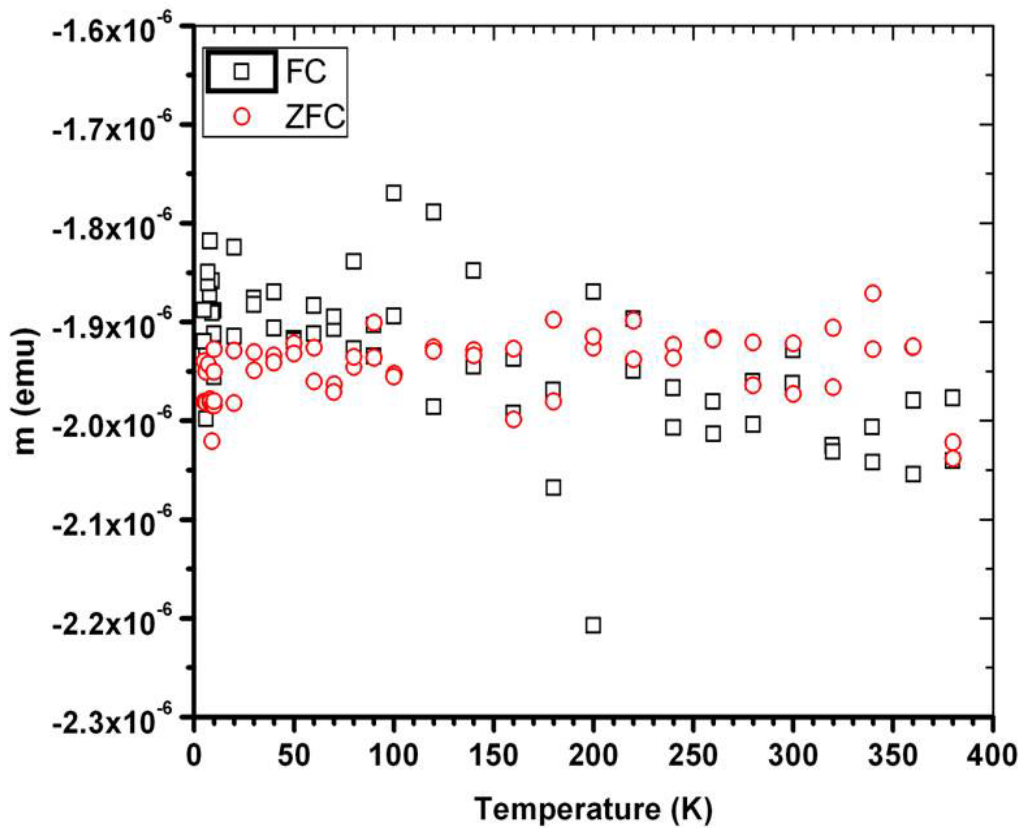

Figure 4.25: FC/ZFC magnetization curves for the virgin n-type 4*H*-SiC.

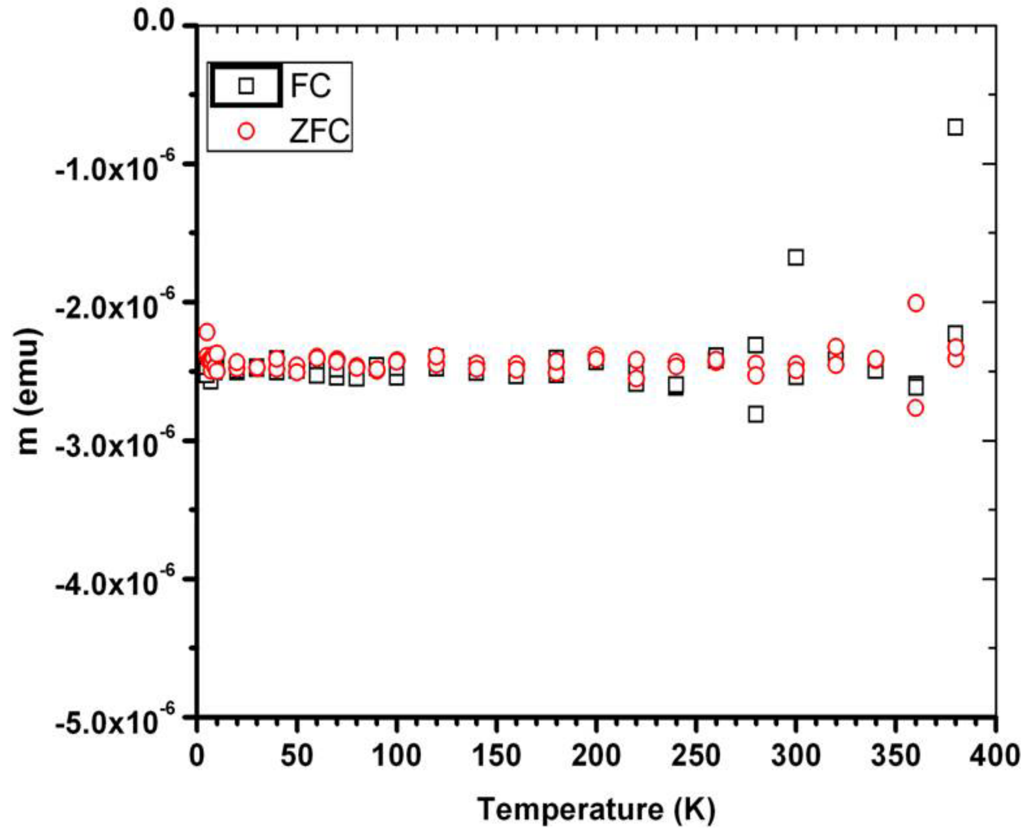

Figure 4.26: FC/ZFC magnetization curves for the C implanted n-type 4*H*-SiC at low energy 60 keV with fluence 1×10^{12} ions/cm^2.

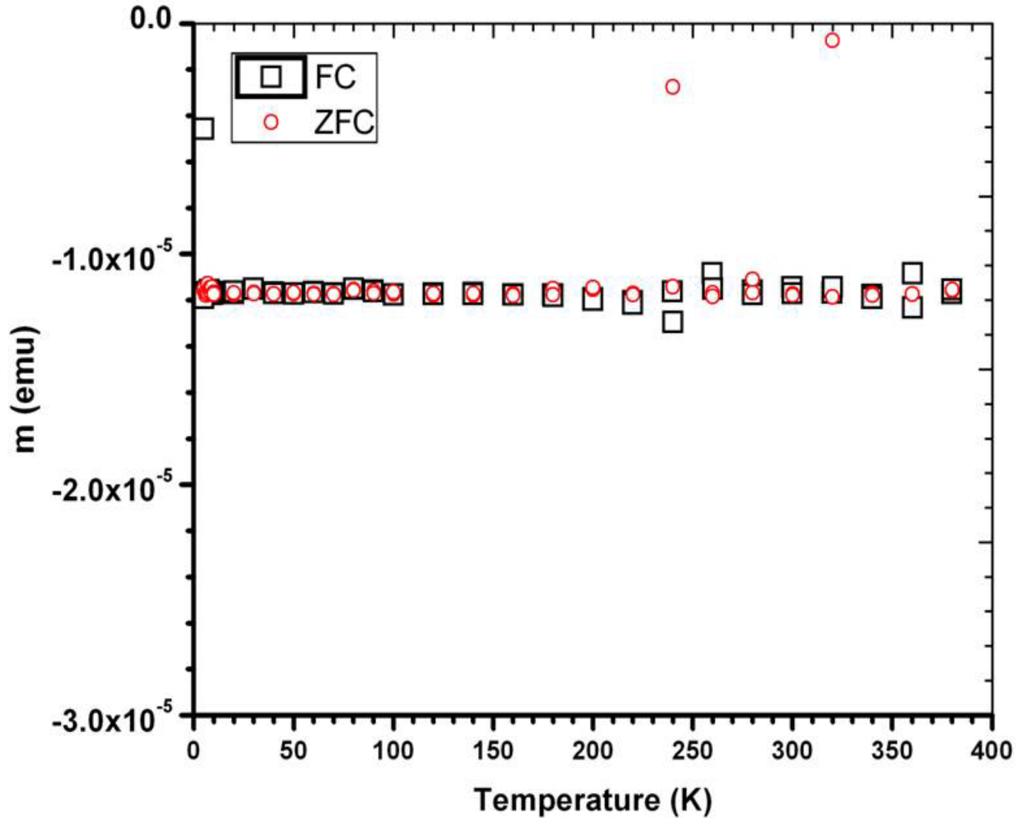

Figure 4.27: FC/ZFC magnetization curves for the C implanted n-type 4*H*-SiC at low energy 60 keV with fluence 1×10^{13} ions/cm^2.

ZnO is a wide band gap semiconductor similar to SiC. Buchholz et al. showed that Cu-doped n-type ZnO was nonmagnetic whereas Cu-doped p-type exhibited ferromagnetism [48]. Jin et al. have detected no indication of ferromagnetism for n-type $Zn_{1-x}TM_xO$ (TM = Cr to Cu) films down to 3 K [49]. Similar results were predicted by Bouloudenine et al. where no ferromagnetism was found in synthesized pure $Zn_{0.9}Co_{0.1}O$ DMS [50]. Theoretical prediction by Huang et al. show that p-type ZnO doped with Cu exhibited ferromagnetism whereas n-type ZnO doped with Cu did not possess any local magnetic moments [51]. Similar results were found by Sato et al. with Mn doped ZnO where the ferromagnetic ordering of Mn magnetic moments was induced by hole doping [52]. Through this research, we tested the hypothesis of defect induced room temperature stable ferromagnetism after self-ion implantation in n-type 4*H*-SiC. The

results show no indication of ferromagnetism in n-type 4*H*-SiC at room temperature and as well as at 5K.

Previous experimental studies, based on the implantation technology, reveal that ferromagnetism can be observed in SiC diluted with 3d transition metals. SQUID measurements showed that a Curie temperature of 50 K was observed for 3 and 5 atomic percent (at.%) of Ni doped in p-type SiC. Fe and Mn exhibited paramagnetic behavior at 3 at.%, where-as at 5 at.% Curie temperatures of 270 and 250 K were observed [53]. Room temperature ferromagnetism was observed in V-doped semi-insulating 6*H*-SiC [54]. Recent studies show that ferromagnetism was detected not only in transition metal doped SiC but also in transition-metal free implanted SiC. Ferromagnetism was observed with the implantation of Ne^+ ions in both semi-insulating 4*H*-SiC and 6*H*-SiC crystals [55, 56]. Liu et al. observed defect-induced magnetism in neutron irradiated semi-insulating p-type SiC crystals [57].

For all the experiments discussed above where ferromagnetism has been observed, either p-type or semi-insulating SiC were used, whereas our studies were carried out on n-type 4*H*-SiC. To date, to our best of our knowledge, no experimental work has been reported on investigating defect induced magnetism for self-ion implantation in n-type 4*H*-SiC. The defects, in particular vacancies, created by implantation in our work may favor the local magnetic moments according to the theoretical predictions but fail in inducing the long-range coupling between the moments caused by these defects. One of the important motivations in this research is to investigate ferromagnetism in n-type 4*H*-SiC. This possibility has been evaluated using SQUID measurements on C implanted samples. The achieved results led us to the conclusion of finding no magnetism in low energy (60 keV) C implanted n-type 4*H*-SiC crystals.

4.6 References

1. W. J. Choyke, H. Matsunami, G. Pensl, Silicon Carbide: Recent Major Advances, Springer Series, Berlin (2004).
2. C. Buttay, D. Planson, B. Allard, D. Bergogne, P. Bevilacqua, C. Joubert, M. Lazar, C. Martin, H. Morel, D. Tournier, C. Raynaud, Mater. Sci. Eng. B **176** 283 (2011).
3. F. Zhao, M. M. Islam, P. Muzykov, A. Bolotnikov, T. S. Sudarshan, IEEE Electron Device Letters **30** 1182 (2009).
4. P. Godignon, X. Jorda, M. Vellvehi, X. Perpina, V. Banu, D. Lopez, J. Barbero, P. Brosselard, S. Massetti, IEEE Trans. on Ind. Elect. **58**(7) 2582 (2011).
5. M. R. Fard, T. E. Blue, D. W. Miller, AIP Conf. Proc. **699** 574 (2004).
6. S. Metzger, H. Henschel, O. Kohn, W. Lennartz, IEEE Trans. on Nucl. Sci. **49**(3) 1351 (2002).
7. H. S. Kim, J. H. Ha, S. Park, S. W. Lee, M. K. Moon, G. Sun, C. H. Lee, Jou. of Nucl. Sci. and Tech. **48**(10) 1342 (2011).
8. R. Gerhardt (Editor), Properties and Applications of Silicon Carbide, InTech Rijeka, Croatia (2011).
9. H. Ohldag, T. Tyliszczak, R. Höhne, D. Spemann, P. Esquinazi, M. Ungureanu, and T. Butz, Phys. Rev. Lett. **98**(18) 187204 (2007).
10. X. He, T. He, Z. Wang and M. Zhao, Physica E **42**(9) 2451 (2010).
11. E. Bekaroglu, M. Topsakal, S. Cahangirov, S. Ciraci, Phys. Rev. B **81** 075433 (2010).
12. P. Esquinazi, J. Barzola-Quiquia, D. Spemann, M. Rothermel, H. Ohldag, N. Garcia, A. Setzer, T. Butz, J. Magn. Magn. Mater **322** 1156 (2010).

13. M. A.Ramos, J. Barzola-Quiquia, P. Esquinazi, A. Munoz-Martin, A.Climent-Font, M. Garcia-Hernandez, Phys. Rev. B **81** 214404 (2010).
14. W. Jiang, H. Wang, I. Kim, Y. Zhang, W. Weber, J. Mater. Res. **25** 2341 (2010).
15. A. Debelle, L. Thome, D. Dompoint, A. Boulle, F. Garrido, J. Jagielski, D. Chaussende, J. Phys. D : Appl. Phys. **43** 455408 (2010).
16. W. Jiang, W. Weber, J. Nucl. Mater. **389** 332 (2009).
17. W. Jiang. Y. Zhang, M. H. Engelherd, W. J. Weber, G. J. Exarhos, J. Lian, R. C. Ewing, J. Appl. Phys. **101** 023524 (2007).
18. S. Miyagawa, K. Baba, M. Ikeyama, K. Saitoh, S. Nakao, Y. Miyagawa, Surface and Coatings Technology **83** 128 (1996).
19. J. F. Barbot, S. Leclerc, M. David, E. Oliviero, R. Montsouka, F. Pailloux, D. Eyidi, M. Denanot, M. Beaufort, A. Declemy, V. Audurier, and C. Tromas, Phys. Stat. Sol. A **206** 1916 (2009).
20. Y. Zhang, W. J. Weber, A. Hallen, G. Possnert, J. Appl. Phys. **91** 6388 (2002).
21. L. Li, W. Hua, S. Prucnal, S. Yao, L. Shao, K. Potzger, S. Zhou, Nucl. Instr. and Meth. B **275** 33 (2012).
22. W. Jiang, W. J. Weber, S.Thevuthasan, D. E. McCready, Nucl. Instr. and Meth. B **148** 562 (1999).
23. W. Jiang, W. J. Weber, S.Thevuthasan, D. E. McCready, Nucl. Instr. and Meth. B **143** 333 (1998).
24. D. W. Feldman, J. H. Parker, Jr., W. J. Choyke, L. Patrick, Phys. Rev. **173** 787 (1968).
25. J.C. Burton, L. Sun, M. Pophristic, F. H. Long, Z. C. Feng, and I. T. Ferguson, J. Appl. Phys. **84** 6268 (1998).

26. H. Harima, Microelectronic Engineering **83** 126 (2006).

27. S. Nakashima and H. Harima, Phys. Stat. Sol. A **162** 39 (1997).

28. W. Jiang, Y. Zhang, M. H. Engelhard, W. J. Weber, G. J. Exarhos, J. Lian, and E. C. Ewing, J. Appl. Phys. **101** 1 (2007).

29. R. Middleton, A Negative Ion Cookbook, H.T.M.L. Version, M. Wiplich 1998, http://tvdg10.phy.bnl.gov/COOKBook (1998).

30. J. Lindhard, Mat. Fys. Medd. Dan. Vid. Selsk. **34**(14) 1 (1965).

31. S. T. Picraux, J. A. Davies, L. Eriksson, N. G. E. Johansson, J. W. Mayer, Phys. Rev. **180** 873 (1969).

32. W. K. Chu, J. W.M ayer, M. Nicolet, Backscattering Spectrometry, Academic Press, New York, 1978.

33. D. Shakhvorostov, W. N. Lennard, P. R. Norton, Nucl. Instru. And Meth. B **272** 18 (2012).

34. L. C. Feldman, J. W. Mayer, S. T. Picraux, Materials Analysis by Ion Channeling, Academic Press, New York, 1982.

35. O. W. Holland, D. Fathy, J. Narayan, O. S. Oen, Radiat. Eff. **90** 127 (1985).

36. J. R. Tesmer and M. Nastasi (eds), Handbook of Modern Ion Beam Materials Analysis, Materials Research Society, Pittsburgh (1995).

37. R. P. Devaty, W. J. Choyke, Phys. Stat. Sol. A **162** 5 (1997).

38. S. Nakashima, T. Kitamura, T. Kato, K. Kojima, R. Kosugi, H. Okumura, H. Tsuchida, M. Ito, Appl. Phys. Lett. **93** 12193 (2008).

39. M. Hundhausen, R. Pusche, J. Rohrl, L. Ley, Phys. Stat. Sol. B **245** 1356 (2008).

40. S. Nakashima and H. Harima, Phys. Stat. Sol. A **162** 39 (1997).

41. M. Gorman, S. A. Solin, Solid State Commun. **15** 761 (1974).

42. S. Nakashima and M. Hangyo, IEEE J Quantum Elec. **25** 965 (1989).

43. A. Perez-Rodriguez, Y. Pacaud, L. Calvo-Barrio, C. Serre, W. Skorupa, J. R. Morante, J. Electron. Mater. **25** 541 (1996).

44. A. Gentils, F. Linez, A. Canizares, P. Simon, L. Thome, M. Barthe, J. Mater Sci. **46** 6390 (2011).

45. W. J. Weber, L. M. Wang, N. Yu, N.J. Hess, Mater. Sci. Eng. A **253** 62 (1998).

46. M. G. Grimaldi, L. Calcagno, P. Musumeci, N. Frangis, J. V. Landuty, J. Appl. Phys. **81** (11), 7181 (1997).

47. M. A. Ramos, J. Barzola-Quiquia, P. Esquinazi, A. Munoz-Martin, A. Climent-Font, M. Garcia-Hernandez, Phys. Rev. B **81** 214404 (2010).

48. D. B. Buchholz, R. P. H. Chang, J. H. Song, J. B. Ketterson, Appl. Phys. Lett. **87** 082504 (2005).

49. Z. Jin, T. Fukurama, M. Kawasaki, K. Ando, H. Saito, T. Sekiguchi, Y. Z. Yoo, M. Murakami, Y. Matsumoto, T. Hasegawa, H. Koinuma, Appl. Phys. Lett. **78**(24) 3824 (2001).

50. M. Bouloudenine, N. Viart, S. Colis, A. Dinia, Chem. Phys. Lett. **397** 73 (2004).

51. D. Huang, Y. Zhao, D. Chen, Y. Shao, Appl. Phys. Lett. **92** 182509 (2008).

52. K. Sato and H. Katayama-Yoshida, Jpn. J. Appl. Phys. **39** L555 (2000).

53. N. Theodoropoulou, A. F. Hebard, S. N. G. Chu, M. E. Overberg, C. R. Abernathy, S. J. Pearton, R. G. Wilson, J. M. Zavada, Y. D. Park, J. Vac. Sci. Technol. A **20** 579 (2002).

54. Z. Shi-Yi, L. Xue-Chao, X. Ze, Y. Wan-Sheng, X. Jun, Y. Jian-Hua, S. Er-Wei, Chin. Phys. B **21**(6) 067503 (2012).

55. L. Li, W. Hua, S. Prucnal, S. Yao, L. Shao, K. Potzger, S. Zhou, Nucl. Instr. and Meth. B **275** 33 (2012).

56. L. Li, S.Prucnal, S. D. Yao, K. Potzger, W. Anwand, A. Wagner, S. Zhou, Appl. Phys. Lett. **98** 222508 (2011).

57. Y. Liu, G. Wang, S. Wang, J. Yang, L. Chen, X. Qin, B. Song, B. Wang, X. Chen, Phys. Rev. Lett. **106** 087205 (2011).

CHAPTER 5

DEFECT CHARACTERIZATION OF HIGH ENERGY IMPLANTATION OF N IN 4*H*-SiC

5.1 Introduction

It is a well-known fact that nitrogen is one of the major impurities in the n-type doping of SiC. The defects are created in the process of doping, which gives rise to deep-level centers in the band gap. These deep centers, which act as electron and hole traps or recombination centers, hinder the performance of the SiC devices. Rhim et al. have proposed that the nitrogen vacancy complexes exhibit magnetism in nitrogen doping of epitaxial graphene on SiC [1]. Weber et al. have investigated the defects in 4*H*-SiC using first principle calculations [2]. The results show that the isolated Si vacancies may possess properties similar to those of N-V centers, which can be potentially used to construct individual qubit states [3].

The exceptional properties of SiC, including chemical inertness and small capture cross-sections of neutrons make it an outstanding candidate for devices in extreme environments such as in nuclear fusion reactors or cladding material for gas-cooled fission reactors and space applications [4]. There is a necessity to study the defects which are created during implantation as it will lead us to use these material in future nuclear applications in a much better way. Out of the three commonly available polytypes of SiC, 4*H*-SiC is considered to be the most advantageous polytype. This polytype can be used not only in high temperature environments [5] but also in high power and high frequency devices because of its superior electronic properties [6]. Previous studies were focused on N implantation in SiC [7 - 11] but none of them studied the implantation induced disorder predominantly in n-type 4*H*-SiC at high energy. Results obtained by combining the advanced techniques of Rutherford backscattering spectrometry in channeling

mode (RBS-C), Raman spectroscopy and as well as Monte Carlo simulations using SRIM/TRIM–2012 are discussed. RBS-C results indicate the disorder is created in the sample along the transverse direction whereas Raman spectroscopy shows the disorder in both the transverse and longitudinal directions.

5.2 Theoretical Simulations and N Ion Implantation in 4*H*-SiC

5.2.1 SRIM/TRIM-2011 Simulations

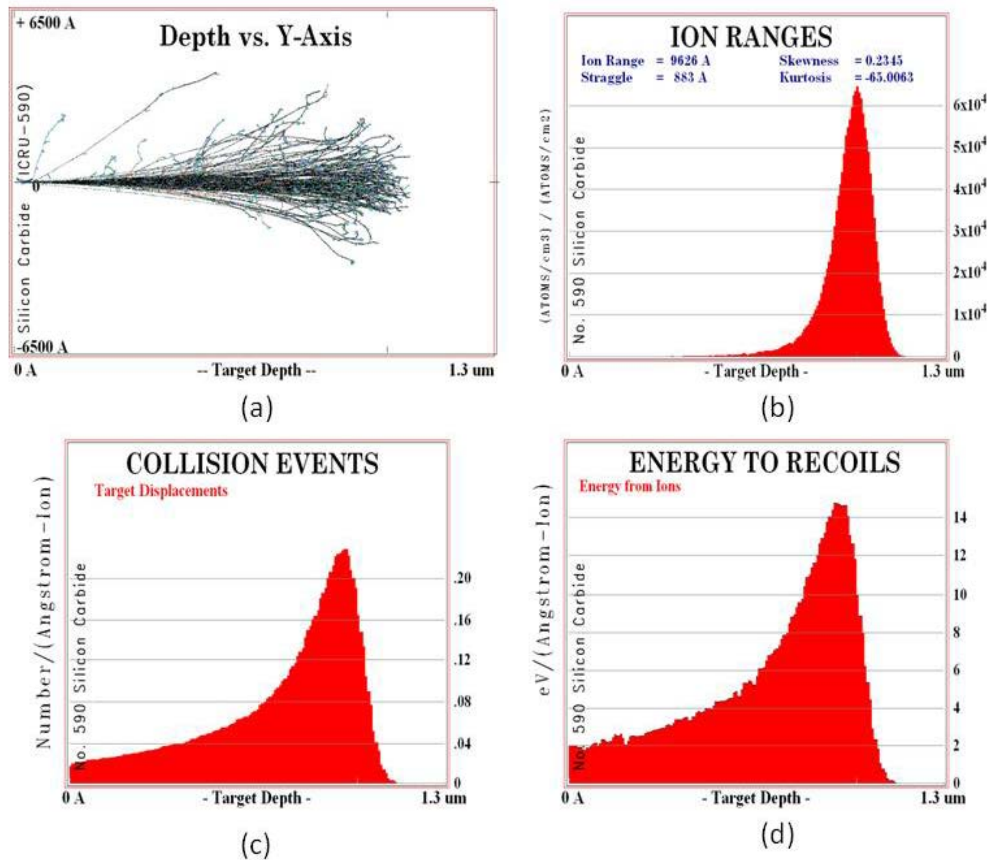

Figure 5.1: TRIM plots for N implantation in 4*H*-SiC at the higher energy of 1 MeV. (a) collision cascade between implanted N ions and SiC, (b) ion-distribution plot, (c) collision events which shows the displacements in the target and (d) energy to recoil atoms.

The outcome of the TRIM simulations is illustrated as different plots in the Figure 5.1. The path of the ion track, which reflects the collisions between implanted N ions and the

cascaded SiC atoms is shown in Figure 5.1(a). For N ions implanted at energy of 1 MeV, the projected range is around 962 nm with energy straggling of about 88 nm. The electronic and nuclear stopping power from SRIM -2011 is found to be 163.8 eV/Å and 1.89 eV/Å respectively.

5.2.2 High Energy Nitrogen Ion Implantation in 4*H*-SiC

A 2.5 MV Van de Graaff (HVEC Type AK) accelerator was used to generate the N ions for the implantation. The N ions were implanted with the higher energy of 1 MeV as compared to the lower energy of 60 keV for C and Si ions. Four different fluences of 1.5×10^{13} ions/cm^2, 7.8×10^{13} ions/cm^2, 1.5×10^{14} ions/cm^2 and 7.8×10^{14} ions/cm^2 were implanted on four different pieces of SiC of sizes 10 mm × 5 mm. From TRIM simulations, the dpa calculated for these fluences are 0.003, 0.018, 0.034 and 0.18 respectively.

5.3 Experimental Analysis of N Implanted 4*H*-SiC Samples

5.3.1 RBS-C Analysis

RBS-C analysis was performed for depth profiling of the implanted ions as well as to study the disorder formation. The ion channeling measurements on these implanted samples have been carried out at a National user facility, Environmental Molecular Sciences Laboratory (EMSL) within the Pacific Northwest National Laboratory (PNNL), Richland, WA.

An ion beam of He^+ at energy 3.5 MeV was used for ion channeling measurements. A higher energy of the probing He ion was necessary to separate the disorder peak in the silicon layers from the carbon signal. The spectra were collected for a 150° fixed detector and the detector was positively biased to 60 V. All the spectra were collected for charge integration of 10 μC and the current on the target was maintained about 15 nA (2 mm diameter in size). The target is positively biased to 300 V for suppression of electrons.

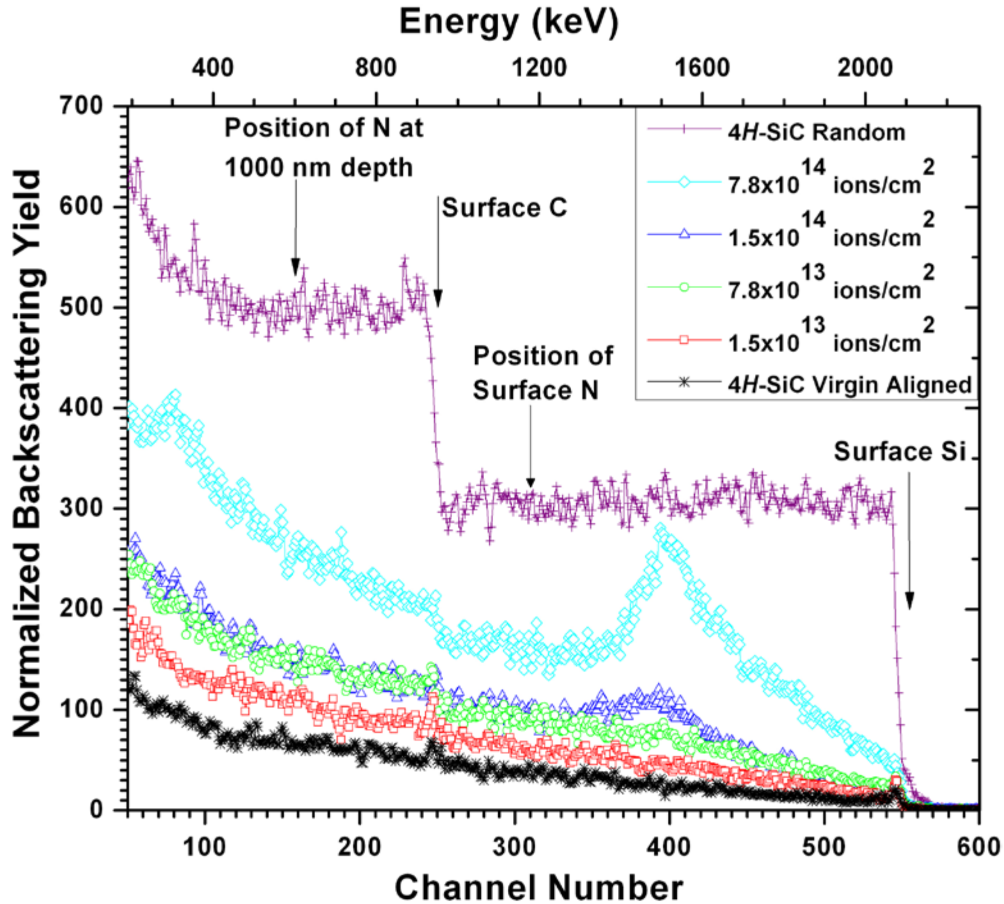

Figure 5.2: RBS-C spectra of 1 MeV N implanted 4*H*-SiC samples at room temperature analyzed using 3.5 MeV He^+ beam.

Figure 5.2 shows the RBS-C spectra of N implantation in 4*H*-SiC at the energy of 1 MeV for four different fluences, 1.5×10^{13} ions/cm^2, 7.8×10^{13} ions/cm^2, 1.5×10^{14} ions/cm^2, and 7.8×10^{14} ions/cm^2. These fluences can also be related in terms of dpa. As previously mentioned in section 5.2.2, the dpa is defined as the fraction of atoms that have been displaced from lattice sites by projectiles or recoils. The dpa has been calculated at the damaged peak using the value of 4*H*-SiC density of 9.64×10^{22} atoms/cm^3. The corresponding dpa values after conversion are 0.003, 0.018, 0.034 and 0.18 for the fluences 1.5×10^{13} ions/cm^2, 7.8×10^{13} ions/cm^2, 1.5×10^{14} ions/cm^2, and 7.8×10^{14} ions/cm^2, respectively.

Aligned spectrum of virgin 4*H*-SiC and the random spectrum was also included in the figure for comparison. The search for the channeling window was first performed on the virgin sample. The sample was rotated from -1° to +1° at the scan step of 0.207°. Once the minimum position for the backscattering yield was found, the sample was tilted from -1° to +1° at the scan step of 0.05°. After finding the minimum yield for the rotation and tilt positions, the aligned spectra for the virgin sample was taken at that position. Later, the random spectrum was taken on the implanted region while continuously rotating the sample from -7° to +7° in the rotation and tilt direction. From the Figure 5.2 it is clearly visible that as the implanted fluence increases, the backscattering yields for all the aligned spectra increases as well. The channel numbers 315 and 160 corresponds to the position of surface N and position of N at 1000 nm depth.

When a He^+ ion passes through the SiC target, it loses energy through interactions with electrons that are raised to excited states or ejected from the atoms. He^+ ions can also transfer energy to the nuclei of the solid through small angle scattering events. This energy loss, which is called nuclear collisions, is much smaller than the electronic collisions. The energy loss value of electronic and nuclear collision can be found out using SRIM-2011. The electronic energy loss of 3.5 MeV He^+ ions in SiC as calculated from SRIM-2011 has a value of about 267.4 eV/nm. Figure 5.3 shows the dE/dx of the He^+ ion from the energy of 0.5 MeV to 4 MeV. The depth is divided into slabs with each slab thickness of 5 nm. The energy loss dE/dx for the incoming and outgoing energies was calculated at each individual slab. The disorder profile was extracted after all the implanted samples spectra were subtracted from aligned spectrum and considering a linear dechanneling approximation to all the spectra.

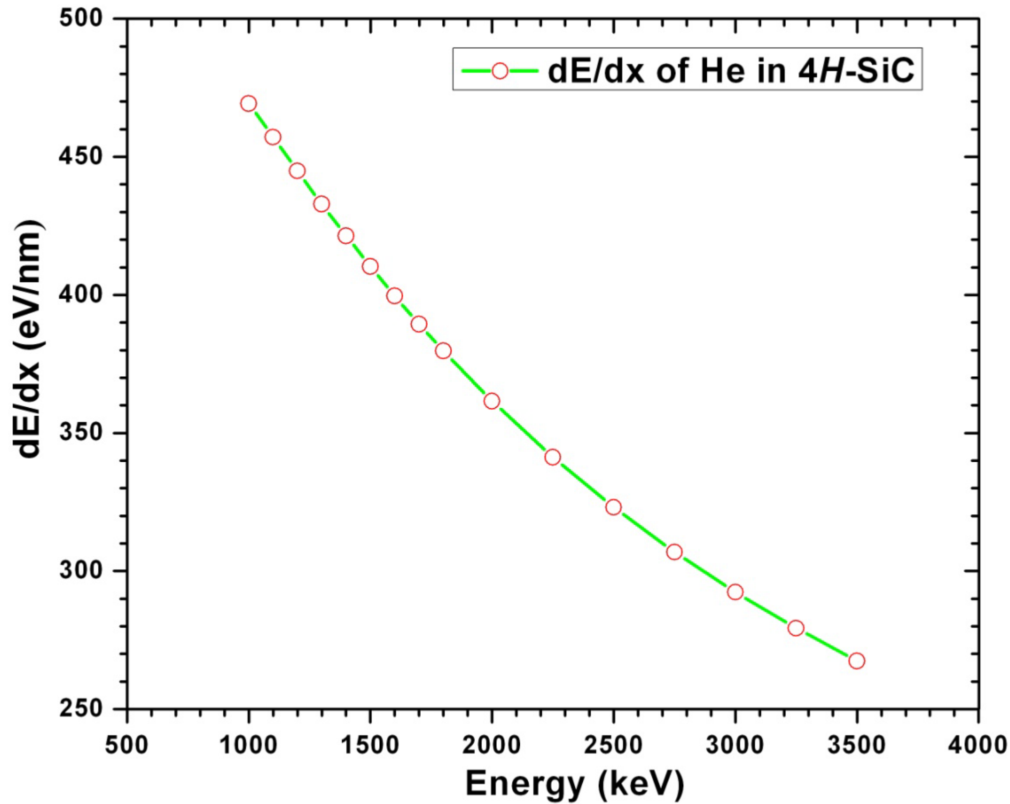

Figure 5.3: Energy loss (dE/dx) of He in 4*H*-SiC from energy 500 – 4000 keV.

The depth is evaluated for the implanted samples using the stopping power of He^+ ion in SiC. The resultant depth profile plot is shown in Figure 5.4. As shown in the Figure 5.4, the damage peak for all the implanted fluences is 1050±50 nm. From SRIM, the simulated depth is found to be 962±44 nm. The damage peak remained constant for all the implanted fluences, showing that there is no diffusion in the as-implanted samples. The sample implanted with lowest fluence of 1.5×10^{13} ions/cm^2, which corresponds to a dpa value of 0.003 at the damage peak, shows low-level disorder to be below 5%. For the next highest implanted fluence of 7.8×10^{13} ions/cm^2, which corresponds to a dpa value of 0.018 at the damage peak, the disorder is found to be below 10%. The disorder increases to 15% for the implanted fluence of 1.5×10^{14} ions/cm^2, which corresponds to a dpa value of 0.034 at the damage peak. For the highest implanted fluence of 7.8×10^{14} ions/cm^2, which corresponds to a dpa value of 0.18 at the damage

peak, 60% of the relative disorder is found. The disorder values are calculated using the yield ratios for the implanted samples aligned and in random position, where 100% disorder corresponds to total amorphization in the sample.

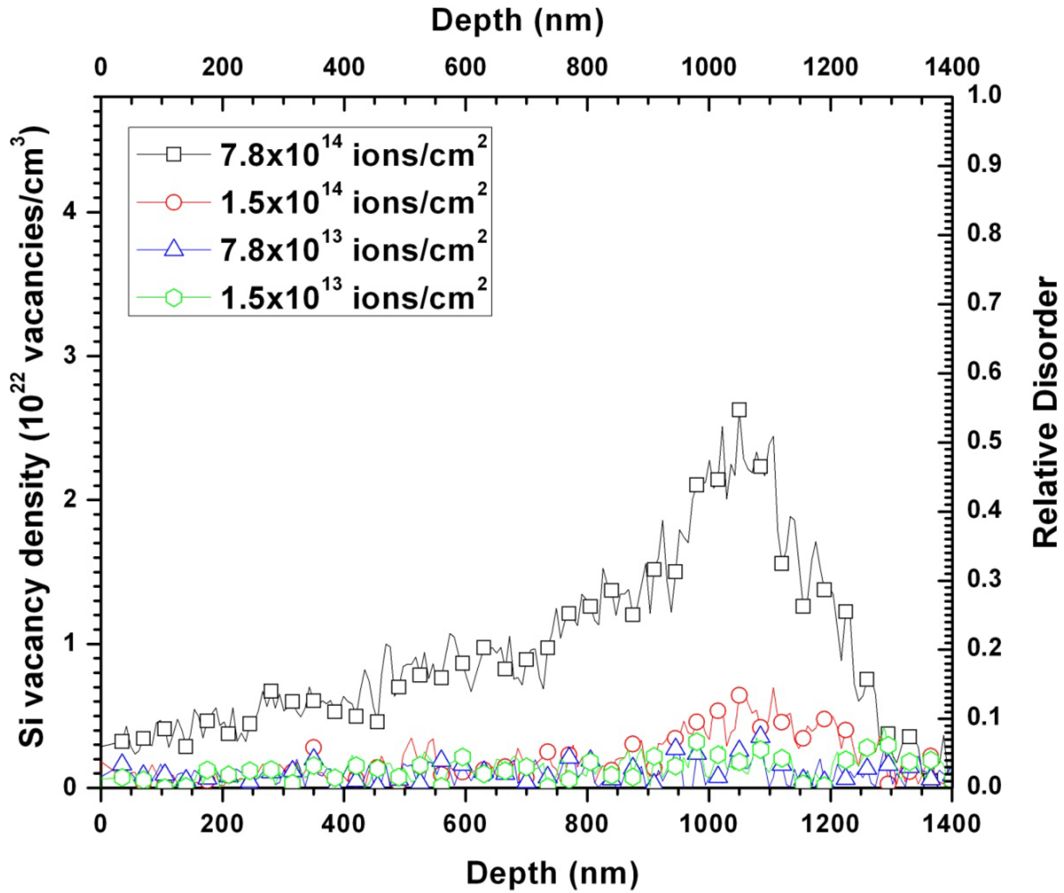

Figure 5.4: Relative disorder of Si sub-lattice as a function of depth.

5.3.2 Raman Analysis of Nitrogen Implanted 4*H*-SiC

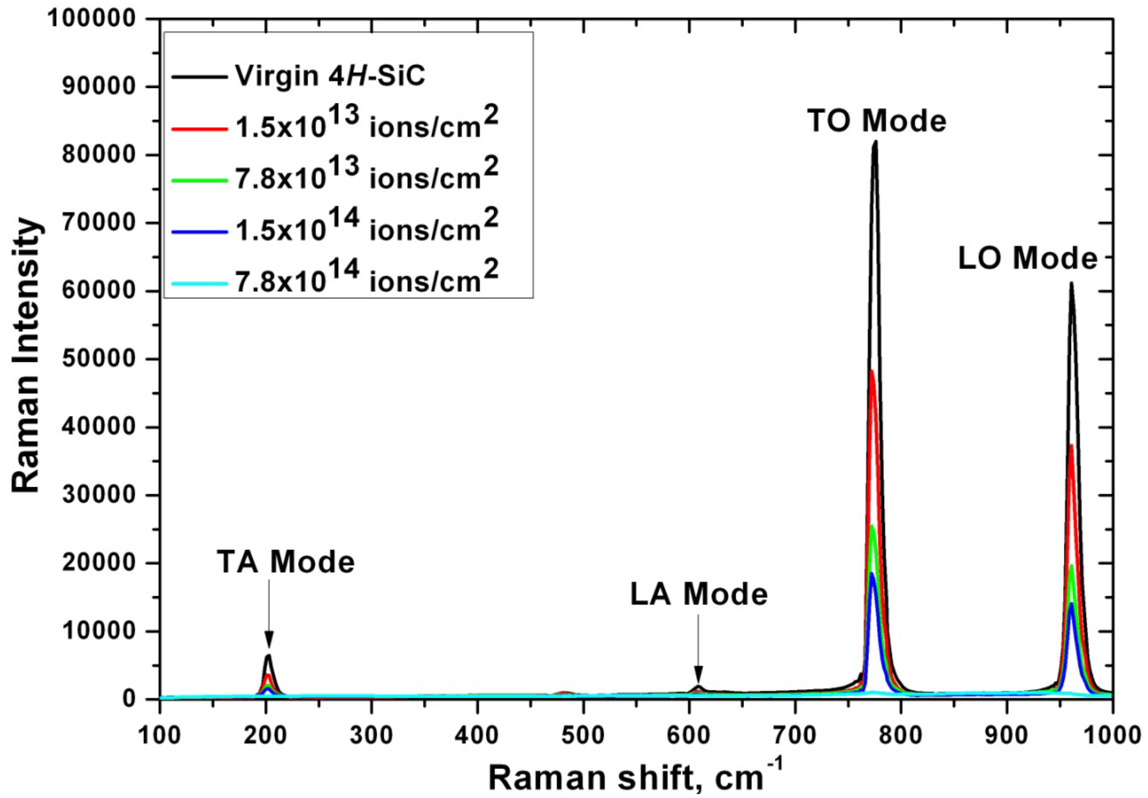

Figure 5.5: Raman shift spectra of high energy (1 MeV) N implanted 4*H*-SiC.

Figure 5.5 shows the Raman spectra of N implantation in 4*H*-SiC at the energy of 1 MeV for different fluences and for virgin 4*H*-SiC. The implantation-induced-disorder was also studied using Raman spectroscopy. The Raman system was calibrated using silicon as the standard, where the main Si phonon peak was seen at 521 cm^{-1}. After the calibration, the spectra for all the implanted fluences and the virgin sample were taken, which is shown in the Figure 5.5.

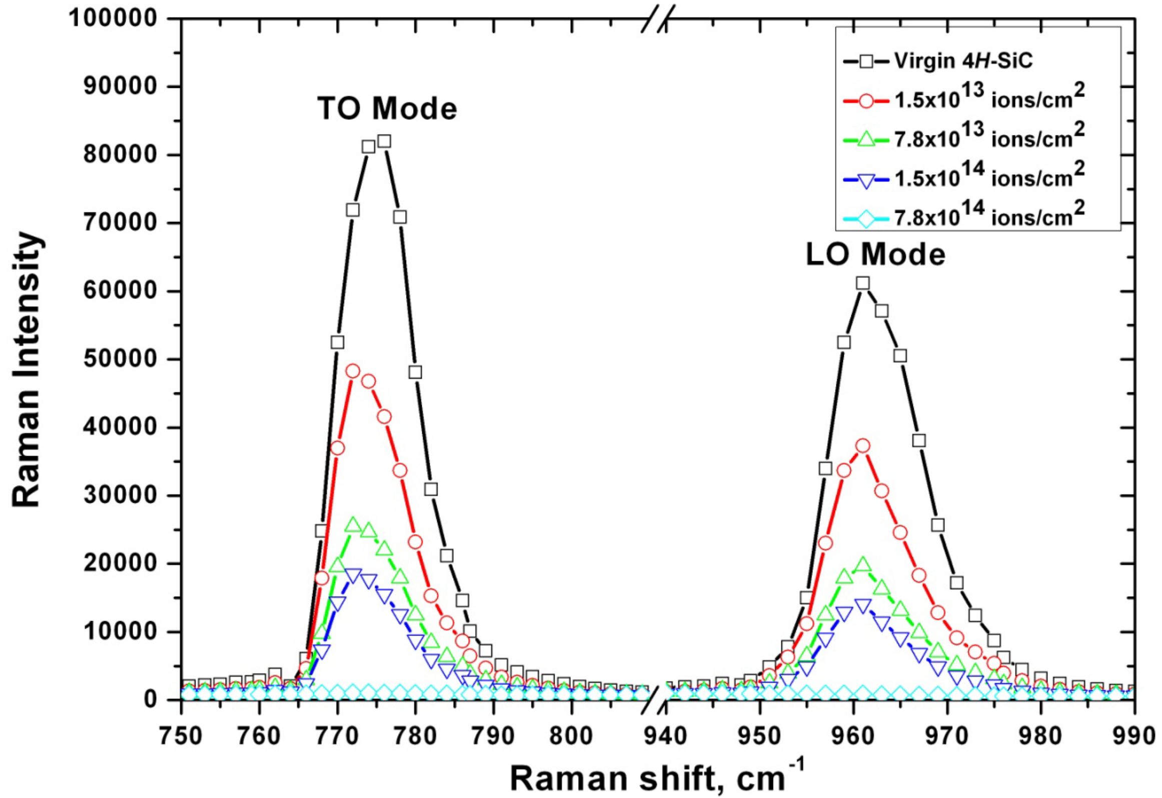

Figure 5.6: Raman spectra of 1 MeV N implanted 4*H*-SiC samples. The TO (775 cm^{-1}) and LO (964 cm^{-1}) mode signals are compared in order to determine the relative amount of disorder in the implanted samples.

Figure 5.6 shows the TO and LO mode signal for samples implanted with N ions in 4*H*-SiC at four different fluences. The spectrum from virgin sample is also included for comparison. From the Figure 5.6, the Raman spectra show a strong dependence on the intensity of the main Raman phonon modes. This is related to the implantation-induced-damage, which determines the decrease in intensity. The intensity gradually decreases as the fluence increases. The reduction in intensity is caused by the decrease in Raman polarizability because of the breaking of bonds and changes in atomic forces and displacements. The plot for the relative disorder for both the TO and LO modes measured from Raman measurements is shown in the Figure 5.7.

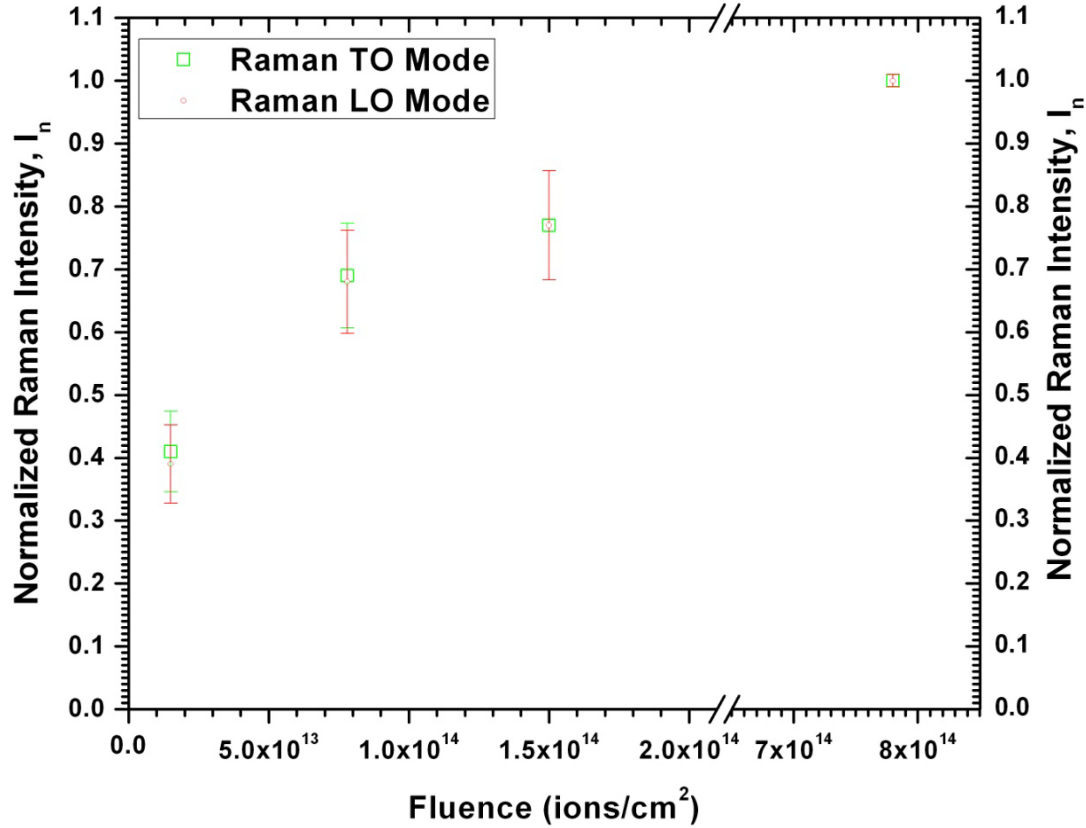

Figure 5.7: Relative Disorder of high energy (1 MeV) N implanted in 4*H*-SiC obtained from Raman measurements comparing the TO and LO modes.

The relative disorder for both the TO and LO modes of N implanted 4*H*-SiC has been evaluated. For the lowest implanted fluence of 1.5×10^{13} ions/cm^2, a relative disorder of 40% was calculated. The relative disorder increased to about 66% for the next implanted fluence of 7.8×10^{13} ions/cm^2. For the highest implanted fluence of 7.8×10^{14} ions/cm^2, the relative disorder increased to 100% corresponding to the total amorphization in the implanted sample. In Raman measurements, the transmitted intensity integrates over all the sample thickness. Thus, Raman measurements can be detected even for a low fluence of 1.5×10^{13} ions/cm^2, which has very low concentration of displaced atoms. The relative damage on Si sub-lattice calculated from RBS-C data and relative disorder from Raman measurements for the implanted N fluences in n-type 4*H*-SiC at high energy 1 MeV is summarized in Table 5.1. The relative disorder values from the

Raman measurements are higher than corresponding values for RBS-C measurements may be due to higher absorption of the probing light from deeper irradiated layers.

Table 5.1: Relative damage on Si sub-lattice from RBS-C data and relative disorder from Raman measurements for implanted N fluences in n-type 4*H*-SiC at high energy 1 MeV.

Implanted N fluences in n-type 4*H*-SiC at high energy 1 MeV (ions/cm^2)	Relative damage on Si sub-lattice from RBS-C data (%)	Relative disorder from Raman measurements (%)
1.5×10^{13}	<5	40
7.8×10^{13}	<10	66
1.5×10^{14}	15	75
7.8×10^{14}	60	100

5.4 References

1. S. H. Rim, Y. Qi, Y. Liu, M. Weinert, L. Li, Appl. Phys. Lett. **100** 233119 (2012).
2. J. R. Weber, W. F. Koehl, J. B. Varley, A. Janotti, B. B. Buckley, C. G. Van de Walle, D. D. Awschalom, J. Appl. Phys. **109** 102417 (2010).
3. P. G. Baranov, A. P. Bundakova, A. A. Soltamova, Phys. Rev. B **85** 125203 (2011).
4. P. Godignon, X. Jorda, M. Vellvehi, X. Perpina, V. Banu, D. Lopez, J. Barbero, P. Brosselard, S. Massetti, IEEE Trans. on Ind. Elec. **58**(7) 2582 (2011).
5. W. Lien, A. P. Pisano, D. Tsai, J. He, D. G. Senesky, Proceedings of the European Solid State Device Research Conference (ESSDERC) **234** (2012).

6. S. Ogata, K. Asano, Y. Sugawara, A. Tanaka, Y. Miyanagi, K. Nakayama, T. Izumi, T. Hayashi, M. Nishimura, International Power Electronics Conference (IPEC), 1929 (2010).
7. R. Capelletti, A. Miotelli, P. M. Ossi, J. Appl. Phys. **81** 146 (1997).
8. J. Gimbert, T. Billon, T. Ouisse, J. Grisolia, G. Ben-Assayag, C. Jaussaud, Mat. Sci. and Engg. B **61-62** 368 (1999).
9. Z. Zolnai, A. Ster, N. Q. Khanh, G. Battistig, T. Lohner, J. Gyulai, E. Kotai, M. Posselt, J. Appl. Phys. **101** 023502 (2007).
10. F. Moscatelli, A. Poggi, S. Solmi, R. Nipoti, IEEE Trans. on Elec. Dev. **55**(4) 961 (2008).
11. F. Zhou, Y. Yuan, K. Chen, X. Wang, Nucl. Instru. Met. in Res. B **267** 2858 (2009).

CHAPTER 6

SUMMARY OF THE DISSERTATION

Recently, defect induced magnetism in SiC has led to renewed attention in the semiconductor industry. Magnetism was achieved using the doping of transition metal ions in SiC, but to date, no one has ever reported experimentally attempts to find the induced magnetism due to the defects created in SiC by implantation of self-ions (host atoms). So far, it was only theoretically predicted for a layer by first principle calculations using the density functional theory. There is evidently a need to compare the calculated results to experimental measurements. This deficiency in the experimental research motivated us to investigate the defects produced in SiC by implantation of 60 keV host atoms (C, Si), which are transition metal free and not impurities in SiC. We have also investigated the defects due to implantation of high energy (1MeV) N in deeper layers.

The research presented in this dissertation is predominantly involved with ion implantation of C, Si and N ions in n-type 4*H*-SiC. Defect characterization of these implanted samples was analyzed using the techniques, RBS-C and Raman spectroscopy. The C and Si implantations were performed at room temperature using the SNICS-II source of negative ions by cesium sputtering associated with the NEC, 9SDH-2 tandem accelerator at IBMAL. The high energy N+ ions were implanted using a 2.5 MV Van de Graaff (HVEC Type AK) accelerator. Special importance was given to the Monte-Carlo simulations, which were performed using SRIM/TRIM -2011 before the implantation to find the different parameters such as the projected range, vacancy concentration and the displacement energies. These values obtained using the

simulations were later used in the experimental research work in estimating the fluences and calculating the dpa values.

6.1 RBS-C and Raman Measurements

6.1.1 C Implantation in 4*H*-SiC

C ions were implanted with the energy of 60 keV into n-type 4*H*-SiC for four different fluences. The fluences implanted were 1.85×10^{14}, 3.5×10^{14}, 7×10^{14} and 1×10^{15} ions/cm^2, which relate to the dpa values of 0.052, 0.098, 0.196 and 0.28, respectively. RBS-C analysis was performed to obtain the depth profiles of the implanted C ions and the relative disorders were assessed in the transverse direction. Raman spectroscopy was used to find the relative disorders in both the transverse and the horizontal directions. The experimentally determined depths of the Si damage peaks were found to be consistent with the SRIM-2011 simulations. For C implanted samples, the depth of the damage peak was found to be at 110±10 nm, which is in agreement with the SRIM simulated depth of 116±16 nm. For these C implanted fluences of (1.85×10^{14} cm^{-2} to 1×10^{15} cm^{-2}), the Si vacancy density varies from 1.37×10^{22} cm^{-3} to 4.22×10^{22} cm^{-3} with the average vacancy distances from 4.17 Å to 2.87 Å at the damage peak (110±10 nm). From the Raman spectroscopy, the implantation-induced lattice disorder calculated along the c-axis (LO mode) and perpendicular to c-axis (TO mode) in 4*H*-SiC is found to be similar.

6.1.2 Si Implantation in 4*H*-SiC

In addition to the C implantation, four different fluences of Si into 4*H*-SiC at the energy of 60 keV were also implanted. The fluences implanted were 5.5×10^{13}, 1.1×10^{14} cm^{-2}, 2.2×10^{14} cm^{-2} and 3.2×10^{14} cm^{-2}, which corresponds to the dpa values of 0.052, 0.103, 0.205 and 0.298, respectively. From the energy-depth conversion, the depth of the damage peak of Si implanted sample was found to be at 50±5 nm. The corresponding value from SRIM was 56±9 nm, which

agrees with the RBS-C data. From RBS-C Si sub-lattice measurements for different fluences (1.1×10^{14} cm^{-2} to 3.2×10^{14} cm^{-2}) of Si implantation in 4*H*-SiC, the Si vacancy density is estimated to range from 1.29×10^{22} cm^{-3} to 4.57×10^{22} cm^{-3}, corresponding to average vacancy distances of 4.26 Å to 2.79 Å at the damage peak (50±5 nm). Similarly to the C implanted samples, the implantation-induced lattice disorder calculated along the c-axis (LO mode) and perpendicular to c-axis (TO mode) in 4*H*-SiC is found to be similar to results from Raman spectroscopy.

6.1.3 N Implantation in 4*H*-SiC

Currently, there is great curiosity of N doping of SiC, which is well suited for applications in optoelectronic and optical devices. For this reason, studying of defects, which play an important role in these devices, is essential. N ion implantation was performed with the Van de Graaff accelerator at IBMAL. N ions were implanted at room temperature with the energy of 1 MeV. The fluences implanted are 1.5×10^{13}, 7.8×10^{13}, 1.5×10^{14} and 7.8×10^{14} ions/cm^2, which relate to the dpa values of 0.003, 0.018, 0.034 and 0.18, respectively. The experimentally determined depths of the Si damage peaks are found to be 1050±50 nm, whereas from SRIM simulations, the simulated depth is found to be 962±44 nm. For the highest implanted fluence, a relative disorder of 60% was obtained using the RBS-C technique. From Raman spectroscopy, the relative disorders varied from 40% for the lowest implanted fluence to 100% for the highest implanted fluence. This relative disorder from Raman measurements is found to be similar for both the TO and LO modes.

6.2 SQUID Measurements for C Implanted n-type 4*H*-SiC

For SQUID measurements different fluences of C were implanted in 4*H*-SiC at low energy 60 keV. The fluences implanted were 1×10^{12}, 5×10^{12}, 1×10^{13}, 5×10^{14}, 8.5×10^{14}, 5×10^{15}

and 1.7×10^{16} ions/cm^2 respectively. The dpa values calculated for these implanted fluences are 2.8×10^{-4}, 1.4×10^{-4}, 2.8×10^{-3}, 0.14, 0.24, 1.4 and 4.76 respectively. From TRIM – 2011 it was estimated that the vacancy creation reaches maximum to about 0.27 vacancies per carbon ion at the damage peak. This value can be used to calculate the vacancy concentration and the values are found to be 0.27×10^{20}, 1.35×10^{20}, 0.27×10^{21}, 1.35×10^{22}, 2.23×10^{22}, 1.35×10^{23} and 4.6×10^{23} respectively. These vacancy concentrations correspond to the average distance between vacancies of 3.3, 1.94, 1.54, 0.42, 0.35, 0.19 and 0.13 nm respectively. No hysteresis loop was observed in all the implanted fluences indicating that no magnetic moments were induced in the implanted sample due to the vacancies.

Additionally temperature dependence magnetization was measured in both field cooled (FC) and zero-field cooled (ZFC) conditions. No difference has been found between FC and ZFC magnetization curves in C-implanted samples for the fluences 1×10^{12} and 1×10^{13} ions/cm^2 as compared to the unimplanted sample. The overlapping result of FC and ZFC magnetization curves suggests no existence of magnetic domains. All the samples with different C implanted fluences show no pronounced ferromagnetism. Lack of ferromagnetism can be attributed due to the absence of enough free carriers in n-type 4*H*-SiC.

6.3 Significance of my Research Work

The studies presented in this dissertation are concerned with defects related to the damage formation during the lower energy of 60 keV ion (C, Si) implantations and higher energy of 1 MeV (N) implantation in n-type 4*H*-SiC. All the samples that were implanted with the lower energy 60 keV C and Si ions and the higher energy 1 MeV N ions were analyzed using RBS-C and Raman techniques. These two techniques probe the implanted samples in different ways (longitudinal and lateral directions) and can be used to evaluate the relative disorder produced.

Both the techniques provide the information and the evaluation of the disorder produced in the implanted samples can be performed straightforwardly. From the channeling technique, not only the relative disorder but also the depth distribution of the displaced atoms can be estimated from the aligned spectrum.

In the Raman measurements, the transmitted intensity integrates over all of the sample thickness, whereas in RBS-C, the analysis was performed only in (0 0 0 1) direction. Moreover in Raman, the absorption coefficient increases with damage and the penetration depth of the laser beam decreases with the amount of damage created in the sample. This is due to the strong optical absorption in the damaged layers. This can be the reason for the different percents of relative disorder that was evaluated using both of the techniques for the N implanted samples. In conclusion, these two techniques can act as complementary to each other in evaluating the relative disorder in the implanted samples.

The main focus is on the defect concentration, which is important to find the average distance between vacancies. The local magnetic moments, which can be induced due to the defects, depend on the average distance of vacancies, which is dependent on the density of the created defects. The defect concentration in turn is dependent on the ion fluence. Hence, the crucial point is the relation between the average distance of vacancies, defect concentration, and the fluence. The disorder build up during implantation with increasing implantation fluences has been studied for C, Si and N ion implants. The key outcome of this research is calculating the average distance between the vacancies which will helps us to determine the predicted narrow window in the implantation fluence that will result in local ferromagnetism in n-type 4*H*-SiC. Through this research, we tested the hypothesis of defect induced room temperature stable

ferromagnetism after self-ion implantation in n-type 4*H*-SiC. The results show no indication of ferromagnetism in n-type 4*H*-SiC at room temperature and as well as at 5K.

Previous experimental studies based on the implantation technology reveal that ferromagnetism can be observed in SiC diluted with 3d transition metals.. For all the experiments discussed above where ferromagnetism has been observed, either p-type or semi-insulating SiC were used, whereas our studies were carried out on n-type 4*H*-SiC. To date, to our best of our knowledge, no experimental work has been reported on investigating defect induced magnetism for self-ion implantation in n-type 4*H*-SiC. The defects, in particular vacancies, created by implantation in our work may favor the local magnetic moments according to the theoretical predictions but fail in inducing the long-range coupling between the moments caused by these defects. One of the important motivations in this research is to investigate ferromagnetism in n-type 4*H*-SiC. This possibility has been evaluated using SQUID measurements on C implanted samples. The achieved results led us to the conclusion of absence of ferro-magnetism in n-type 4*H*-SiC crystals implanted with low energy (60 keV) C^- ions with fluences in the range from 1×10^{12} ions/cm^2 to 1×10^{16} ions/cm^2. It may be interesting to carry out in future, similar investigations of defect induced magnetism in p-type and semi-insulating 4*H*-SiC.

APPENDIX

STOPPING AND RANGE OF IONS IN MATTER/TRANSPORT OF IONS IN MATTER

(SRIM/TRIM - 2011)

A1. Introduction

This computer program is based on the Monte Carlo simulations and was first developed by J. F. Zeigler and J. P. Biersack [1] and recent version can be found at http://www.srim.org. This simulation program is used to evaluate the energy loss of ions into matter, the final distribution of the ions, the displacement of lattice atoms by energetic ions in the material and the production of plasmons and phonons within the solid by the passing ions. All the SRIM and TRIM calculations in this dissertation work were performed using SRIM/TRIM-2011 version. The code starts with the input of the desired ion of a particular energy and direction into any target material, the code calculates the stopping and range of incident ions, producing tables that can be used for many different experimental calculations.

A2. Some Definitions of Important Parameters used in TRIM

In TRIM simulations the trajectory of the ion is perpendicular to the target surface, co-linear to the X-axis, and the Y- and Z-axis are orthogonal in the target surface plane. The different ranges can be defined as follows:

$$\text{Mean Projected Range}, R_p = \sum_i {x_i}/{N} = \langle x \rangle \qquad \text{Equation A1}$$

$$\text{Lateral Projected Range}, R_y = \sum_i {|y_i|}/{N} = \langle |y| \rangle \qquad \text{EquationA2}$$

$$\text{Radial Range}, R_r = \sum_i {(y_i^2 + z_i^2)}/{N} \qquad \text{Equation A3}$$

Here x_i is the projected range of ion, i on the x-axis. $\Sigma_i x_i$ is the sum of the ion projected ranges, $\Sigma_i x_i/N$ is the mean projected range of N ions and <x> is the mean projected range of all ions. For the lateral projected range, it is similar to mean projected range except the distance is taken in the XY plane. Cylindrical symmetry of the ion distribution is assumed in the radial

range. The other statistical terms of the moments of the energy loss distribution are straggling, skewness and kurtosis.

Straggling is defined as the square root of the variance and refers to the distribution of energy loss about an average value. It is related to the second moment of the ion distribution and is mathematically defined as below:

$$Straggling, \sigma = \left[\sum_i \left(\frac{x_i^2}{N}\right) - R_p^2\right]^{1/2} = \langle(\Delta x_i^2)\rangle^{1/2} \quad \text{Equation A4}$$

Similarly skewness and kurtosis are defined as the third and fourth moments of the ion distribution and is defined mathematically as follows:

$$\text{Skewness}, \gamma = \langle \Delta x^3 \rangle / [\Delta x^2]^{3/2} \quad \text{Equation A5}$$

$$\text{Kurtosis}, \beta = \langle \Delta x^4 \rangle / [\Delta x^2]^2 \quad \text{Equation A6}$$

In the definitions mentioned above, the projected range and the straggling have dimensions of length where as the terms skewness and kurtosis are dimensionless. Negative skewness indicates that the peak is skewed towards the surface and the most probable depth is greater than the peak depth. The positive skewness tells about the peak skewed away from the surface and the most probable depth is smaller than the peak depth. The term kurtosis indicates the extent of the distribution tails, with a value of 3 indicating a Gaussian distribution.

The damage in the target material such as target displacements, vacancies and replacement collisions can also be calculated using the Monte Carlo simulations from TRIM. Assume an energetic ion of energy E_i which has an atomic number Z_1 incident onto target material with an atomic number of Z_2. Displacement energy, E_d can be defined as the energy required for a target atom to leave its site and be pushed far enough away such that it will not

return to its empty site. The binding energy of a lattice atom to its site is E_b and the E_f is the final energy of the moving atom. After the energetic ion collides with the target material, the incident ion has energy E_1 and the target atom has energy E_2.

A displacement occurs when the struck atom energy is greater than displacement energy i.e. $E_2>E_d$. Similarly a vacancy occurs if $E_2>E_d$ and $E_1>E_d$. In the process, the energy E_2 of the moving atom is reduced by E_b before it collides with other atoms. The phonons are released when the struck atom does not have enough energy to leave the lattice site i.e. $E_2<E_d$ and the atoms vibrate back to their original site. In other case, when $E_2>E_d$ and $E_1<E_d$ and the incident ion and the target material has same atomic number, the incoming atom will remain on its lattice site and this collision is called as replacement collision with E_1 released as phonons. Similarly when $E_2>E_d$ and $E_1<E_d$ and the atomic numbers are not the same, then Z_1 becomes a stopped interstitial atom. The other process is when $E_1<E_d$ and $E_2<E_d$, Z_1 becomes an interstitial and E1+E2 is released as phonons.

A3. TRIM Set Up

TRIM is a program included in SRIM; all the features of the transport of ions in matter can be achieved using TRIM. This program will accept from simple layer target to complex targets made of compound materials with up to eight layers each of different materials. All kinetic phenomena associated with the ion's energy loss such as target damage, sputtering, ionization, phonon production, displacement, and vacancy concentration can be simulated. All target atom cascades are followed in detail. Before running the program, the different types of damages that can be selected are: a) ion distribution and quick calculation of damage, b) detailed calculation with full damaged cascades, c) surface sputtering and monolayer collision steps, d) varying ion energy/angle/depth in both quick damage and full damage cascades, e) damage

cascades from neutrons/electrons/photons in both quick damage and full damage cascades, and f) special multilayer biological targets.

Quick damage calculations are used if the details of target damage or sputtering are not necessary. But when the details about target damage or sputtering are needed, full damage cascades with detailed calculation can be performed. This option follows every recoil until its energy drops below the lowest displacement energy of any target atom. Thus, all collision damage to the target is analyzed. All the calculations for this research are done using the option "detailed calculation with full damage cascades." Before running TRIM, this option needs to be selected. The other data that needs to be input in TRIM are the name of the ion, target material, its density, angle of incidence, and energy of the ion. TRIM accepts any values from 10 eV to 2 GeV. The lower limit is due to the failure of the binary approximation and the higher value is due to neglection of high order relativistic effects. TRIM offers the features of stopping and restarting the ion penetration profile and changing of other defined parameters in the middle of a simulation if necessary. TRIM also requires the input of displacement energy, which is the amount of energy required to displace an atom from its lattice position, i.e. the amount of energy required to produce a stable Frenkel defect. The displacement energies of 20 eV and 35 eV were used for C and Si respectively for the theoretical simulations. From the energy loss of the ions and recoiling of the atoms, TRIM calculates the distribution of Frenkel defects. The absolute defect concentration predicted by TRIM simulations critically depends upon the value of the inputted displacement energy.

A.1 References

1. J. F. Ziegler, J. P. Biersack, U. Littmark, The Stopping and Range of Ions in Solids, Pergamon, Press, New York (1985).